Quantum Optics in Dense Atomic Media: From Optical Memories to Fluids of Light

Quentin Glorieux

▶ **To cite this version:**

Quentin Glorieux. Quantum Optics in Dense Atomic Media: From Optical Memories to Fluids of Light. Atomic Physics [physics.atom-ph]. Sorbonne Université, 2018. tel-01950430

HAL Id: tel-01950430
https://theses.hal.science/tel-01950430

Submitted on 20 Dec 2018

HAL is a multi-disciplinary open access archive for the deposit and dissemination of scientific research documents, whether they are published or not. The documents may come from teaching and research institutions in France or abroad, or from public or private research centers.

L'archive ouverte pluridisciplinaire **HAL**, est destinée au dépôt et à la diffusion de documents scientifiques de niveau recherche, publiés ou non, émanant des établissements d'enseignement et de recherche français ou étrangers, des laboratoires publics ou privés.

Quantum Optics in Dense Atomic Media: From Optical Memories to Fluids of Light

QUENTIN GLORIEUX

Habilitation à diriger des recherches
Sorbonne Université

Membres du Jury :
Valia Voliotis, Présidente
Antoine Browaeys, Rapporteur
Iacopo Carusotto, Rapporteur
Jacqueline Bloch, Examinatrice
Juergen Eschner, Examinateur
Robin Kaiser, Examinateur

Laboratoire Kastler Brossel
Paris, France
3 Décembre 2018

Contents

Introduction

Looking back over almost a decade of research after I graduated in 2010, I realized that what fascinates me the most in physics are the analogies between apparently unrelated phenomena. Connecting microscopic descriptions and macroscopic quantities as does thermodynamics, or the general framework of spin 1/2 particle from NMR to quantum information... These are just two examples but one can find this everywhere in modern physics.

I cover in this work the links between what is known today as quantum technologies and the more fundamental topic of quantum fluids. I have always envisioned myself as a fundamental physicist, remotely interested in real-life applications. However, it is funny to note that part of what I believed to be fundamental science 10 years ago (quantum memories, squeezing, entanglement...) is today entering in the phase of technological development and applications with the major effort of the EU towards quantum technologies. This is exactly what should motivate basic science: sometimes it does bring applications to make our life easier and a better society and sometimes it just provides knowledge itself without any immediate application (which also pushes toward a better society by making it smarter). I am curious to see what quantum fluids will bring in 10 years. This work summarizes my (modest) contribution to this field.

The main goal of this manuscript is to provide the tools to connect non-linear and quantum optics to quantum fluids of light. Because the physics of matter quantum fluids and fluids of light has long been the territory of condensed matter physicists, it is uncommon to find textbooks which draw the analogies with quantum optics. I have taken the reverse trajectory, being trained as a quantum optician and moving progressively to quantum gases and quantum fluids of light. Naturally, I try to use the concepts and resources developed by the quantum optics community to improve experiment about fluids of light, but I also reverse the approach and ask a very simple question: what does the concept of fluid of light bring to our understanding of non-linear and quantum optics ? It can be rephrased as an operational question: which new effects can we predict (and possibly observe) using the photon fluid formalism ?

This is actually a very exciting time, as we have recently demonstrated the validity of this approach with an experiment about the dispersion relation in a fluid of light [1]. In this experiment, described in details in the chapter 4, we have shown that light in a non-linear medium follows the Bogoliubov dispersion: a constant group velocity at small wavevectors and a linear increase with k at large wavevectors. If you trust the formal analogy between the non-

linear Schrödinger equation and the paraxial propagation of light in a non-linear medium, this result is not surprising. However, what is amazing is that, this description allowed us to design a non-linear optics experiment and helped us to understand it. This experiment can also be thought as a correction to the Snell-Descartes law in a non-linear medium. In this analogy,the group velocity is directly linked to the position of the beam in the transverse plane at the output of the medium. A linear increase with k at large wavevectors translates to the standard refraction law: increasing the incidence angle will increase the distance from the optical axis after the medium. However, at small angle the constant (non-zero) group velocity tells us that, whatever the angle of incidence, the beam will exit the medium at the same position ! The refraction law is independent of the incident angle. Moreover, another idea can be extracted from quantum gases formalism: the group velocity depends on the medium density (at small k). Therefore the refraction law does not depend on the incident angle but on the light intensity ! Can we do something with this ? I don't know. Maybe we can use this novel understanding to image through non-linear medium. Or maybe we just understand a bit more of non-linear optics now.

This time is a very exciting one also because now we know that this approach works and we have tens of ideas for novel non-linear optics experiments testing the cancellation of drag force due to superfluidity, observing the Hawking radiation, or the Zel'dhovich effect... The next challenge is to bring this description to the field of quantum optics, where quantum noise and entanglement are of primary importance. What is the hydrodynamic analogue of squeezing or of an homodyne detection ? Understanding the effects of interactions in complex quantum systems beyond the mean-field paradigm constitutes a fundamental problem in physics. This manuscript just briefly ventures in this territory... But this will be, for sure, the next direction of my scientific career.

In fact I did not venture in this territory, but this manuscript intends to provide the tools to do so in the future. Chapter 1 is a brief summary of what are the tools needed for quantum optics in a warm atomic medium: the two-level atoms model, electromagnetically induced transparency, four-wave-mixing, cooperative effects and decoherence. In chapter 2, I describe one type of optical quantum memory based on the gradient echo memory protocol. I present two implementations: in a warm vapor and in high optical depth cold atomic cloud and cover how these two implementations are complementary with their specific strengths and weaknesses. In chapter 3, I move to quantum optics with the study of imaging using the noise properties of light and propagation of quantum noise in a fast light medium. I complete the description of my previous works in chapter 4 including more recent experiments about fluid of light in an exciton-polariton microcavity and in an atomic vapor. The final chapter is devoted to describe several outlooks and collaborative projects I have recently initiated.

Chapter 1

Hot atomic vapor

1.1 Atomic ensembles

When learning about light-atom interaction, various approaches can be discussed. Light can be described as a classical electromagnetic field or as quantum elementary excitations: the photons. Similarly an atom can be seen as a classical oscillating dipole or treated using quantum mechanics. The description of the interaction can then take any form mixing these 4 different perspectives. While for most experiments a classical approach is sufficient, it is sometimes needed to invoke $\hbar$ and its *friends* to explain a specific behaviour. In this work, I will try, as much as possible, to avoid an artificial distinction between quantum and classical phenomena, as it does not bring much to the understanding of the effects. Sometimes, a purely classical description is even more intuitive.

In this first section, I remind readers of the basic tools to appreciate atomic ensemble physics, without entering into the details and complexities of genuine alkali atomic structures. I describe the differences in light-matter interaction between the case of one single atom and an atomic ensemble, and explain what I call a dense atomic medium. A short discussion will illustrate the relationship between collective excitations and Dicke states [2]. This work is mainly focused on warm atomic ensembles (with the notable exception of section 2.2) and therefore a discussion on the role of Doppler broadening and the assumptions linked to it will conclude this part.

1.1.1 Light–matter interaction

Let us start with the simplest case: one atom interacting with light in free space. Two processes, time-reversals of each other, can happen: absorption and stimulated emission[1]. An important question is: what is the *shadow* of an atom ? Or more precisely what is the dipole cross-section σ_0 of one atom interacting with light in free space ? It is interesting to note that the answer to this question does not depend on the description of the atom as a classical oscillating dipole or a two-level atom. With λ being the light wavelength, we

[1] Obviously, a third process, called spontaneous emission, is also possible, but for this specific discussion we do not need it.

have the resonant cross section for a two-level atom[2] can be written as: [3]:

$$\sigma_0 = \frac{3\lambda^2}{2\pi}. \tag{1.1}$$

From this relation, we can immediately conclude that it is a *difficult* task to make light interact with a single atom. Indeed, focusing light in free-space is limited by diffraction to a spot of area $\sim \pi\lambda^2/4$. Therefore, even a fully optimized optical system, will not reach a focusing area of σ_0. What is surprising here, is that it does not depend on the choice of your favorite atom.

Nevertheless various tricks can be tested to improve this coupling. A common criteria to discuss the interaction strength is called cooperativity C and is given by the ratio between the dipole cross section and the mode area of the light:

$$C = \frac{\sigma_0}{\text{Area}_{\text{mode}}}. \tag{1.2}$$

The cooperativity gives the ratio between the photons into the targeted mode and those emitted to other modes.

A simple way of increasing C is to put your single atom in an optical cavity. By doing so you will approximately multiply C by the number of round trips inside the cavity. The cooperativity will be modified to:

$$C = \frac{\sigma_0}{\text{Area}_{\text{mode}}} \frac{1}{T}, \tag{1.3}$$

with T being the output mirror transmission. A second approach would be to reduce the area of the mode below diffraction limit. It is obviously impossible with a propagating field but it has been observed that using the evanescent field near a nano-structure can indeed provide a mode area well below $\pi\lambda^2/4$. In this work we will use another way of improving coupling: by adding more than one atom we can increase the cooperativity by the number of atoms N as

$$C = \frac{\sigma_0}{\text{Area}_{\text{mode}}} N. \tag{1.4}$$

The cooperativity is therefore equal to the inverse of the number of atoms needed to observe non-linear effects. Unfortunately, adding more atoms comes with a long list of associated problems that we will discuss throughout this work.

1.1.2 Dicke states and collective excitation

Getting a large cooperativity means having a large probability for a photon to be absorbed by the atomic medium. However, we find here an important conceptual question: if a photon is absorbed by the atomic ensemble, in what direction should I expect the photon to be re-emitted ? If there is an optical cavity around the atomic ensemble, it is natural to expect the photon to be more likely emitted in the cavity mode, since it is most strongly coupled to the atoms. The coupling efficiency β is the ratio between the decay rate in the cavity mode to the total decay rate and is given by:

$$C = \frac{\beta}{1-\beta}. \tag{1.5}$$

[2] More generally, the cross section for an atom with F_g and F_e being the total angular momenta for the ground and the excited states respectively, has the form $\sigma = \frac{2F_e+1}{2F_g+1}\frac{\lambda^2}{2\pi}$.

But, what if we do not place the atoms in a cavity ? Why shouldn't we expect the recovered field in any arbitrary direction ? This would make the job of an experimental physicist way trickier...

Dicke states

We can get a physical intuition of why light is mainly re-emitted in the forward direction by introducing Dicke states. In 1954, Robert Dicke predicted in Ref. [2] that the behaviour of a cloud of excited atoms would change dramatically above a density of 1 atom per λ^3. Indeed, when the inter-atomic distance becomes smaller than the wavelength of the emitted photons, it becomes impossible to distinguish which atoms are responsible for the emission of individual photons. This indistinguishability lead to a spontaneous phase-locking of all atomic dipoles everywhere in the medium, and therefore a short and directional burst of light is emitted in the forward direction. The anisotropic nature of the emission can be understood simply as a constructive interference due to the alignment of atomic dipoles thanks to the dipole-dipole interaction [4, 5].

Collective excitation

When the atomic density is lower than λ^{-3}, the dipole-dipole interaction becomes negligible but, fortunately, directional emission can still occur. The mechanism involved here is similar to the Dicke prediction. When one photon interacts with the atomic ensemble, the created excitation is delocalized in the entire cloud. *Every* atom participates in the absorption process and each of them retains the phase of the incoming field in the coherence between the ground and the excited states. If the Fock state with only one photon is sent into the medium, the collective state of the atomic cloud $|\underline{e}\rangle$ will be written as a coherent superposition of all possible combinations of a single atom excited $|e\rangle$ and all the other ones in the ground state $|g\rangle$:

$$|\underline{e}\rangle = \frac{1}{\sqrt{N}} \sum_{i=1}^{N} |g_1, g_2, ..., g_{i-1}, e_i, g_{i+1}, ..., g_N\rangle. \tag{1.6}$$

Once again the collective enhancement comes from a constructive interference effect [6]. During the scattering process, an atom at position $\vec{r}_i$ in the cloud interacts with an incoming photon of wavevector $\vec{k}$ and therefore acquires (in the rotating frame) a static phase term $e^{i\vec{k}\vec{r}_i}$ in the collective state superposition $|\underline{e}\rangle$. After the scattering[3] of a photon in the direction of a wavevector $\vec{k}'$, the atomic ensemble is back in the collective ground state $|\underline{g}\rangle$ but with an additional phase. The cloud state is:

$$\left(\frac{1}{\sqrt{N}} \sum_{i=1}^{N} e^{i(\vec{k}-\vec{k}').\vec{r}_i} \right) |\underline{g}\rangle. \tag{1.7}$$

The global factor before $|\underline{g}\rangle$ gives the square root of the probability of this process. To benefit from the $\frac{1}{N}$ enhancement the phase term must be equal to

[3] We assume here an elastic Rayleigh scattering process and therefore the norm of $\vec{k}'$ is fixed, only its direction is a free parameter.

zero and therefore we must have $\vec{k} = \vec{k}'$. The probability of scattering is then maximum in the forward direction with the same wavevector $\vec{k}$ as the incident photon.

Decoherence

With these two configurations (Dicke states and collective enhancement) we have understood qualitatively why emission will be in the forward direction after scattering through atomic vapor. Obviously there are many restrictions to these simple explanations, because the phase coherence is not always conserved. These troublemakers are grouped under the term: decoherence.

One main reason for the decoherence will come from the fact that atoms are moving (and moving quite fast in a hot atomic vapor). Taking this into account, the position of re-emission for atom i will not be $\vec{r}_i$ and cancellation of the phase $e^{i(\vec{k}-\vec{k}').\vec{r}_i}$ will not be perfect anymore. This will be discussed in more detail in paragraph 1.1.4.

Another drawback with *real* atoms is that they often have more than one excited state with slightly different energies. If light couples to these states (even with different coupling constants), the atomic ensemble state will acquire a temporal phase of the order of $e^{i\Delta E t/\hbar}$ with ΔE being the characteristic energy difference between excited states. We will come back to this point when we will discuss 2-level atoms and rubidium D-lines (see paragraph 1.2.1).

1.1.3 What is a dense atomic medium ?

As an associate professor, I am member of a CNU (Conseil National des Universités) thematic section called *dilute media and optics.* Then why do I entitle this work "Quantum Optics in dense atomic medium". What does dense mean in this context ? I do not mean that I have been working with dense media in condensed matter sense (with the notable exception of section 4.4) but rather with an **optically dense** cloud. In the continuation I describe the relationship between temperature and atomic density in a warm vapor and the method to provide a good measure of the optical density: the optical depth.

Atomic density

A strong advantage of atomic vapors is that their density can be tuned at will by simply changing their temperature. As alkali vapors are not perfect gases, there is a correction to the Boyle law given by C. Alcock, V. Itkin and M. Horrigan in Ref. [7]. The vapor pressure p in Pascal is given by:

$$p(\text{Pa}) = 10^{A+\frac{B}{T}}, \tag{1.8}$$

with $A = 9.318$ and $B - 4040$ K. The atomic density n_{at} is then given by dividing the vapor pressure by k_B the Boltzmann constant times the temperature T:

$$n_{at} = \frac{p(\text{Pa})}{k_B T}. \tag{1.9}$$

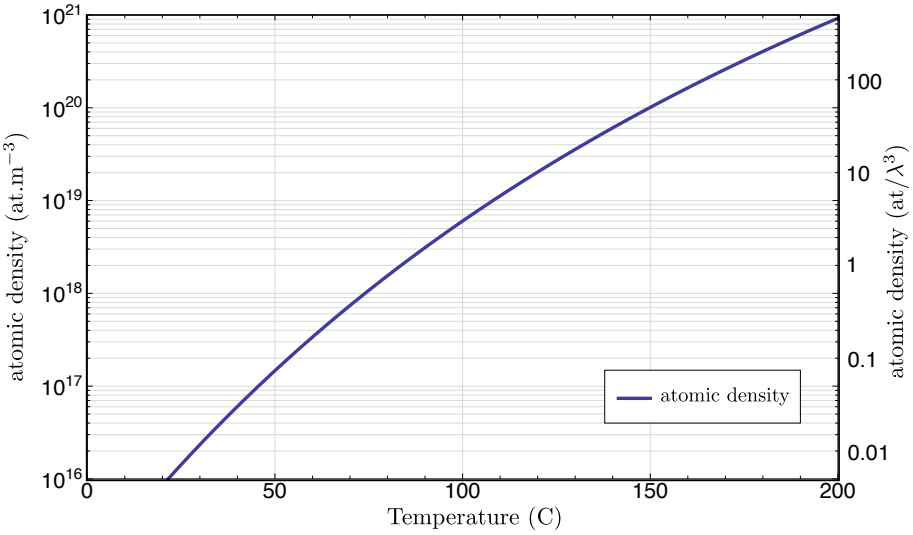

Figure 1.1: Atomic density of rubidium as function of temperature in Celsius. Right scale is given in unit of λ^3 for the D2 line.

Optical depth

Taking into account the density, light propagating in an atomic medium will have a linear absorption α given by:

$$\alpha = n_{at}\sigma_0. \tag{1.10}$$

The optical depth is simply defined as the product of α by L, the length of the atomic medium. Based on this definition we can directly write the Beer law of absorption for a beam of initial intensity I_0:

$$I = I_0 \exp\left[-\alpha L\right]. \tag{1.11}$$

For the D2 line of rubidium $\sigma_0 = 1.25 \times 10^{-9}$ cm^{-2}. We can note that the value is slightly different from Eq. 1.1 due to the multiplicity of atomic states.

Saturation intensity

This derivation is only valid on resonance and with a weak electromagnetic field. In fact, saturation can modify the behaviour of the medium. To quantify this effect, we introduce the saturation intensity I_{sat} which is defined as the value of intensity for which the cross section is reduced by half compared to the low intensity case. This leads to the redefinition of the atomic cross section σ as [8]:

$$\sigma = \frac{\sigma_0}{1 + I/I_{sat}}. \tag{1.12}$$

We can refine even more this model by adding a detuning $\Delta = \omega_L - \omega_0$ between the excitation (laser) field frequency and the atomic transition. In this case we have:

$$\sigma(\Delta) = \frac{\sigma_0}{1 + 4(\Delta/\Gamma)^2 + I/I_{sat}}. \tag{1.13}$$

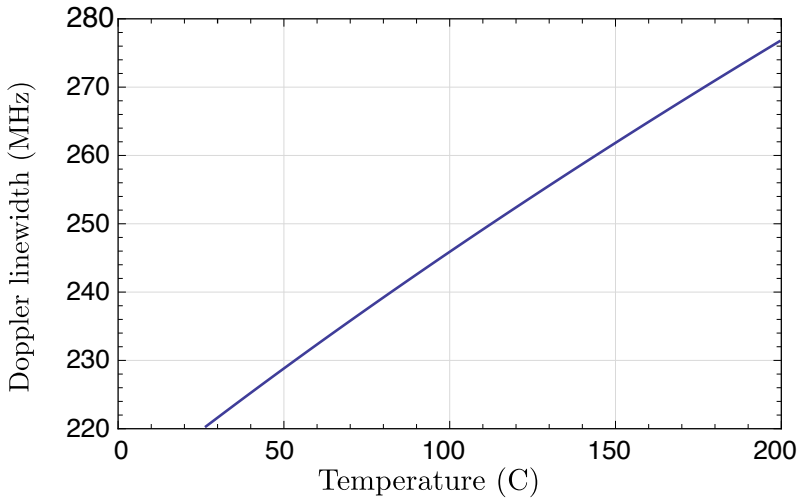

Figure 1.2: Doppler linewidth of rubidium D2 line as function of temperature.

The saturation intensity is defined for a resonant excitation. However, in practice, it is often useful to know if the atomic medium is saturated or not at a large detuning from the resonance. A simple way to obtain a quick insight on this question is defining an *off-resonance* saturation intensity $I_{sat}(\Delta)$. It is given by [8]:

$$I_{sat}(\Delta) = \left[1 + 4\frac{\Delta^2}{\Gamma^2}\right] I^0_{sat}, \tag{1.14}$$

with I^0_{sat} the resonant saturation intensity. We have then reformulated Eq. 1.12 with $I_{sat}(\Delta)$ instead of I_{sat}. We can remember that, when $I = I_{sat}(\Delta)$, the cross section is reduced by half compared to low intensity.

1.1.4 Doppler broadening

Unfortunately, in an atomic cloud, every atom does not contribute equally to the light-matter interaction. This is a consequence of the Doppler effect. Indeed, atoms moving at the velocity $\vec{v}$ will result to a frequency shift $\sim \vec{k}\vec{v}$. In a warm atomic vapor this effect is crucial to understand the dynamics of the system, as Doppler broadening can be much greater than the natural linewidth Γ. For an atom of a mass m at temperature T the Doppler linewidth Γ_D is given by:

$$\Gamma_D = \sqrt{\frac{k_B T}{m\lambda^2}}. \tag{1.15}$$

At 100°C, this gives $\Gamma_D \approx 250$ MHz for Rb D2 line, compared to $\Gamma \approx 6$ MHz.

An important consequence is that the atomic response, derived in the next section, will have to be integrated over the atomic velocity distribution to obtain quantitative predictions. We will not include this calculation here, as it adds unnecessary complexity but no immediate intelligibility. We refer the interested reader to [9, 10, 11]

1.2 Non-linear optics in dense atomic media

There is no two-level atom and rubidium is not one of them

William D. Phillips

This famous quote from Bill Phillips reminds us, that how useful can the two-level atom model be, it still remains simplistic compared to the complexity of alkali atomic structures. In this section, I briefly recall three important features of this model: linear absorption $\mathrm{Im}(\chi^{(1)})$, linear phase shift $\mathrm{Re}(\chi^{(1)})$ and non-linearity $\chi^{(3)}$ near a two-level atomic resonance. This well known derivation is an important concept settling the background of this work. Along this section I will highlight the theoretical tools one by one to progressively cover more and more complex situations. Specifically, we are in this work focusing on non-linear effects with large intensities. This means not only a large $\mathrm{Re}(\chi^{(3)})$ but also a large $\mathrm{Re}(\chi^{(3)}) \times I$.

Therefore I introduce:

- the saturation of non-linearity at larger intensity ($\chi^{(5)}$ correction term);
- the concept of electromagnetically induced transparency (EIT) and possible extension when the probe beam is not perturbative anymore;
- the process of four-wave-mixing.

1.2.1 2–level atoms

Let us consider the interaction of a monochromatic electric field with a system of N two-level atoms. This interaction process can be described by the optical Bloch equation [12]:

$$\frac{d\hat{\rho}}{dt} = -i\frac{i}{\hbar}\left[\hat{H}, \hat{\rho}\right] - \hat{\Gamma}\hat{\rho}, \tag{1.16}$$

where $\hat{\rho}$ is the density matrix of the atomic system, Γ is the decay rate of the excited state, $\hat{H} = \hat{H}_0 + \hat{V}$ is the Hamiltonian of the system with the non-perturbative part $\hat{H}_0$ and the interaction $\hat{V}$ which can be written as $\hat{V} = -\mathbf{d}\cdot\mathbf{E} = -\hbar\Omega/2$ in the dipole approximation. Ω is the Rabi frequency.

We can denote the ground and the excited state of the atom as $|g\rangle$ and $|e\rangle$ respectively with the resonant transition frequency ω_{eg}. With these notations we can rewrite the Bloch equation (1.16) for the slowly varying amplitudes $\sigma_{ij}(t)$ of the density matrix elements $\rho_{ij}(t) = \sigma_{ij}(t)\exp(-i\omega_{ij}t)$ in the following form:

$$\begin{aligned}
\dot{\rho}_{gg} &= i\frac{\Omega}{2}\left(\sigma_{ge} - \sigma_{eg}\right) + \Gamma\rho_{ee} \\
\dot{\rho}_{ee} &= -i\frac{\Omega}{2}\left(\sigma_{ge} - \sigma_{eg}\right) - \Gamma\rho_{ee} \\
\dot{\sigma}_{ge} &= -i(\Delta - i\Gamma/2)\sigma_{ge} - i\frac{\Omega}{2}\left(\rho_{ee} - \rho_{gg}\right),
\end{aligned} \tag{1.17}$$

where Ω is the Rabi frequency of the probe field and $\Delta = \omega - \omega_{eg}$ is the laser detuning from the excited state. To obtain this system of equations we have

applied the Rotating Wave Approximation (RWA). This approximation allows to eliminate the fast decaying terms and to rewrite the Bloch equation for slow-varying amplitudes [12]. The elements ρ_{gg} and ρ_{ee} correspond to population of the ground and the excited states respectively, while the elements $\sigma_{eg} = \sigma^*_{ge}$ correspond to the atomic coherence. We can rewrite the system of equations (1.17) as:

$$\begin{aligned} \dot{\rho}_{ee} - \dot{\rho}_{gg} &= -i\Omega\left(\sigma_{ge} - \sigma_{eg}\right) - \Gamma\left(\rho_{ee} - \rho_{gg} + 1\right) \\ \dot{\sigma}_{ge} &= -i(\Delta - i\Gamma/2)\sigma_{ge} - i\frac{\Omega}{2}\left(\rho_{ee} - \rho_{gg}\right), \end{aligned} \tag{1.18}$$

taking into account the condition that $\rho_{gg} + \rho_{ee} = 1$. Because the amplitudes ρ_{gg}, ρ_{ee} and σ_{eg} are slow-varying we can assume that $\dot{\rho}_{gg} = \dot{\rho}_{ee} = \dot{\sigma}_{ge} = 0$ and the solution of (1.18) can be found in the following form:

$$\begin{aligned} \sigma_{ge} &= -\frac{\Omega/2\left(\rho_{ee} - \rho_{gg}\right)}{\Delta - i\Gamma/2}, \\ \rho_{ee} - \rho_{gg} &= -\frac{\Delta^2 + \Gamma^2/4}{\Delta^2 + \Gamma^2/4 + \Omega^2/2}. \end{aligned} \tag{1.19}$$

The response of the medium on the interaction with light can be described in terms of the atomic polarization $\mathbf{P}$. The vector of polarization relates to the electric field with a proportional coefficient:

$$\mathbf{P} = \varepsilon_0 \chi \mathbf{E}, \tag{1.20}$$

where χ is the atomic susceptibility.

In general, if we neglect frequency conversion processes, the polarization $\mathbf{P}$ can be written as an expansion in Taylor series in the electric field as:

$$P = \varepsilon_0\chi^{(1)}E + \varepsilon_0\chi^{(2)}|E|^2 + \varepsilon_0\chi^{(3)}|E|^2\cdot E + \varepsilon_0\chi^{(4)}|E|^4 + \varepsilon_0\chi^{(5)}|E|^4\cdot E + ... \tag{1.21}$$

Here $\chi^{(1)}$ is known as a linear susceptibility, higher order terms are known as a second-order, a third-order, or n-order susceptibilities. In general, for anisotropic materials the susceptibility is a $(n-1)$-order rank tensor. In our consideration we expand the Taylor series up to the rank 5 to take into account the nonlinear response of the atomic medium. For a centro-symmetric medium, the even terms vanish and the polarization of the system can be written as [12]:

$$P = \varepsilon_0\chi^{(1)}E + \varepsilon_0\chi^{(3)}|E|^2 \cdot E + \varepsilon_0\chi^{(5)}|E|^4 \cdot E + ... \tag{1.22}$$

The polarization can be found in terms of the density matrix elements:

$$P = N\ \mu_{eg}\sigma_{ge}, \tag{1.23}$$

where μ_{eg} is the dipole moment of the transition. From this expression we can find a full polarization of the atomic system:

$$P = -\frac{N|\mu_{eg}|^2(\Delta + i\Gamma/2)}{\hbar(\Delta^2 + \Gamma^2/4 + \Omega^2/2)}E = -\frac{4N|\mu_{eg}|^2}{\hbar\Gamma^2}\cdot\frac{\Delta + i\Gamma/2}{1 + 4\Delta^2/\Gamma^2 + 2\Omega^2/\Gamma^2}E. \tag{1.24}$$

We can write P as function of the saturation intensity I_{sat} using:

$$\frac{I}{I_{\text{sat}}} = 2\left[\frac{\Omega}{\Gamma}\right]^2 \text{ with } I = \frac{1}{2}n_0\varepsilon_0 cE^2. \tag{1.25}$$

One obtains:

$$P = -\frac{4N|\mu_{eg}|^2}{\hbar\Gamma^2} \cdot \frac{\Delta + i\Gamma/2}{1 + 4\Delta^2/\Gamma^2 + I/I_{\text{sat}}} E. \tag{1.26}$$

We should note that the real part of the susceptibility corresponds to the refractive index of the medium, while the imaginary part gives information about the absorption.

Next we calculate the zeroth, first and second contributions to the polarization of a collection of two-level atoms. By performing a power series expansion of Eq. (1.26) in the quantity I/I_{sat}:

$$P \approx -\frac{4N|\mu_{eg}|^2}{\hbar\Gamma^2} \frac{\Delta + i\Gamma/2}{(1 + 4\Delta^2/\Gamma^2)} E \cdot \left[1 - \frac{I/I_{\text{sat}}}{1 + 4\Delta^2/\Gamma^2} + \frac{I^2/I_{\text{sat}}^2}{(1 + 4\Delta^2/\Gamma^2)^2}\right]. \tag{1.27}$$

We now equate this expression with Eq. 1.22 to find the three first orders of the atomic polarization:

$$\begin{aligned}
\varepsilon_0\chi^{(1)} &= -\frac{4N|\mu_{eg}|^2}{\hbar\Gamma^2} \cdot \frac{\Delta + i\Gamma/2}{(1 + 4\Delta^2/\Gamma^2)} \\
\varepsilon_0\chi^{(3)}|E|^2 &= \frac{4N|\mu_{eg}|^2}{\hbar\Gamma^2} \cdot \frac{\Delta + i\Gamma/2}{(1 + 4\Delta^2/\Gamma^2)} \cdot \frac{I/I_{\text{sat}}}{1 + 4\Delta^2/\Gamma^2} \\
\varepsilon_0\chi^{(5)}|E|^4 &= -\frac{4N|\mu_{eg}|^2}{\hbar\Gamma^2} \cdot \frac{\Delta + i\Gamma/2}{(1 + 4\Delta^2/\Gamma^2)} \cdot \frac{I^2/I_{\text{sat}}^2}{(1 + 4\Delta^2/\Gamma^2)^2}.
\end{aligned} \tag{1.28}$$

We introduce the usual[4] power series expansion:

$$\chi_{\text{eff}} = \chi^{(1)} + 3\chi^{(3)}|E|^2 + 10\chi^{(5)}|E|^4. \tag{1.29}$$

This notation allows us to write the effective refractive index n_{eff} as:

$$n_{\text{eff}}^2 = 1 + \chi_{\text{eff}}. \tag{1.30}$$

We use the standard definition [12] of the non-linear indices (n_2 and n_3) : $n_{\text{eff}} = n_0 + n_2 I + n_3 I^2$ and we can expand n_{eff}^2 in:

$$n_{\text{eff}}^2 = n_0^2 + 2n_0 n_2 I + (2n_0 n_3 + n_2^2) I^2. \tag{1.31}$$

We can then connect the indices to the expression of $\text{Re}(\chi)$. We show the scaling of $\text{Re}(\chi)$ in Figure 1.3.

$$\begin{aligned}
n_0 &= \sqrt{1 + Re\left[\chi^{(1)}\right]}, \\
n_2 &= \frac{3Re\left[\chi^{(3)}\right]}{n_0^2 \varepsilon_0 c}, \\
n_3 &= \frac{20Re\left[\chi^{(5)}\right]}{n_0^3 \varepsilon_0^2 c^2} - \frac{n_2^2}{2n_0}.
\end{aligned} \tag{1.32}$$

[4]The coefficients 1, 3 and 10 are used because we are only concern with the non-linear effects conserving the input frequency. For example the $\chi^{(3)}$ term can lead to several frequency conversion, and we only keep triplets like: $(+\omega, +\omega, -\omega)$, $(+\omega, -\omega, +\omega)$ and $(-\omega, +\omega, +\omega)$. This coefficient is given by the binomial coefficient $\binom{3}{2}$.

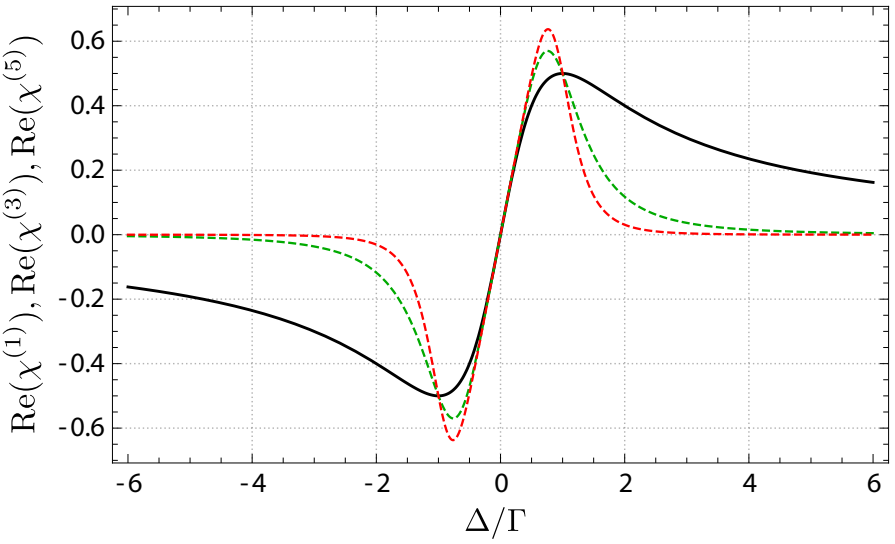

Figure 1.3: $\mathrm{Re}(\chi^{(1)})$ in black ,$\mathrm{Re}(\chi^{(3)})$ in dashed green,$\mathrm{Re}(\chi^{(5)})$ in dashed red

What to optimize ?

When looking at the previous derivation of the non-linear susceptibility, we see that 3 different quantities can be optimized depending on the goal of your experiments.

- If you want to observe non-linear effects at the single photon level, for example to create a photonic transistor, you want to optimize the value of $\mathrm{Re}\left[\chi^{(3)}\right]$ in the limit $I \ll I_{sat}$;
- If you want to observe dispersive effects as slow and fast light propagation, you will want to optimize the value of derivative of $\mathrm{Re}[\chi]$ as function of the frequency. This is the configuration we will study in chapter 3;
- If you are interested in a large value for $\Delta n = n_2 \times I$, you have access to 2 knobs: increasing n_2 or increasing I. However you must stay within the limit of $I < I_{sat}$ otherwise the Taylor expansion does not hold anymore. That is why we have done the calculation to the next order I/I_{sat}. This is the configuration we will study in chapter 4.

Scaling for effective 2-level atoms.

We briefly review the dispersive limit. When the laser is detuned far enough from the atomic transition, we have a simplification of the atomic response.

First, the approximation of the 2-level atoms becomes more precise because the contribution from all the levels averages to an effective contribution. This is the case when the detuning Δ is much larger than the hyperfine splitting energy scale (typically around ~ 500 MHz for Rb).
The second consequence is that the absorptive part of the susceptibility $\mathrm{Im}(\chi)$ becomes negligible with respect to the dispersive part $\mathrm{Re}(\chi)$. In this limit, the

medium is virtually transparent but there is still a non-negligible phase shift (a linear and a non-linear one). At $\Delta \gg \Gamma$, we can simplify Eq. 1.28 to obtain for the linear part of the absorption:

$$\text{absorption: } \mathrm{Im}(\chi^{(1)}) \propto \frac{N}{\Delta^2}, \tag{1.33}$$

and for the non-linear dispersive part:

$$\text{phase shift: } \mathrm{Re}(\chi^{(3)}) \propto \frac{N}{\Delta^3}. \tag{1.34}$$

The non-linear absorption is neglected as it scales with $\frac{1}{\Delta^4}$, as well as the linear phase shift which just results in a redefinition of the phase reference.

In the far detuned limit, an intuitive idea to improve the non-linear phase shift is to simply increase the atomic density, by rising the cloud temperature as described in section 1.1.3. This is indeed true as $\mathrm{Re}(\chi^{(3)})$ scales with N. However, this is often critical to conserve a large (fixed) transmission while increasing the non-linear phase shift. This condition of fixed transmission means that $\frac{N}{\Delta^2}$ is a constant. In other words, we can rewrite the phase shift $\mathrm{Re}(\chi^{(3)})$ as this constant times $\frac{1}{\Delta}$.

We see that the intuitive vision is no longer valid if we want to keep a fixed transmission: to maximize the phase shift at a given transmission it is therefore favorable to reduce Δ, which in consequence leads to a lower temperature (to keep $\frac{N}{\Delta^2}$ constant). This is obviously limited by the initial hypothesis of far detuned laser ($\Delta \gg \Gamma$).

In order to verify this model we have measured the non-linear phase shift for various temperatures and detuning and this is reported in chapter 4. In the next paragraph, I explain how to conduct this measurement.

Measurement of the non-linear phase shift for effective 2-level atoms.

The typical method to measure the non-linear phase shift of a sample is to realize a z-scan experiment [13, 14]. However this technique works better with a thin layer of material. For thick samples, we can use a technique demonstrated in Ref. [15]. This allows to measure the accumulated phase $\Delta\phi$ along the propagation. The phase accumulated can be written as:

$$\Delta\phi(r) = k \int_{z_0}^{z_0+L} n_2 I(r,z) dz, \tag{1.35}$$

with z_0 is the coordinate of the front of the sample and L is its length. The intensity profile of the beam can then be replaced by the Gaussian profile of a TEM(0,0) beam at the input plane. We obtain:

$$\Delta\phi(r) = k \int_{z_0}^{z_0+L} n_2 \Delta\phi(r) \frac{w_0^2}{w(z)^2} e^{-2r^2/w(z)^2} dz, \tag{1.36}$$

with w_0 is the waist radius, $w(z) = w_0\sqrt{1+\left(\frac{z}{z_R}\right)^2}$ and $z_R = \frac{\pi w_0^2}{\lambda}$. It is then possible to derive the far field diffraction pattern in the Fraunhofer limit (see

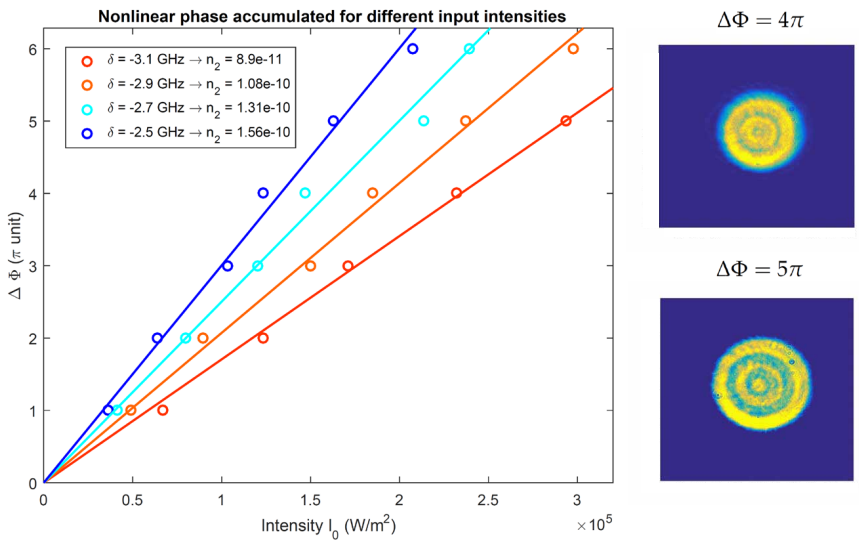

Figure 1.4: Typical non-linear phase shift measurement for effective 2-level atomic cloud. Detuning δ is given to D1 Rb85 line. Cell temperature is 130C. For larger intensity a clear deviation is observed due to n_3 term (not shown). Insets are examples of obtained far field measurements.

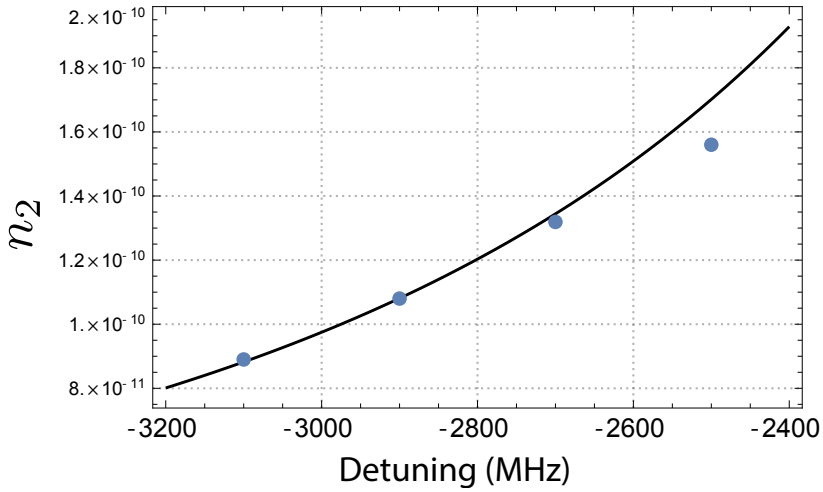

Figure 1.5: Comparison between 2-level atoms model and experimental measurement of n_2. Blue dots are experimental data presented in Fig. 1.4, and black line is the model of Eq. 1.32. The model is scaled by the atomic density which is a fitting parameter.

Ref. [15] for details). From Eq. 1.36, it is clear that the phase shift in the center : $\Delta\phi(r=0)$ is directly proportional to n_2 and the central intensity $I(0,0)$. We will therefore observe a switch from a bright spot to dark spot in the center of the diffraction pattern when the phase is modified by π and back to a bright spot again for a phase change of 2π. By simply counting the number of rings N_{Rings} that appear while slowly increasing $I(0,0)$, we can estimate the non-linear phase shift accumulated along z. In the limit of long Rayleigh length ($z \ll z_R$) we can approximate Δn to:

$$\Delta n = n_2 I \simeq \frac{\lambda}{L} N_{Rings}. \tag{1.37}$$

In Figure 1.4, I present an experimental characterization of n_2 for rubidium 85. From this figure, we have extracted the value of n_2 as function of the detuning from the atomic transition. To validate the 2-level atoms model, I plot in Figure 1.5, the results of the numerical model (Eq. 1.32) after integration over the Doppler profile and compare it to the experimental data. We see that for large detuning the model is in excellent agreement. However as we get closer to the resonance the contribution of the $\chi^{(5)}$ term start to be not negligible anymore and n_2 is reduced[5] compared to the value predicted by $\chi^{(3)}$. This is the main limitation to obtain a larger $\Delta n = n_2 I$ in experiments.

To get a better understanding of this effect we have compared $\chi^{(5)} I^2$ and $\chi^{(3)} I$ for the two-level model. We see in Fig. 1.6, that the contribution of $|\chi^{(5)} I^2|$ is huge when we get closer to resonance but at detuning larger than 2.5 GHz, it can be safely neglected at this intensity.

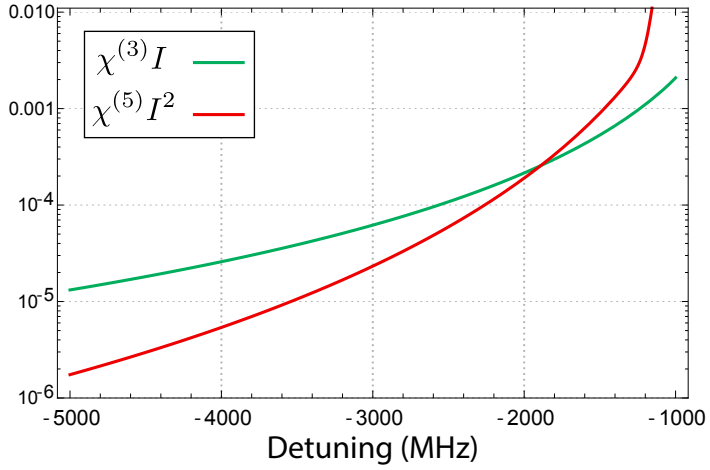

Figure 1.6: Comparison between $|\chi^{(5)} I^2|$ and $|\chi^{(3)} I|$. Here $I = 2.10^5$ W/m^2 (which is still much smaller than the effective saturation intensity at this detuning).

[5] $\chi^{(3)}$ and $\chi^{(5)}$ are of opposite signs.

1.2.2 Electromagnetically induced transparency

In the previous section we have discussed non-linearity in a 2-level atoms model. If we add one more level, more complex schemes using atomic coherences can be exploited. Here, I briefly describe the interaction of the system of 3-level atoms with two electromagnetic fields in order to study the effect of *electromagnetically induced transparency* (EIT) [16, 17].

The interaction process can be described by the evolution of the optical Bloch equations, as it was done in the section 1.2.1. The three levels are noted: $|g\rangle$ for ground, $|e\rangle$ for excited, $|s\rangle$ for supplementary third level. The optical Bloch equation (1.16) can be rewritten for slowly-varying amplitudes in the case of a 3-level atom as following [9, 12]:

$$\begin{aligned}
\dot{\rho}_{gg} &= i\frac{\Omega_p}{2}(\sigma_{ge}-\sigma_{eg})+\Gamma_{eg}\rho_{ee} \\
\dot{\rho}_{ss} &= i\frac{\Omega_c}{2}(\sigma_{se}-\sigma_{es})+\Gamma_{es}\rho_{ee} \\
\dot{\rho}_{ee} &= -i\frac{\Omega_p}{2}(\sigma_{ge}-\sigma_{eg})-i\frac{\Omega_c}{2}(\sigma_{se}-\sigma_{es})-\Gamma\rho_{ee} \\
\dot{\sigma}_{ge} &= -i(\Delta_p-i\Gamma/2)\sigma_{ge}-i\frac{\Omega_p}{2}(\rho_{ee}-\rho_{gg})+i\frac{\Omega_c}{2}\sigma_{gs} \\
\dot{\sigma}_{se} &= -i(\Delta_c-i\Gamma/2)\sigma_{se}-i\frac{\Omega_c}{2}(\rho_{ee}-\rho_{ss})+i\frac{\Omega_p}{2}\sigma_{sg} \\
\dot{\sigma}_{gs} &= -i(\Delta_p-\Delta_c-i\gamma_0)\sigma_{gs}-i\frac{\Omega_p}{2}\sigma_{es}+i\frac{\Omega_c}{2}\sigma_{ge}.
\end{aligned} \tag{1.38}$$

Here we characterize two electromagnetic fields: the probe field with the Rabi frequency Ω_p interacts between the initially populated ground state $|g\rangle$ and the excited state $|e\rangle$, while the control field with the Rabi frequency Ω_c couples the excited state $|e\rangle$ with the initially empty second ground state $|s\rangle$. The probe and the control fields are detuned from the corresponding atomic resonances with detunings $\Delta_p=\omega_p-\omega_{eg}$ and $\Delta_c=\omega_c-\omega_{es}$ respectively. Decay rates Γ_{eg} and Γ_{es} can be found with the Clebsch-Gordan coefficients of the corresponding transitions, and they satisfy to the condition $\Gamma_{eg}+\Gamma_{es}=\Gamma$. The decay rate γ_0 corresponds to the decay rate of the ground states coherence between $|g\rangle$ and $|s\rangle$.

In the RWA we assume ρ_{ii} and σ_{ij} as slowly varying amplitudes. With these conditions the system (1.38) can be solved in the steady-state regime when

$$\dot{\rho}_{gg}=\dot{\rho}_{ee}=\dot{\rho}_{ss}=\dot{\sigma}_{ge}=\dot{\sigma}_{se}=\dot{\sigma}_{gs}=0.$$

In the following, we are interested in the nonlinear components of the atomic susceptibility χ, which is the proportionality coefficient between the atomic polarization and the electric field, see Eq. 1.20. We solve the system (1.38) numerically. The polarization induced by the probe field can be found in terms of the coherence at the corresponding atomic transition σ_{ge}, in the same way how it was done in Eq. 1.23.

We can extract quantities similar to 2-level atoms: $\chi^{(1)},\chi^{(3)},\chi^{(5)}$ from a linear expansion of χ obtained numerically. The code to implement these simulations in Mathematica is available here.

1.2.3 Four-wave-mixing

Adding one more level, one can add even more complexity (and also more fun) in the light-matter interactions. I describe here, a typical configuration called double-Λ, where two intense pumps, one probe beam and one conjugate beam interact (see Figure 1.7). A lot of details about this configuration can be found in [18, 19, 20, 21, 22, 23, 24].

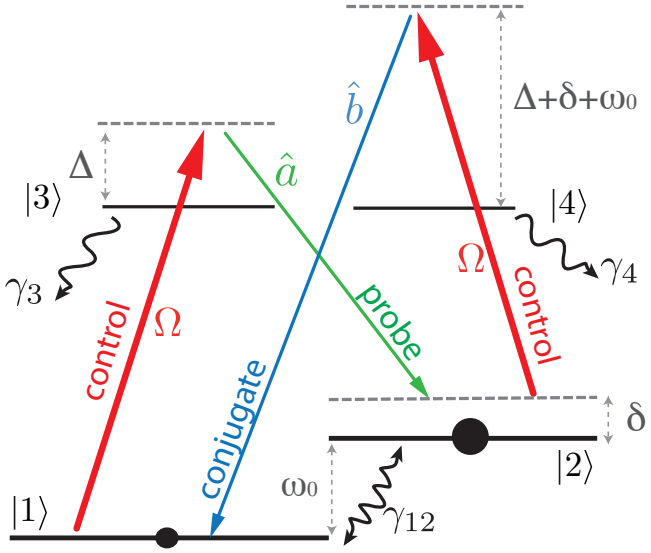

Figure 1.7: Levels scheme for four-wave-mixing in the double-Λ configuration.

Here, I will just give an intuitive description of a few phenomenon. One important point to understand, is there is only one pump laser in real experimental configuration. So if it is detuned by Δ from the transition $|1\rangle \rightarrow |3\rangle$ it has to be detuned by $\Delta+\omega_0$ from the transition $|2\rangle \rightarrow |4\rangle$. If $\Delta > 0$ and $\Delta \gg \Gamma$, it directly implies a steady state for the population with a large amount of the atoms in state $|2\rangle$.
An interesting approach, to understand the quantum correlations which appears between the probe and conjugate is to think of four-wave-mixing as a DLCZ memory protocol [25]. Indeed, one starts with all the population in $|2\rangle$. Sometimes (not often because of the large detuning) a $|2\rangle \rightarrow |4\rangle$ pump photon will *write* his phase in the atomic coherence and induce the emission of an anti-Stokes (conjugate) photon. In the DLCZ [25] language, when this anti-Stokes (conjugate) photon is detected it implies that the memory has been loaded. After a given time, the memory can be read (efficiently due to small detuning) by a pump photon on the $|1\rangle \rightarrow |3\rangle$ transition. This process is accompanied by the emission of a probe photon, in a coherent manner (as describe in section 1.1.2).

In chapter 3, I use this technique to generate entangled pulses of light between the probe and the conjugate [20]. I also use another property of this system: to provide small group velocity and anomalous dispersion, in order to observe slow and fast light [26].

1.2.4 Slow and fast light

We begin by applying the curl operator to the Maxwell equations to obtain the Helmholtz equation

$$(\nabla^2 E + k^2)\mathbf{E} = 0, \tag{1.39}$$

where we have $k = \mu_0\epsilon_0\epsilon_r\omega^2$. As usual we assume the beam to propagate along the $+z$ direction and we ignore polarization. Solutions of the Helmholtz equation that fulfills these conditions are:

$$E(z,t) = E_0(z)e^{i(kz-\omega t)}. \tag{1.40}$$

The phase velocity is defined as the velocity at which the phase of this solution moves:

$$v_\phi = \frac{\omega}{k} \tag{1.41}$$

By replacing k with its definition, it can be rewritten with the speed of light in vacuum c and the index of refraction n:

$$v_\phi = \frac{\omega}{\sqrt{\mu_0\epsilon_0\epsilon_r(\omega)\omega^2}} = \frac{c}{n(\omega)}. \tag{1.42}$$

This is a well known result but it hides in the dependency on ω of $\epsilon_r(\omega)$ that different frequency will propagate at different velocities. It has no consequence for monochromatic waves, but it implies that a pulse will distort while propagating in a dispersive media. Slow and fast light terminology comes from this effect: a light pulse (basically a wave-packet) that propagates slower than c will be qualified as slow-light and reciprocally if it does propagate faster than c it will be qualified as fast-light [27, 28]. Let us precise this terminology.

A wavepacket has the general form:

$$E(z,t) = \int E_0(k)e^{i(kz-\omega(k)t)}\mathrm{dk}, \tag{1.43}$$

where $E_0(k)$ is the Fourier transform of $E_0(z)$ at $t = 0$. If the spectrum $E_0(k)$ is sufficiently narrowband (i.e. the pulse is not too short), we can call the central value k_c and Taylor expand ω around k_c:

$$\omega(k) \approx \omega_c + \left.\frac{\partial\omega}{\partial k}\right|_{k=k_c}(k-k_c). \tag{1.44}$$

Using this approximation we can write:

$$E(z,t) \approx E\left(z - t\left.\frac{\partial\omega}{\partial k}\right|_{k_c}, 0\right) \times e^{i(k_c\left.\frac{\partial\omega}{\partial k}\right|_{k_c}-\omega_c)t}. \tag{1.45}$$

In this simple results we can see that the pulse will propagate largely undistorted (up to an overall factor phase and as long as Eq. 1.44 is a good approximation) at the group velocity given by:

$$v_g = \left.\frac{\partial\omega}{\partial k}\right|_{k_c}. \tag{1.46}$$

As derived previously about 2-level atoms, it is often more convenient to express the group velocity as a function of the variation of n with frequency. We have

$$\begin{aligned} \frac{\partial \omega}{\partial k} &= \frac{c}{n} - \frac{ck}{n^2}\frac{\partial n}{\partial k} \\ &= \frac{c}{n} - \frac{\omega}{n}\frac{\partial \omega}{\partial k}\frac{\partial n}{\partial \omega}. \end{aligned} \tag{1.47}$$

We can then write the group velocity:

$$v_g = \frac{c}{n(\omega_c) + \omega_c \left.\frac{\partial n}{\partial \omega}\right|_{\omega_c}}. \tag{1.48}$$

This equation gives us direct access of the group velocity if we know $n(\omega_c)$ (which is the case now that we master optical Bloch equations). The group velocity is then given by the speed of light in vacuum divided by a term that includes both the index of refraction at the carrier frequency and the derivative of the index around the carrier frequency. The denominator is commonly called the group index n_g and it can take values larger or smaller than unity [29].

In the vast majority of dielectric media, far away from resonance, $\left.\frac{\partial n}{\partial \omega}\right|_{\omega_c}$ is usually positive and $n_g > 1$. However, it is possible (using EIT for example) to obtain $\left.\frac{\partial n}{\partial \omega}\right|_{\omega_c} < 0$. This type of medium is said to have *anomalous dispersion*. For sufficiently large negative value, it is possible to reach $n_g < 1$: a negative group velocity. I report on the use of this type of medium in chapter 3.

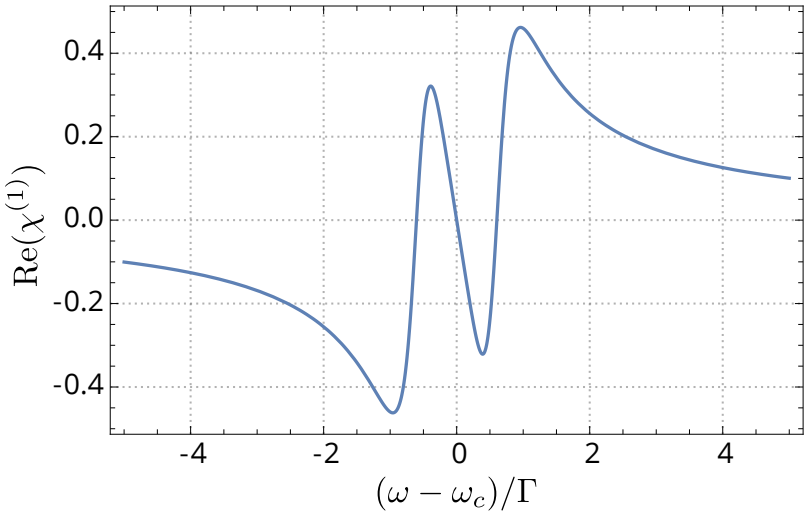

Figure 1.8: Real part of the the linear refractive index for the EIT configuration described in section 1.2.2. We can see that around $\omega - \omega_c = 0$ the slope of $\frac{\partial n}{\partial \omega}$ is large and negative. This is a perfect place of observe a negative group velocity.

Chapter 2

Multimode optical memory

List of publications related to this chapter :

- **Temporally multiplexed storage of images in a gradient echo memory**.
  Q. Glorieux, J. B. Clark, A. M. Marino, Z. Zhou, and P. D. Lett.
  Optics Express **20**, 12350 (2012)

- **Gradient echo memory in an ultra-high optical depth cold atomic ensemble**.
  B. M. Sparkes, J. Bernu, M. Hosseini, J. Geng, **Q. Glorieux**, P. A. Altin, P. K. Lam, N. P. Robins, and B. C. Buchler.
  New Journal of Physics **15**, 085027 (2013)

- **Spatially addressable readout and erasure of an image in a gradient echo memory**.
  J. B. Clark, **Q. Glorieux** and P. D. Lett.
  New Journal of Physics **15**, 035005 (2013)
  Not included.

- **An ultra-high optical depth cold atomic ensemble for quantum memories**.
  B. M. Sparkes, J. Bernu, M. Hosseini, J. Geng, **Q. Glorieux**, P. A. Altin, P. K. Lam, N. P. Robins, and B. C. Buchler.
  Journal of Physics, **467**, 012009 (2013)
  Not included.

2.1 Gradient Echo Memory

Light in vacuum propagates at c. This statement is not only a fundamental principle of physics it is also the foundation of the definition of the meter in the international system of units. Delaying [30], storing [31] or advancing [32] light are therefore only possible in a medium (i.e. not in vacuum). In the next two chapters, I will show how to play with the speed of light in a optically dense atomic medium [33].

The main motivation to delay or store photons in matter is the need to synchronize light-based communication protocols. Quantum technologies promise an intrinsically secure network of long distance quantum communication. However for a realistic implementation, the *quantum internet* will need quantum repeaters in order to compensate losses in long distance channels [34]. The core element of a quantum repeater is a quantum memory [35] which can store and release photons, coherently and on demand. This chapter is covering this topic with the presentation of an important memory protocol: the gradient echo memory and two implementations of this protocol one in a warm vapor [36] and the second in a cold atomic cloud [37].

If you are somewhat familiar with MRI, understanding qualitatively gradient echo memory (GEM) is straightforward. Imagine you want to encode quantum information in a light. Various approaches are available (from polarization encoding, time-bin, orbital angular momentum...) but for qubit encoding (i.e. an Hilbert space of dimension 2), you always can map your information into a spin 1/2 system and represent it on the Bloch sphere. Let's say your information is of the generic form $|\psi\rangle = \frac{1}{\sqrt{2}}\left(|0\rangle + e^{i\phi}|1\rangle\right)$, this means on the equator of the Bloch sphere with a latitude ϕ as shown on Fig. 2.1 i). In GEM, during the storage process one applies a spatially dependant energy shift in order to enlarge the transition [38, 39]. This technique enables the storage of photons with a broad spectrum (i.e. short in time).

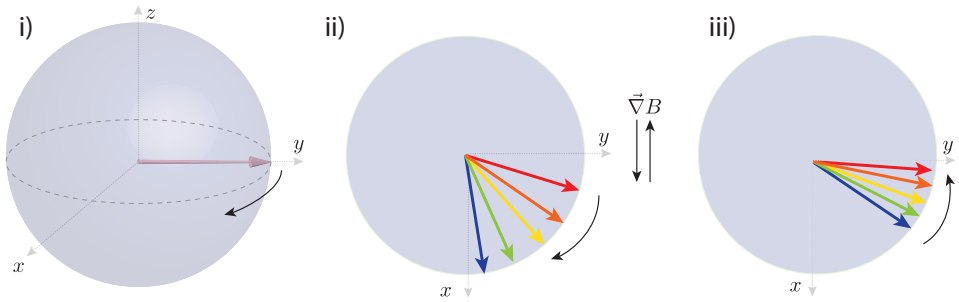

Figure 2.1: GEM protocol. i) Bloch sphere with the state initialized on the equator. ii) and iii) are views from top of the equatorial plan. ii) Dephasing with the gradient in one direction. iii) Rephasing with the gradient in the other direction. The dephasing is shown in the rotating frame.

Because $|\psi\rangle$ is not the energy ground state, the state will start to rotate in the equatorial plane of the Bloch sphere. However, due to the spatially dependant energy shift, each frequency component will rotate at a different speed and

dephase as shown in figure 2.1 ii) The trick used in gradient echo techniques is to reverse the time evolution of the dephasing process. By simply inverting the energy gradient after the evolution time T, we can see on figure 2.1 iii) that the frequency components will start to precess in the opposite direction with opposite speed[1]. At a time $2T$, all frequency components will be in phase again and the collective enhancement described in chapter 1 can occur.

Various approaches have been tested to produce a spatially varying energy shift. The two most successful techniques are using an AC-Stark shift in rare-earth crystal and using a Zeeman shift on atomic vapors by applying a magnetic field gradient. In this chapter I describe the Zeeman shift implementation in warm and cold atomic ensembles [40, 36, 37].

2.1.1 Storage time and decoherence

I should now describe how to convert coherent light excitation into a matter excitation. In the two-level-atom configuration, a quantum field $\hat{\mathcal{E}}(z,t)$ (carrying the information) is sent into the atomic vapor with ground state $|g\rangle$ and excited state $|e\rangle$.

Here, we are focusing on the propagation of a light pulse into a medium, therefore the time derivative terms in the Maxwell-Bloch equations have to be conserved, but the transverse gradient is neglected[2]. Using the rotating wave approximation described in chapter 1, and in the presence of a spatially varying magnetic field, the evolution equations are given by:

$$\begin{aligned} \frac{\partial}{\partial t}\hat{\sigma}_{ge}(z,t) &= [-\Gamma + i\eta(t)z]\hat{\sigma}_{ge}(z,t) - ig\hat{\mathcal{E}}(z,t) \\ \left(\frac{\partial}{\partial t} + c\frac{\partial}{\partial z}\right)\hat{\mathcal{E}}(z,t) &= igN\hat{\sigma}_{ge}(z,t). \end{aligned} \tag{2.1}$$

We have introduced the term $i\eta(t)z$ which represents the energy shift form the spatially varying magnetic field. $\eta(t)$ is the gradient slope that can be inverted (or modified in a more complex manner) at the desired time. From this coupled equations it is straightforward to point out the problem of the two-level-atom configuration. The information is transferred from the field to the atomic coherence $\hat{\sigma}_{ge}(z,t)$. However this coherence will decay with the decay rate of the excited state Γ. This is a terrible problem for a quantum memory ! The good news is: this problem can be solved using a third level.

The solution comes from mapping the photonic excitation into the ground state coherence of a three-level atom as discussed in section 1.2.2. Using a two-photon detuning equal to zero and a large one photon detuning compared to Γ, it is possible to apply the adiabatic elimination of the excited state and rewrite the evolution equation for the ground state coherence in a way similar

[1] This is true if not only the energy gradient is switched but also the sign of the energy. If only the energy gradient changes sign, the components will still precess in the same direction but the slowest components will become the fastest.

[2] The opposite approximation is done in the Chapter 4, where the time evolution is not considered but the diffraction in the transverse plan is.

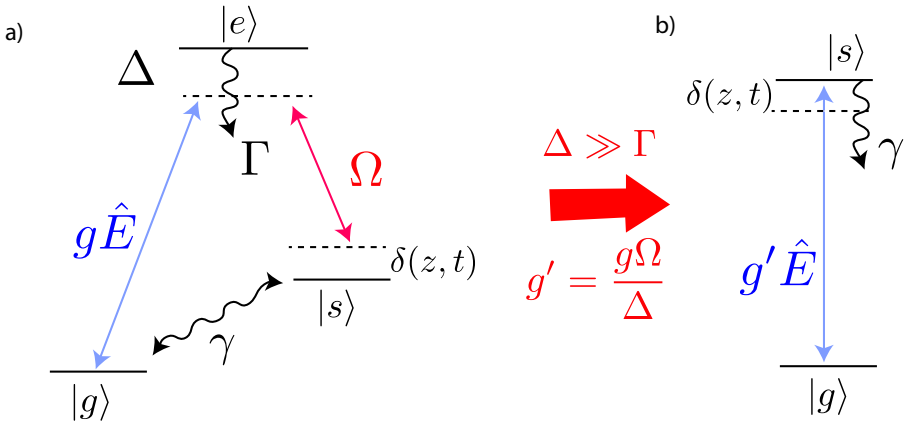

Figure 2.2: Adiabatic elimination notation summary.

to equations 2.1:

$$\begin{aligned} \frac{\partial}{\partial t}\hat{\sigma}_{gs}(z,t) &= [-\gamma + i\eta(t)z - i\frac{\Omega^2}{\Delta}]\hat{\sigma}_{gs}(z,t) - i\frac{g\Omega}{\Delta}\hat{\mathcal{E}}(z,t) \\ \left(\frac{\partial}{\partial t} + c\frac{\partial}{\partial z}\right)\hat{\mathcal{E}}(z,t) &= i\frac{g^2N}{\Delta}\hat{\mathcal{E}}(z,t) + i\frac{gN\Omega}{\Delta}\hat{\sigma}_{gs}(z,t). \end{aligned} \tag{2.2}$$

We apply a transformation to this equations by going into the rotating frame at frequency $\frac{g^2N}{\Delta}$. Moreover we neglect the ac-Stark shift induced by the control field and we finally obtain [40, 41]:

$$\begin{aligned} \frac{\partial}{\partial t}\hat{\sigma}_{gs} &= [-\gamma + i\eta(t)z]\hat{\sigma}_{gs} - i\frac{g\Omega}{\Delta}\hat{\mathcal{E}} \\ \left(\frac{\partial}{\partial t} + c\frac{\partial}{\partial z}\right)\hat{\mathcal{E}} &= i\frac{g\Omega N}{\Delta}\hat{\sigma}_{gs}. \end{aligned} \tag{2.3}$$

We found an equation similar to Eq. 2.1 but where the decoherence Γ has been replaced by γ which is the long-lived coherence between the two ground states. This is a major improvement as the ground state coherent is immune from spontaneous emission, and therefore much longer memory time can be envisioned (and demonstrated actually [42]). Another important improvement is obtained by going to three levels and modifying the coupling g to $\frac{g\Omega}{\Delta}$, which can be modified and tuned with the Rabi frequency of the control field.

A final transformation [26] is made to the equations 2.3 by changing z to the retarded frame $z' = z + ct$:

$$\begin{aligned} \frac{\partial}{\partial t}\hat{\sigma}_{gs} &= [-\gamma + i\eta(t)z]\hat{\sigma}_{gs} - i\frac{g\Omega}{\Delta}\hat{\mathcal{E}} \\ \frac{\partial}{\partial z'}\hat{\mathcal{E}} &= iN\frac{g\Omega}{\Delta}\hat{\sigma}_{gs}. \end{aligned} \tag{2.4}$$

2.1.2 GEM polaritons

Equations 2.4 can be solved numerically but new insights emerge when writing them in the picture of normal modes called GEM-polaritons [39, 43]. The polari-

ton picture for light-matter interaction in a 3-level system has been pioneered by Lukin and Fleischhauer with the introduction of the dark-state polariton [6]. This pseudo particle is a mixed excitation of light and matter (atomic coherence) where the relative weight can be manipulated with the external control field. This is a boson-like particle which propagates with no dispersion and a tunable group velocity. It is possible to consider a similar approach for GEM. Neglecting the decoherence and taking the spatial Fourier transform of Eq. 2.4, we can write [43]:

$$\begin{aligned} \frac{\partial}{\partial t}\hat{\sigma}_{gs}(t,k) &= -\eta\frac{\partial}{\partial k}\hat{\sigma}_{gs}(t,k) + i\frac{g\Omega}{\Delta}\hat{\mathcal{E}}(t,k) \\ k\hat{\mathcal{E}}(t,k) &= N\frac{g\Omega}{\Delta}\hat{\sigma}_{gs}(t,k). \end{aligned} \tag{2.5}$$

In analogy to [6], we consider the polariton-like operator in k-space:

$$\hat{\psi}(k,t) = k\hat{\mathcal{E}}(t,k) + N\frac{g\Omega}{\Delta}\hat{\sigma}_{gs}(t,k). \tag{2.6}$$

This particle will follow an equation of motion:

$$\left(\frac{\partial}{\partial t} + \eta(t)\frac{\partial}{\partial k} - iN\frac{g^2\Omega^2}{\Delta^2 k}\right)\hat{\psi}(k,t) = 0 \tag{2.7}$$

This equation indicates that $|\psi(k,t)|$ propagates un-distorted along the k-axis with a speed defined by the gradient η. We are here in front of a strange polariton.

The first difference with dark-state-polariton is that it does propagate in the k-plane instead of the normal space.

The second difference, maybe more fundamental is that the weight of one of the two components depends on k. If the polariton is normalized (and it has to be, in order to fulfill the bosonic commutation relation), lower spatial frequencies (short k) will be more an atomic excitation and higher spatial frequencies will be more a field excitation. We see here the limit of the analogy with the dark-state polariton. The GEM polariton picture is mainly useful to understand that the velocity of the pseudo particle is given by $\eta(t)$ and therefore will change sign when $\eta(t)$ will be flipped. We have here another interpretation of the rephasing process explained with the Bloch sphere, earlier in the chapter.

2.1.3 GEM in rubidium vapor

I give here a short description of the implementation of GEM in a hot Rubidium 85 vapor. More details are given in the article: *Temporally multiplexed storage of images in a gradient echo memory*, attached to this work [36]. The first task is to isolate a pair of ground states that can be individually addressed by light fields and whose energy splitting can be tuned by a linear Zeeman shift. This is done by applying a bias magnetic field (about 50 G) to lift the degeneracy of the m_F sub-levels for F=2 and F=3 ground states (see figure 2.3).
The second step is to apply a gradient magnetic field along the atomic vapor (a 20 cm long cell) to control the inhomogeneous broadening of the two-photon Raman transition. The amplitude of this gradient field must be smaller than the bias field and large enough to accept the full bandwidth of the light pulse

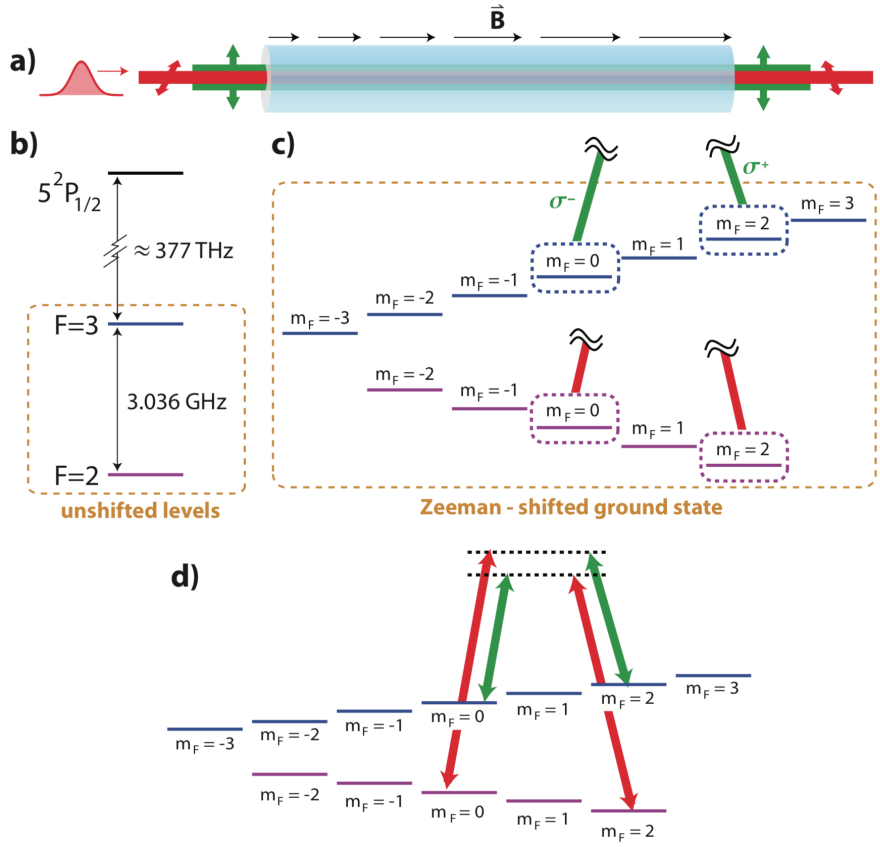

Figure 2.3: a) Orthogonal linearly polarized Raman beams used in the Λâ“GEM experiments presented in this thesis. When propagating along the direction of the magnetic field, a linear polarization can be viewed as a superposition of $\sigma+$ and $\sigma-$ polarizations. We therefore simultaneously drive two Raman transitions in any given echo experiment. b) An unshifted hyperfine structure for the D1 transition in 85Rb. c) A weak bias magnetic field to Zeeman shift the hyperfine structure of the ground state. In the weak field limit, the m_F levels are linearly and oppositely shifted in the F = 2 and F = 3 manifolds. For the Îâ“GEM protocol, we couple $m_F = 2$ and $m_F = 0$ magnetic sublevels. d) Complete depiction of the two Raman transitions. Figure and caption are extracted from the J. Clark thesis [26], whom I supervised at NIST.

we expect to store. Typically, in rubidium a rule of thumb is a Zeeman shift of 1 MHz per Gauss. So a gradient with 1 Gauss amplitude already allows for the storage of 1 microsecond Gaussian pulses.
An important part of the development of such setup consists in the precise control of the gradient and the ability to reverse it quickly. Indeed in the echo description we have done so far, the inversion of the gradient is supposed to be instantaneous. It is clear that switching a large current in an inductor instantaneously is a tricky issue. More details on the methods used are given in the article *Gradient echo memory in an ultra-high optical depth cold atomic ensemble* attached to this work [37].

Finally, an important reason why GEM is a powerful tool for storing and retrieving light is that it is intrinsically temporally multimode: one can store multiple pulses at different times inside the memory and retrieve them independently [44, 36, 45]. But it is also spatially multimode, so images can be stored in the transverse plane (only limited by decoherence due to atomic diffusion). We have leveraged these two advantages to demonstrate the first storage of a "movie" inside an atomic memory [36]. Results are presented in the next pages.

2.1.4 Press releases

These results led to multiple press articles covering this topic. I reproduce here some excerpts.

The sequence of images that constitute Hollywood movies can be stored handily on solid-state media such as magnetic tape or compact diskettes. At the Joint Quantum Institute images can be stored in something as insubstantial as a gas of rubidium atoms. No one expects a vapor to compete with a solid in terms of density of storage. But when the "images" being stored are part of a quantum movie –the coherent sequential input to or output from a quantum computer – then the pinpoint control possible with vapor will be essential. **Phys.org**

One of the enabling technologies for a quantum internet is the ability to store and retrieve quantum information in a reliable and repeatable way. One of the more promising ways to do this involves photons and clouds of rubidium gas. Rubidium atoms have an interesting property in that a magnetic field causes their electronic energy levels to split, creating a multitude of new levels. **MIT Technology Review**

Having stored one image (the letter N), the JQI physicists then stored a second image, the letter T, before reading both letters back in quick succession. The two "frames" of this movie, about a microsecond apart, were played back successfully every time, although typically only about 8 percent of the original light was redeemed, a percentage that will improve with practice. According to Paul Lett, one of the great challenges in storing images this way is to keep the atoms embodying the image from diffusing away. The longer the storage time (measured so far to be about 20 microseconds) the more diffusion occurs. The result is a fuzzy image. **Science Daily.**

Temporally multiplexed storage of images in a gradient echo memory

Quentin Glorieux,* Jeremy B. Clark, Alberto M. Marino, Zhifan Zhou, and Paul D. Lett

Quantum Measurement Division, National Institute of Standards and Technology and Joint Quantum Institute, NIST, and the University of Maryland, Gaithersburg, MD 20899, USA

**quentin.glorieux@nist.gov*

Abstract: We study the storage and retrieval of images in a hot atomic vapor using the gradient echo memory protocol. We demonstrate that this technique allows for the storage of multiple spatial modes. We study both spatial and temporal multiplexing by storing a sequence of two different images in the atomic vapor. The effect of atomic diffusion on the spatial resolution is discussed and characterized experimentally. For short storage time a normalized spatial cross-correlation between a retrieved image and its input of 88 % is reported.

© 2012 Optical Society of America

OCIS codes: (270.0270) Quantum optics; (270.5565) Quantum communications; (210.4680) Optical memories.

References and links

1. H. J. Kimble, "The quantum internet," Nature **453**, 1023–1030 (2008).
2. N. Sangouard, C. Simon, H. de Riedmatten, and N. Gisin, "Quantum repeaters based on atomic ensembles and linear optics," Rev. Mod. Phys. **83**, 33–80 (2011).
3. N. Sangouard, C. Simon, B. Zhao, Y.-A. Chen, H. de Riedmatten, J.-W. Pan, and N. Gisin, "Robust and efficient quantum repeaters with atomic ensembles and linear optics," Phys. Rev. A **77**, 062301 (2008).
4. C. Simon, M. Afzelius, J. Appel, A. Boyer de la Giroday, S. J. Dewhurst, N. Gisin, C. Y. Hu, F. Jelezko, S. Kroll, J. H. Mller, J. Nunn, E. S. Polzik, J. G. Rarity, H. de Riedmatten, W. Rosenfeld, A. J. Shields, N. Skold, R. M. Stevenson, R. Thew, I. A. Walmsley, M. C. Weber, H. Weinfurter, J. Wrachtrup, and R. J. Young, "Quantum memories," Eur. Phys. J. D **58**, 1–22 (2010).
5. A. Lvovsky, B. Sanders, and W. Tittel, "Optical quantum memory," Nat. Photonics **3**, 706–714 (2009).
6. W. J. Munro, K. A. Harrison, A. M. Stephens, S. J. Devitt, and K. Nemoto, "From quantum multiplexing to high-performance quantum networking," Nat. Photonics **4**, 792–796 (2010).
7. C. Simon, H. de Riedmatten, and M. Afzelius, "Temporally multiplexed quantum repeaters with atomic gases," Phys. Rev. A **82**, 010304 (2010).
8. M. Afzelius, C. Simon, H. de Riedmatten, and N. Gisin, "Multimode quantum memory based on atomic frequency combs," Phys. Rev. A **79**, 052329 (2009).
9. M. Bonarota, and J. Le Gouët, "Highly multimode storage in a crystal," New. J. Phys. **13**, 013013 (2011).
10. S. Y. Lan, A. G. Radnaev, O. A. Collins, D. N. Matsukevich, T. A. B. Kennedy, and A. Kuzmich, "A multiplexed quantum memory," Opt. Express **17**, 13639–13645 (2009).
11. O. Collins, S. Jenkins, A. Kuzmich, and T. Kennedy, "Multiplexed memory-insensitive quantum repeaters," Phys. Rev. Lett. **98**, 060502 (2007).
12. M. Hosseini, B. M. Sparkes, G. Hetet, J. J. Longdell, P. K. Lam, and B. C. Buchler, "Coherent optical pulse sequencer for quantum applications," Nature **461**, 241–245 (2009).
13. K. Surmacz, J. Nunn, K. Reim, K. C. Lee, V. O. Lorenz, B. Sussman, I. A. Walmsley, and D. Jaksch, "Efficient spatially resolved multimode quantum memory," Phys. Rev. A **78**, 033806 (2008).
14. M. Shuker, O. Firstenberg, R. Pugatch, A. Ron, and N. Davidson, "Storing images in warm atomic vapor," Phys. Rev. Lett. **100**, 223601 (2008).
15. K. Vudyasetu, R. M. Camacho, and J. C. Howell, "Storage and retrieval of multimode transverse images in hot atomic rubidium vapor," Phys. Rev. Lett. **100**, 123903 (2008).

#164994 - $15.00 USD Received 19 Mar 2012; revised 27 Apr 2012; accepted 1 May 2012; published 16 May 2012
(C) 2012 OSA

16. I. H. Agha, C. Giarmatzi, Q. Glorieux, T. Coudreau, P. Grangier, and G. Messin, "Time-resolved detection of relative-intensity squeezed nanosecond pulses in an ^{87}Rb vapor," New J. Phys. **13**, 043030 (2011).
17. V. Boyer, A. M. Marino, R. C. Pooser, and P. D. Lett, "Production of entangled images by four-wave mixing," Science **321**, 544–547 (2008).
18. G. Hétet, M. Hosseini, B. Sparkes, and D. Oblak, P. K. Lam, and B. C. Buchler, "Photon echoes generated by reversing magnetic field gradients in a rubidium vapor," Opt. Lett. **33**, 2323–2325 (2008).
19. M. Hosseini, B. M. Sparkes, G. Campbell, P. K. Lam, and B. C. Buchler, "High efficiency coherent optical memory with warm rubidium vapour," Nat. Commun. **2**, 174 (2011).
20. M. Hosseini, G. Campbell, B. M. Sparkes, P. K. Lam, and B. C. Buchler, "Unconditional room-temperature quantum memory," Nat. Phys. **7**, 794–798 (2011).
21. H. Sasaki, K. Karaki, M. Mitsunaga, and N. Uesugi, "Holographic motion picture: theory and observations," J. Lumin. **64**, 273–281 (1995).
22. M. Mitsunaga, N. Uesugi, H. Sasaki, and K. Karaki, "Holographic motion picture by Eu3+:Y2SiO5," Opt. Lett. **19**, 752–754 (1994).
23. O. Firstenberg, M. Shuker, R. Pugatch, D. Fredkin, N. Davidson, and A. Ron, "Theory of thermal motion in electromagnetically induced transparency: Effects of diffusion, Doppler broadening, and Dicke and Ramsey narrowing," Phys. Rev. A **77**, 043830 (2008).
24. C. Cohen-Tannoudji, J. Dupont-Roc, and G. Grynberg, *Atom Photon Interactions: Basic Process and Applications* (Wiley Science, 2008).
25. F. Franz, "Rubidium spin relaxation in the rare gases under ultraclean conditions," Phys. Rev. **139**, A603–A611 (1965).
26. W. Franzen, "Spin relaxation of optically aligned rubidium vapor," Phys. Rev. **115**, 850–856 (1959).
27. M. Lukin, "Colloquium: Trapping and manipulating photon states in atomic ensembles," Rev. Mod. Phys. **75**, 457–472 (2003).
28. M. Fleischhauer and M. Lukin, "Quantum memory for photons: dark-state polaritons," Phys. Rev. A **65**, 022314 (2002).
29. L. Zhao, T. Wang, Y. Xiao, and S. F. Yelin, "Image storage in hot vapors," Phys. Rev. A **77**, 041802 (2008).

1. Introduction

Storage and retrieval of non-classical states of light has recently become a topic of interest due to the need for quantum memories (QM) in quantum network protocols [1]. Indeed, a QM is required for quantum repeaters which allow long distance distribution of entanglement [2,3]. In the perfect case, a QM should preserve the quantum state of a light pulse during the longest storage time possible. A large number of techniques have been investigated (see [4,5] and references therein). An attractive way to improve the performance of a QM is by multiplexing communication channels [6,7]. Temporal multiplexing can be used to increase the rate of entanglement distribution [8,9]. Similarly, a spatially multimode approach can, in principle, reduce the requirements on the storage time for a realistic implementation of a quantum repeater [10,11]. Experimentally, temporal and spatial multiplexing have been demonstrated independently with different techniques in atomic memories. Temporal multiplexing, in an atomic medium, has been recently demonstrated using the gradient echo memory (GEM) technique [12]. Correspondingly, using the electromagnetically induced transparency (EIT) technique, several groups have stored an image in an atomic vapor [13–15]. In this paper, we first demonstrate the ability of the GEM in an atomic vapor to store multi-spatial-mode images and we show that the resolution of the retrieved images is ultimately limited by the atomic diffusion of the atoms.

Given that there exists a straightforward method for the generation of multi-spatial-mode quantum states of light near the Rb atomic resonance [16,17], we would like to eventually be able to store such states in an atomic vapor memory. While a large number of other approaches to a quantum memory are available, our experiment is implemented using the promising technique of gradient echo memory in an atomic vapor introduced by Buchler and coworkers [18]. This technique has recently led to a recovery efficiency of 87 % [19], temporal multiplexing [12], and storage of a weak coherent state with a recovery fidelity above the no-cloning limit [20]. Thus, the GEM is a promising candidate for quantum memory because it has a very high recovery efficiency not achieved yet with other techniques in a hot atomic vapor. It is also

#164994 - $15.00 USD Received 19 Mar 2012; revised 27 Apr 2012; accepted 1 May 2012; published 16 May 2012
(C) 2012 OSA

relatively easy to implement, not requiring laser-cooled atoms or cryogenics. The ability of the GEM to store and recover multi-spatial-mode images, and to do so with high spatial fidelity has, however, not yet been demonstrated, and the present experiments are designed to verify the image storage properties of the GEM in much the same way as has been done for other techniques.

It is also interesting to combine multiplexing techniques for both time and space. So far storing multiple images has been demonstrated only in solid-state systems. Several experiments using holographic memories have been able to record trains of images by storing the information in the atomic population [21,22] and have opened the way to photon-echo protocols. Here, we report the coherent storage and retrieval of a sequence of two different images using an atomic vapor gradient echo memory.

2. Gradient echo memory

In our GEM experiments a light pulse is sent into a ^{85}Rb atomic vapor which can be considered, for simplicity, as a collection of three-level systems in a Λ configuration. A spatially-dependent Zeeman shift is applied using a linearly varying magnetic field along the axis of propagation. For a total Zeeman shift larger than the pulse frequency bandwidth, a high optical density, and the presence of an intense co-propagating control field that drives the Raman transition, each frequency component of the pulse can be absorbed. The photonic excitation is therefore transferred into the long lived collective coherence of the hyperfine atomic ground states. Similar to nuclear magnetic resonance or photon echo techniques, the spectral components of the signal are mapped into the medium along the length of the cell. After the excitation, the collective dipole dephases due to the inhomogenous magnetic field. It is possible, however, to rephase the collective excitation by reversing the magnetic field gradient. The time evolution is then reversed, and when all the dipoles have rephased the retrieved light pulse emerges in the forward direction provided that the control field is again present. As demonstrated in [19], this technique preserves a phase relationship between the input and retrieved pulses and is therefore a coherent storage.

In our experiment, the transverse profile of the signal field is shaped using a mask and imaged into the atomic medium. For a control field much wider than the signal, the transverse profile of the collective excitation of the atomic coherence directly mimics the profile of the signal field, so spatial information can be stored in the atomic memory. In this paper we first describe the experimental setup and present results on the storage of two images into the atomic medium. We then introduce the criterion of similarity, based on a normalized cross–correlation, to analyze the spatial fidelity of the retrieved images with respect to its input reference image. The crosstalk between the first and second retrieved images is investigated with regard to this criteria. Finally, we use a resolution chart to measure and quantify the effect of atomic diffusion at a given buffer gas partial pressure on the storage of spatial information. We investigate primarily the transverse spatial diffusion, as longitudinal diffusion along the direction of the field gradient effectively prevents atoms from contributing to the coherent echo signal, and we show that the resolution of the retrieved images primarily depend on the storage duration, as expected and similar to what is found with EIT techniques.

3. Experimental setup

The experimental setup is shown in Fig. 1. The light from a Ti:sapphire laser, blue detuned by 1.5 GHz from the $5S_{1/2}$, F=2 $\rightarrow$ $5P_{1/2}$, F=3 transition, is used as a control field for the Raman coupling. The signal beam is generated using a double-passed 1.5 GHz acousto-optic modulator to downshift the frequency by the amount of the hyperfine splitting (3.036 GHz). The signal and control beams are overlapped with crossed linear polarizations in the 5 cm long

#164994 - $15.00 USD Received 19 Mar 2012; revised 27 Apr 2012; accepted 1 May 2012; published 16 May 2012
(C) 2012 OSA

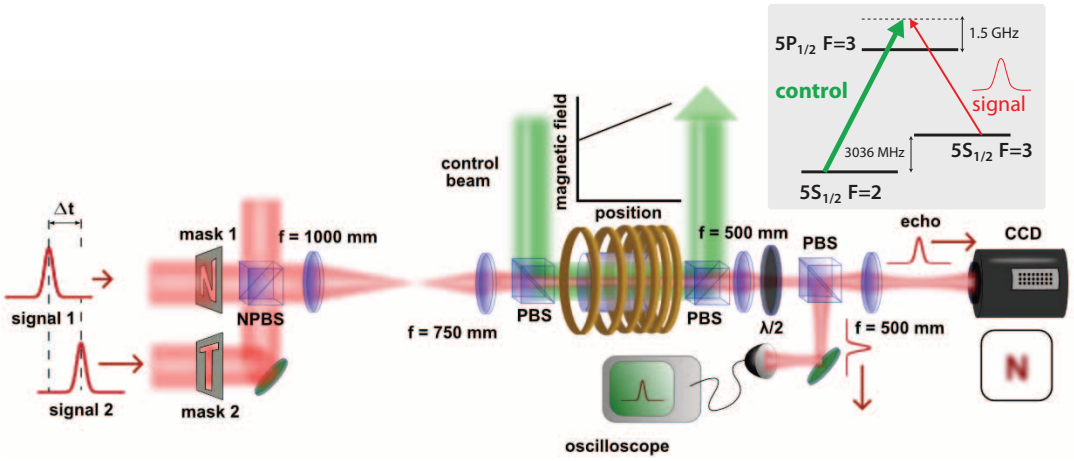

Fig. 1. Schematic of the experimental setup for image storage in a GEM. The signal beam is previously shaped temporally with an acousto-optic-modulator (not shown). The spatial profile is fixed using a mask in the beam path and the mask is then imaged into the ^{85}Rb cell with a magnification of 0.75. A control field is overlapped with the signal using a polarizing beam splitter (PBS), and finally, the retrieved image is recorded using a fast–gated intensified camera. A small fraction of the signal is sent to a fast photodiode for monitoring the spatially-integrated retrieved power. For the storage of two consecutive images, two signal beams are combined with the same polarization on a non-polarizing beam splitter. Inset: three-level system for ^{85}Rb.

memory cell. The cell contains isotopically pure ^{85}Rb and 667 Pa (5 Torr) of Ne buffer gas and is heated up to 80 °C. A bias magnetic field of 1 mT (10 G) is applied to the cell to split the ground state Zeeman sublevels and select a specific three-level system (see Fig. 1 inset). The Raman absorption line is broadened by a 15 μT/cm magnetic field gradient we apply in the propagation direction. The spatial profile of the signal beam is shaped by placing a mask in its path and imaging it into the memory cell. In order to store two different images, two distinct signal beams have to be shaped independently. The temporal profile of each signal pulse is Gaussian with a full width at $1/e^2$ of 1.1 μs. The storage duration is set by the delay between the input pulse and the flip of the magnetic gradient. The flip duration is less than 1 μs. After the cell, the control field is filtered with a polarizing beam splitter. A fast–gated intensified camera records the time–integrated light intensity during 100 ns wide frames. For convenience, a small fraction of the retrieved image beam is sent to a photodiode for recording the retrieved power as function of time.

4. Temporal and spatial multiplexing

In Fig. 2(a) we present the timeline of the storage and retrieval of two consecutive images. The amplitude of the retrieved pulse is normalized to the input amplitude. In this particular configuration (control beam diameter of 3 mm and power 120 mW, and a probe beam diameter of 1 mm) we report a retrieval efficiency of 8 %. Improvements to this can be obtained by using a longer memory cell, thereby improving the optical depth for the Raman absorption. The optical depth on resonance is approximatively 200, nevertheless, the probe beam is far detuned from resonance, and the absorption is due to a 2-photon Raman absorption. In the results presented here, the absorption of the input beam is on the order of 30 %, leading to a maximum theoretical retrieval efficiency of 9 %. (We have measured a recovery efficiency of

#164994 - $15.00 USD Received 19 Mar 2012; revised 27 Apr 2012; accepted 1 May 2012; published 16 May 2012
(C) 2012 OSA

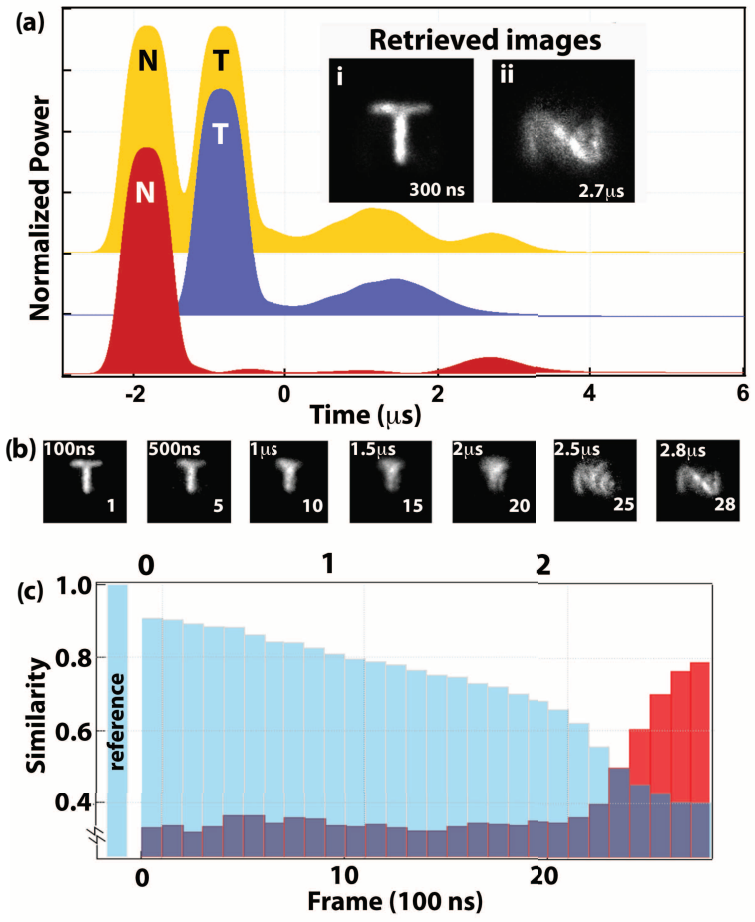

Fig. 2. Storage and retrieval of two images in a GEM. (a) The spatially-integrated intensity from the retrieval of the single letter T (blue) and N (red). The input pulse is at negative time and the retrieved pulse is at the symmetric positive time after the magnetic field gradient flip. The yellow curve shows the storage of two images, and the curves are vertically displaced for clarity. Retrieved images at time 0.3 μs and 2.7 μs are presented, respectively, in Fig. 2(a), i and ii. (b) The detailed timeline of the retrieved images for 7 frames. The frame number is indicated in the images and the time corresponds to the time after the magnetic flip. (c) S_N (red) and S_T (blue) as function of the frame number. The reference for N or T has a similarity of 1 and is plotted before 0.

#164994 - $15.00 USD Received 19 Mar 2012; revised 27 Apr 2012; accepted 1 May 2012; published 16 May 2012
(C) 2012 OSA

up to 62 % for a 6.5 ms storage time in a similar configuration by using a 20 cm long memory cell.) As we are interested in the spatial properties of the GEM in this work we do not focus on the overall efficiency of the process. We first check that a single image can be stored, and optimize the alignment independently for the two different signal beams corresponding to the images of the letters N and T (the red and blue traces in Fig. 2(a), respectively). To store both images in the atomic memory, the two input pulses are combined on a beam splitter with a delay of 1 μs between them. Two frames from the gated intensified camera of the retrieved images after a storage time of 0.5 μs (frame 3) and 4.5 μs (frame 27) are presented, respectively, in Fig. 2(a), i and ii. As GEM in this configuration is a first-in-last-out memory [12], the first retrieved image corresponds to the letter T and the second one to the letter N.

A more detailed timeline of 7 frames for the retrieved images is included in Fig. 2(b). This figure shows the intensity profile of the retrieved light for different times and clearly exhibits an overlap between the two letters in frame 25. To study the overlap quantitatively we define the similarity S to be the cross–correlation of a given frame with a reference image, normalized by the square root of the auto–correlation product :

$$S = \frac{\sum_{i,j} N_{ij}^{in} N_{ij}^{echo}}{\sqrt{\sum_{i,j} (N_{ij}^{in})^2 \sum_{i,j} (N_{ij}^{echo})^2}}, \tag{1}$$

where $N_{i,j}^{in}$ is the intensity recorded for pixel i,j of the input pulse image and $N_{i,j}^{echo}$ for the retrieved image. The reference image is selected from among the frames of the input pulse for each letter. In Fig. 2(c) we plot the similarities for the retrieved images with respect to the N and the T reference images (respectively denoted S_N and S_T). For reference, the similarity between the T and the N input images is 35 %. The evolution as function of time is given for 28 non-overlapping frames representing successive 100 ns time intervals. The first frame is taken 100 ns after the magnetic field gradient is switched. We temporally expand the retrieved pulse compared to the input (expansion ratio of 1.4) using a different magnetic field gradient for the recovery [12]. This allowed for a slightly longer diffusion time and made it easier to measure its effect in the retrieved images. The total storage time is therefore given by twice the time measured from the magnetic field flip corrected by the expansion ratio. For the retrieved image the initial value of S_T is 88 % and it decreases at a rate of 1.1 % per frame due to the atomic diffusion that blurs the image. After 19 frames the value of S_T starts to drop faster, at a rate of 4.6 % per frame. On the other hand, S_N is initially low (35 %) and after 21 frames it suddenly rises at a rate of 8.5 % per frame. After frame 28 S_N reaches 78 %, corresponding to when the second echo is retrieved from the memory. The two curves cross during the 24th frame with S_T = 47 % and S_N = 51 %. This is close to a value of 50 %, which we take to be a threshold for distinguishing the images. As shown by the yellow curve of Fig. 2(a), there is a temporal overlap between the two input images. The similarities corresponding to this overlapping input frame are S_T = 55 % and S_N = 48 %. On the other hand, the frame just before can be identified as an N and the frame just after as a T, with a difference $D = |S_N - S_T| > 0.5$. The retrieved images mimic this behavior with an overlap during frame 24. The value of D immediately before (frame 23) and after (frame 25) is greater than 0.15. These similar qualitative behaviors suggest that there is no significant crosstalk between the two images and that the reduction of D between the input and the output is a consequence of the blurring of the images.

5. Effect of atomic diffusion

It has been proposed that the decay of S during the storage in an EIT based memory is mainly due to atomic diffusion [14,23]. We show that our experiment using a GEM technique is consistent with this statement and demonstrate that the expected spatial resolution of the retrieved

#164994 - $15.00 USD Received 19 Mar 2012; revised 27 Apr 2012; accepted 1 May 2012; published 16 May 2012
(C) 2012 OSA

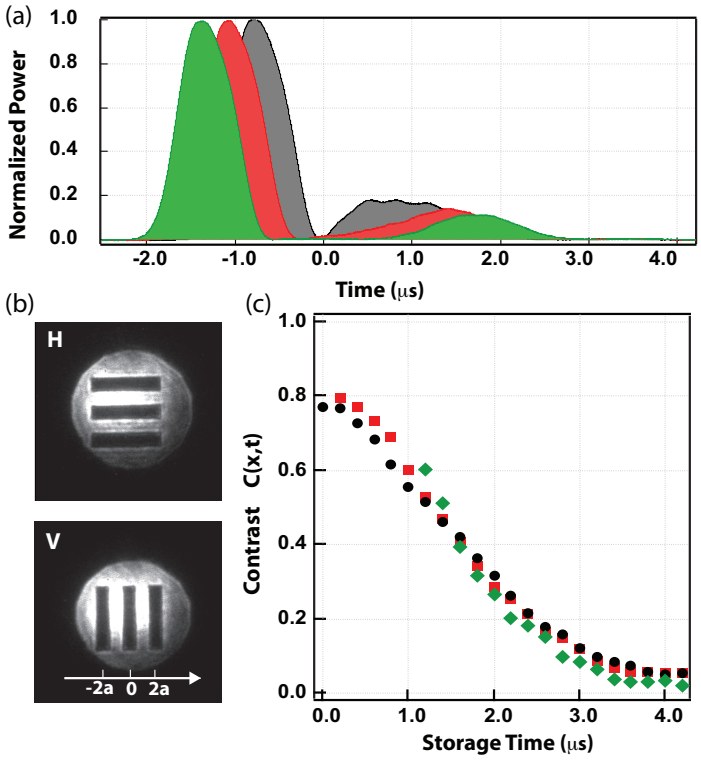

Fig. 3. (a) The input and retrieved pulses for three different delays. Time t = 0 is taken to be the time of the magnetic field flip. The maximum of the input pulses are at -1.4 μs, -1.1 μs, -0.8 μs (respectively green, red, and black curves). (b) The input images for horizontal (H) and vertical (V) lines. $1/2a$ is the spatial frequency of the bars, where the distance between a black and a white line is denoted a. (c) Contrast for the retrieved image (vertical) as function of storage time for 21 frames. The symbol colors correspond to those in a).

images can be predicted from the buffer gas partial pressure and the storage time. The internal dynamics of the atoms are described by the optical Bloch equations [24]. In the presence of a buffer gas, the Rb atoms are subject to velocity changing collisions with the gas that are assumed to preserve the internal state. The atomic excitation $\rho(x,y,z,t)$ therefore diffuses in the transverse directions as follows:

$$\frac{\partial}{\partial t}\rho(x,y,z,t) = D\nabla^2\rho(x,y,z,t), \tag{2}$$

where D is the diffusion coefficient. The diffusion along the propagation axis is neglected as it induces only loss in the process and does not affect the spatial information in the transverse plane. Indeed, if one atom diffuses along the direction of the magnetic gradient, it will not rephase at the same time as others and therefore will not contribute to the expected retrieved image. Using the Green's function formalism, the evolution in time and space of a single point initially at the position $X' = (x',y')$ can be calculated. Thus the evolution of the atomic excitation from an arbitrary initial condition can be derived by knowing the spatial distribution $\rho(x',y',0)$ of the excitation at t = 0 as follows:

$$\rho(x,y,t) = \frac{1}{\sqrt{4\pi Dt}}\int e^{\frac{-(x-x')^2-(y-y')^2}{4Dt}}\rho(x',y',0)\,dx'\,dy'. \tag{3}$$

#164994 - $15.00 USD Received 19 Mar 2012; revised 27 Apr 2012; accepted 1 May 2012; published 16 May 2012
(C) 2012 OSA

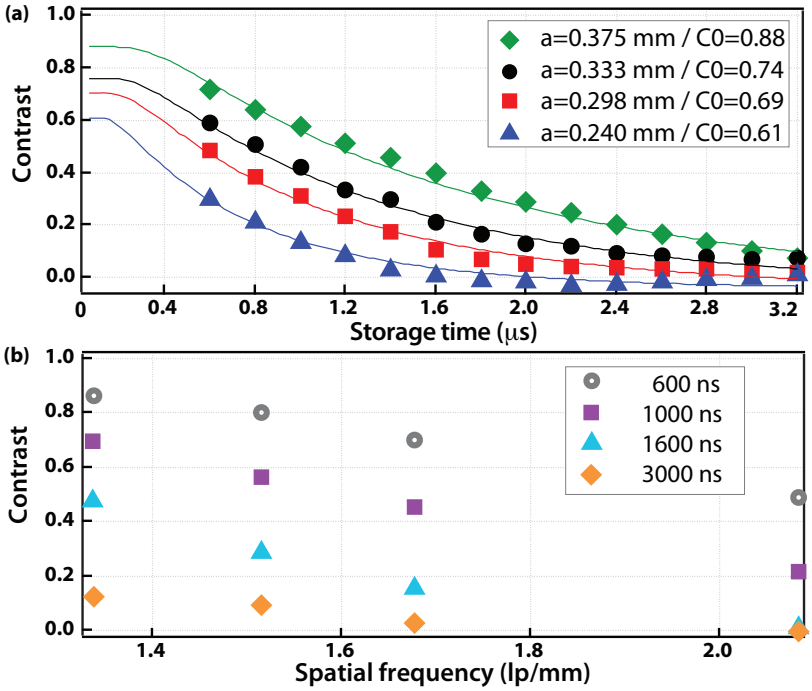

Fig. 4. (a) Contrast and theoretical fit for four images such as shown in Fig. 3(b), with bar widths, a, as indicated in the figure. The fits are done without free parameters using Eq (3). D = 105 cm^2/s, $t_0 = 0$ and C_0 is given in the legend. (b) Modulation transfer function for four different storage times.

To evaluate quantitatively the effect of diffusion on the spatial resolution we stored and retrieved images of a resolution test chart consisting of a group of three bars oriented vertically or horizontally as shown in Fig. 3(b). The resolution chart is imaged into the memory with a magnification of 0.75. For three different pulse delays relative to the magnetic field switching time (Fig. 3(a)) we record 100 ns frames during the retrieval process. The contrast $C(t)$ is defined as:

$$C(t) = \frac{I(x=a,t) - I(x=0,t)}{I(x=a,t) + I(x=0,t)}, \tag{4}$$

where x can refer to the vertical or the horizontal direction and a is the width of a stored line taking into account the magnification (see Fig. 3(b)). At $t = 0$, $x = 0$ refers to the center dark line and $x = a$ to the center of a bright line. $I(x,t)$ is the intensity recorded by the camera at position x for a frame recorded at time t, integrated over the extent of the pattern in y. With this definition C can fall below zero for a long storage time as the atoms diffuse from bright lines to dark lines resulting in $I(x = 0) > I(x = a)$. As shown in Fig. 3(c), the contrast for a given spatial frequency does not depend on the time between the input pulse maximum and the magnetic field switching, but only on the total storage time. We have also independently checked that the orientation of the lines does not affect the contrast. The fact that the only parameter that affects the contrast is the storage duration strongly suggests that diffusion is the main source of the degradation of the resolution.

To confirm this observation we have compared 4 masks with different spatial frequencies. The resolution of the mask varies from of 1 to 1.6 line pairs/mm, resulting in lines of 375 μm to 240 μm in the image plane in the memory after taking into account the magnification. In Fig. 4(a), we plot the contrast as function of storage time for the different masks and the fit

#164994 - $15.00 USD Received 19 Mar 2012; revised 27 Apr 2012; accepted 1 May 2012; published 16 May 2012
(C) 2012 OSA

of the data to the model of Eq. (3). In order to take into account independently the quality of our optical system and the contrast degradation due to the memory we have measured the initial contrast of the input pulse C_0. C_0 is measured for the different masks and is a fixed normalization parameter for the fit. We take the value of the diffusion coefficient for 667 Pa of Ne buffer gas at 80 °C to be 105 cm^2/s as previously reported [25,26], and therefore no free parameters are allowed for the fit. The good agreement between our theoretical model based on atomic diffusion and the experimental data confirms the key role of diffusion in the contrast of the retrieved image for the GEM technique. In Fig. 4(b) we plot the modulation transfer function (contrast as a function of spatial frequency) for different storage times. This graph could be a useful benchmark for spatial channel multiplexing for a quantum communication network, as the three lines of the test chart can be seen as three parallel information channels. Since the contrast needed for a given multi-spatial-mode quantum repeater protocol can be defined a priori, Fig. 4(b) provides the maximum spatial frequency allowed for a fixed storage time and therefore the number of spatial channels which can be simultaneously used to store quantum information.

6. Conclusion

We have shown that a multi-spatial-mode image can be stored using the GEM protocol. Moreover, we have demonstrated that multiple images can be stored and retrieved at different times, allowing the storage of a short movie in an atomic memory. This opens the way to multiplexing simultaneously in time and in space for future quantum memory applications. We confirm that the main limitation of this technique, similar to that in EIT-based memory [14,23], is the atomic diffusion during the storage time. We expect that this could be overcome by using a cold atomic sample [27,28] or mitigated by storing the Fourier transform of the image into the memory as suggested in [14,29]. Finally, as the different spectral components of the input signal are mapped along the length of the cell with GEM, unlike EIT, it would be interesting to investigate if there is an effect of longitudinal diffusion on the signal spectral properties and noise.

Acknowledgments

This work was supported by the AFOSR. Q.G. and P.D.L. thank Ping Koy Lam and Ben Buchler of the Quantum Optics Group at ANU for hosting a visit by Q.G. Q.G. thanks all the members of this group for fruitful discussions.

#164994 - $15.00 USD Received 19 Mar 2012; revised 27 Apr 2012; accepted 1 May 2012; published 16 May 2012
(C) 2012 OSA

2.2 GEM in a cold atom ensemble

Shifting from warm atomic vapor (with the simplicity of high and tunable density) to laser-cooled atoms trapped in a magneto-optical trap (MOT) has many advantages. The first of them being the reduction of decoherence due to atomic motion. However, in order to obtain the large optical depth required for an efficient gradient echo memory, a substantial optimization work has been needed. In the paper attached to this work, I highlight the various techniques I developed and used during my stay at the Australian National University under the supervision of Ping Koy Lam.

For quantum memory applications we aim to reach low temperatures and the very large optical depths (OD) required for high efficiency. Because OD is related to the integrated absorption of photons through a sample, there are a number of ways to increase the OD. These include: increase the atom number (for instance by increasing the length of the cloud) or increase the density. Low temperature is also important as the thermal diffusion of atoms is a limiting factor for the memory lifetime.

In the attached paper, I present a MOT that achieves a peak OD of over 1000 at a temperature of 200 μK. We obtain this result by combining three techniques:

- The optimization of the static loading of the MOT through geometry. The optimal shape for our atomic ensemble is a cylinder along the direction of the memory beams to allow for maximum absorption of the probe. This can be achieved by using rectangular, rather than circular, quadrupole coils or using a 2D MOT configuration.
- The use of a spatial dark spot. The density in the trapped atomic state is limited by re-absorption of fluorescence photons within the MOT (leading to an effective outwards radiation pressure). By placing a dark spot of approximately 7.5 mm in diameter in the repump, atoms at the centre of the MOT are quickly pumped into the lower ground state and become immune to this unwanted effect, allowing for a higher density of atoms in the centre of the trap, as first demonstrated in [46].
- The use of optical de-pumping, followed by a compression phase with a temporal dark spot [47].

With the setup built using these techniques, we have implemented the gradient echo memory scheme on the D1 line of Rubidium. The results shown here demonstrate a memory efficiency of $80 \pm 2\%$ and a coherence time up to 195 μs. This coherence time is a factor of eight greater than GEM experiments done in atomic vapor (described in the previous section).

New Journal of Physics
The open access journal for physics

Gradient echo memory in an ultra-high optical depth cold atomic ensemble

B M Sparkes[1], J Bernu[1], M Hosseini[1], J Geng[1,2], Q Glorieux[1,3], P A Altin[4], P K Lam[1,5], N P Robins[4] and B C Buchler[1]

[1] Centre for Quantum Computation and Communication Technology, Department of Quantum Science, Research School of Physics and Engineering, The Australian National University, Canberra, ACT 0200, Australia
[2] Quantum Institute for Light and Atoms, Department of Physics, East China Normal University, Shanghai 200062, People's Republic of China
[3] Joint Quantum Institute, University of Maryland, College Park, MD 20742, USA
[4] Quantum Sensors Lab, Department of Quantum Science, Australian National University, Canberra, ACT 0200, Australia
E-mail: ping.lam@anu.edu.au

New Journal of Physics **15** (2013) 085027 (15pp)
Received 14 February 2013
Published 23 August 2013
Online at http://www.njp.org/
doi:10.1088/1367-2630/15/8/085027

Abstract. Quantum memories are an integral component of quantum repeaters—devices that will allow the extension of quantum key distribution to communication ranges beyond that permissible by passive transmission. A quantum memory for this application needs to be highly efficient and have coherence times approaching a millisecond. Here we report on work towards this goal, with the development of a ^{87}Rb magneto-optical trap with a peak optical depth of 1000 for the D2 $F = 2 \rightarrow F' = 3$ transition using spatial and temporal dark spots. With this purpose-built cold atomic ensemble we implemented the gradient echo memory (GEM) scheme on the D1 line. Our data shows a memory efficiency of $80 \pm 2\%$ and coherence times up to 195 μs, which is a factor of four greater than previous GEM experiments implemented in warm vapour cells.

[5] Author to whom any correspondence should be addressed.

Content from this work may be used under the terms of the Creative Commons Attribution 3.0 licence. Any further distribution of this work must maintain attribution to the author(s) and the title of the work, journal citation and DOI.

© IOP Publishing Ltd and Deutsche Physikalische Gesellschaft

Contents

1. Introduction

The development of quantum key distribution (QKD) over the last few decades [1] brings with it the promise of secure global communication. Although there have been some heroic efforts, the current maximum distance for QKD is 260 km [2], achieved using optical fibres. Beyond this length scale, the loss of photons from the quantum channel makes provably secure single-step QKD impossible. One way of overcoming the distance limitation is to use a quantum repeater (QR), a device based on entanglement swapping along nodes placed between the start and end locations of the signal [3]. A working QR will require two key components: a source of entanglement and a quantum memory to store the entanglement at the nodes [4, 5]. Storage is required because the generation, detection and distillation of entanglement is not deterministic. In order to establish entanglement between repeater nodes, entanglement has to be stored and recalled on demand.

For use in a QR, a quantum memory must meet a number of requirements. The efficiency of the memory must be as high as possible, ideally approaching unity. The efficiency is important for bit rates: inefficient storage means that the chance of generating entanglement in any given attempt is lower and it will take longer to complete a swapping operation. The storage time must be long as this will limit the maximum distance between nodes in a QR network. For instance, if the distance between nodes were to be 100 km, then more than half a millisecond of storage is required. A high storage bandwidth is also desirable. The bandwidth will limit the kind of entanglement that can be stored in the memory. The most common sources of entangled photons are based on spontaneous parametric downconversion and these sources have a wide bandwidth. A narrow bandwidth memory will therefore require new sources of entanglement [6–8]. A multimode quantum memory, in which many entangled states can be stored simultaneously, would allow for faster bit-rates in QRs, and there are QR protocols that can use multi-mode memories to improve QR designs [9, 10]. The product of the storage time and the bandwidth, known as the delay-bandwidth product gives an indication of the number of pieces of information that can usefully be stored in a multimode memory.

The challenge for experimentalists developing quantum memory prototypes is to realize all these properties in a single system. The practicalities of achieving this are intertwined with

the choice of atomic ensemble. The current menu has a choice of three: warm gaseous atomic ensembles [11–13]; solid state systems [14–17]; and cold gaseous atomic ensembles, which will be the focus of this work.

No matter what the storage medium, the key to achieving high efficiencies is to have a high optical depth (OD). This is normally achieved by having as high a density of absorbers in the interaction volume as possible. To date the highest efficiency of any unconditioned quantum memory prototype is 87% [11]. This was achieved using the gradient echo memory (GEM) scheme in a warm atomic vapour. This system used a 20 cm-long cell of isotopically pure ^{87}Rb and 0.07 kPa of Kr buffer gas and had a resonant OD in the thousands [18]. The thermal motion of the atoms is the primary obstacle to increasing the storage lifetime in warm vapour [18, 19], which was found to decay with a time constant of around 50 μs.

Reducing atomic motion is not the only way to increase storage times—it depends on the storage protocol. For example, it has been demonstrated that long storage times can be obtained in an electromagnetically induced transparency (EIT)-based warm memory by using high buffer gas pressure [20]. In a GEM scheme, however, high buffer gas pressure increases collisional broadening and absorption of the coupling beam [18]. The effect of transverse diffusion can be minimized by increasing the interaction volume and using anti-relaxation coatings to minimize inelastic wall collisions [21, 22]. Although this technique would reduce transverse diffusion, the longitudinal diffusion would eventually limit coherence times. This is because, owing to the longitudinal frequency gradient needed for GEM, longitudinal diffusion introduces random frequency changes to the atoms during storage, which lowers the memory fidelity.

One obvious way to overcome the impact of atomic motion is to use slow-moving atoms. Laser cooling provides an efficient way to achieve this, and cold atom memories have been the subject of many experiments aiming for longer memory storage times. The majority of these cold atom experiments have used EIT as the storage method. A coherence time of 540 ms was achieved by cooling approximately 3×10^6 Na atoms into a Bose–Einstein condensate (BEC) and placing them in a dipole trap [23]. The maximum memory efficiency in this ensemble was, however, just a few per cent. A much longer coherence time of 3 s was achieved using a cross-beam dipole trap of 3×10^5 ^{87}Rb atoms [24], although no memory was demonstrated in this experiment. This was recently improved on further, with a coherence time of 16 s [25].

By optimizing for higher atom number and therefore higher OD, high efficiency is also possible in cold atom systems, although this can come at the expense of long storage time due to higher temperatures. A memory efficiency of 50% was achieved using a two-dimensional (2D) magneto-optical trap (MOT) of ^{85}Rb with an OD < 140, and a coherence time of a few hundred nanoseconds [26]. Similar efficiencies were achieved for single-photon storage in a ^{87}Rb BEC in a cross-beam dipole trap containing 1.2×10^6 atoms [27]. The coherence time for this experiment was approximately 500 μs. More recently, 78% efficiency and a coherence time of 98 μs [28] has been achieved using a MOT with 10^9 atoms and an OD of 160. It has also been demonstrated that, by creating a MOT inside a ring cavity, single photons can be generated efficiently with the atomic coherence being maintained for up to 3 ms [29]. Finally, experiments have also been done showing the interaction of quantum states of light with cold-atom-based EIT. Continuous-wave sideband squeezing [30] and discrete variable entanglement [7] have both been investigated.

In this paper we introduce a cold atom realization of the GEM scheme. This protocol has resulted in the highest efficiencies in both warm vapour [11] and solid-state memory

systems [15]. In both these realizations, it was shown that GEM adds no noise to the output. It has also been shown to be temporally [11], spatially [19, 31] and spectrally multi-mode [32]. Given that the warm vapour GEM storage time is limited by atomic motion, a cold atom version of this protocol is well motivated. To achieve this we first had to develop an ultra-high OD atomic source to allow for high efficiency recall.

The body of the paper is split into two sections: in section 2 we will present the experimental details of our cold atomic source; and in section 3 we will present the basic theory behind GEM and a high efficiency demonstration of GEM using cold atoms. In section 4 we discuss possible improvements and other experiments that could benefit from a high OD atomic source. Conclusions are presented in section 5.

2. The cold atomic source

The MOT is a workhorse of modern atomic physics as it offers the robust and efficient collection, cooling and storage of cold atoms. A typical MOT operating on ^{87}Rb will quickly cool (tens of milliseconds) and trap 10^8 atoms from a dilute thermal background gas at densities of approximately 10^{10} atoms cm^{-3} and temperatures on the order of 100 μK.

For quantum memory applications we aim to reach low temperatures and the very large ODs required for high efficiencies. Because OD is related to the integrated absorption of photons through a sample, there are a number of clear ways to increase the OD. These include increase the atom number (for instance by increasing the length of the cloud) or increase the density. Low temperature is also important as the thermal diffusion of atoms is a limiting factor for the memory lifetime. In addition, the memory cannot be operated while either the magnetic or optical trapping fields are active. Cold atoms expand ballistically when released from a MOT, with a typically Gaussian velocity distribution related to their kinetic temperature. The density of a sample decreases as it expands, reducing the OD. A lower temperature means a slower expansion of the cloud and therefore higher densities after switch off of the trap.

In the following we present a MOT that achieves a peak OD of over 1000 at a temperature of 200 μK. We obtain this result by optimizing both the static loading of the MOT through geometry, a spatial dark spot and optical de-pumping, followed by a compression phase using a temporal dark spot [33]. After describing the application of these techniques, we present a characterization of the system using near resonant absorption imaging.

2.1. Loading phase

Our ^{87}Rb MOT is in a three beam retro-reflection configuration. The trapping and cooling laser has a total power of 400 mW after spatial filtering and is red-detuned by 30 MHz from the D2 $F = 2 \rightarrow F' = 3$ transition for the loading of the MOT. The repumping field is on resonance with the D2 $F = 1 \rightarrow F' = 2$ transition, as shown in figure 1(a). Figure 1(b) shows the MOT beam configuration, with trapping and repump beams being combined on a polarizing beam-splitter (PBS) and then split further using another PBS (neither pictured) to create three cooling beams of approximately 3.5 cm diameter, all of which are then appropriately polarized and retro-reflected.

The optimal shape for our atomic ensemble is a cylinder along the direction of the memory beams to allow for maximum absorption of the probe. This can be achieved by using rectangular, rather than circular, quadrupole coils [34, 35] or using a 2D MOT configuration [26, 36].

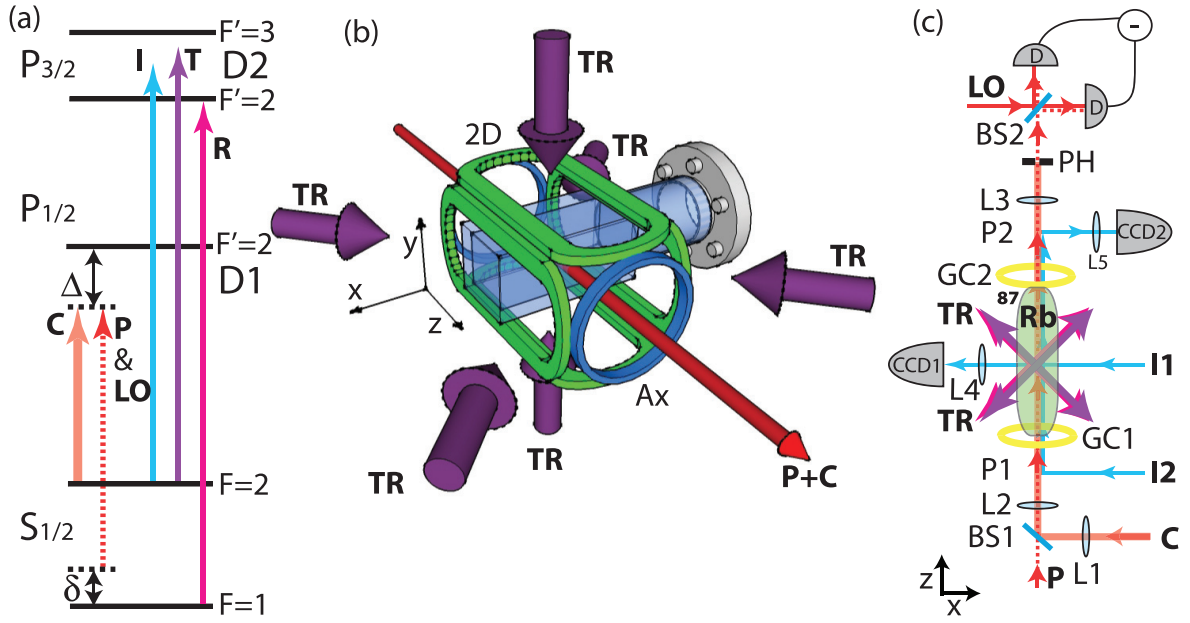

Figure 1. Experimental set-up. (a) Energy level diagram for all fields present: C—coupling; P—probe; LO—local oscillator; I—Imaging; T—trapping; R—repump. Also shown are one- and two-photon detunings for probe and coupling fields (Δ and δ respectively). (b) Three-dimensional (3D) representation of MOT configuration: TR—trapping and repump fields; 2D—x and y MOT coils (green); Ax—axial (z) coils (blue). (c) 2D schematic diagram of experiment: ^{87}Rb—atomic ensemble; BS—50:50 beam-splitter; L—lens; D—photo-diode detector; I1(2)—imaging beam 1(2); CCD—charged-coupled device camera; PH—pin-hole; GC—GEM coils; P1 and P2—positions for inserting mirrors for axial (z) imaging with I2. MOT coil configuration not shown, neither is vertical (y) MOT beam.

To create this shape while still allowing easy access for the memory beams we use four elongated coils in a quadrupole configuration to create a 2D MOT in the z direction (memory axis) and position the horizontal MOT beams at 45° to the long axis of the MOT. An extra set of axial coils in the z direction creates 3D confinement. The shape of the MOT can then be determined by the currents in the 2D and axial coils, as well as the relative intensities of the trapping fields.

For the loading phase, the cylindrically symmetric magnetic field gradient produced by the 2D MOT coils is 16 G cm^{-1}, and for the axial coils is 2 G cm^{-1}. The ^{87}Rb atoms are produced from a natural-mixture Rb dispenser inside a $100 \times 50 \times 50$ mm^3 single-sided, anti-reflection coated cell shown in figure 1(b). This cell is attached to a vacuum system consisting of a 70 L s^{-1} ion pump supplemented by a passive titanium sublimation pump; with the dispenser running in the cell we measure a background pressure at the ion pump of 1.5×10^{-9} kPa.

The density in the trapped atomic state ($F = 2$ here) is limited by reabsorption of fluorescence photons within the MOT (leading to an effective outwards radiation pressure [37]). By placing a dark spot of approximately 7.5 mm in diameter in the repump, atoms at the centre of the MOT are quickly pumped into the lower ground state ($F = 1$) and become immune to

this unwanted effect, allowing for a higher density of atoms in the centre of the trap, as first demonstrated in [38].

We can collect over 10^{10} atoms in this configuration. However, we find that the static MOT parameters that optimize atom number do not optimize density in the compression and cooling phase of the MOT, and we typically work with a sample of 4×10^9 atoms.

2.2. Compression phase

In this second stage of the ensemble preparation we utilize a temporal dark spot to transiently increase the density of the sample by simultaneously increasing the trapping laser and repump detunings and increasing the magnetic field gradient [33, 39, 40]. Detuning the trapping laser creates some of the conditions for polarization-gradient cooling [41], which can be used to achieve much colder and denser ensembles than in a standard MOT. We smoothly ramp the frequency of the trapping beam from 30 to 70 MHz below resonance, and the repump beam to 8 MHz below resonance, over a period of 20 ms. The 2D magnetic field gradient in the x and y directions is ramped up to $40\,\mathrm{G\,cm^{-1}}$ as the trapping and repump lasers are detuned. We do not ramp the axial field.

Finally, we optically pump the atoms into the desired ground state ($F = 1$, see figure 1(a)) by simply turning off the repump 50 μs before the trapping beam.

2.3. Magneto-optical trap characterization

Absorption imaging was used to optimize and characterize the MOT. The set-up and frequency of the imaging beams are shown in figure 1. We perform imaging both across (I1) and along (I2) the z-axis (in which case two mirrors are temporarily placed at locations P1 and P2).

Absorption imaging allows us to measure the OD of the MOT using Beer's law

$$\mathrm{OD} \simeq \ln(I_\mathrm{t}/I_\mathrm{o}), \tag{1}$$

where I_t is the transmitted imaging beam intensity after passing through the MOT and I_o is the intensity measured without the MOT present. This is calculated for every point in the imaging plane.

As the absorption of light by atoms away from resonance will follow a Lorentzian decay, to be able to have a precise value for OD it is important to have a well calibrated line centre. This is especially important as one goes further off resonance as the relation between on-resonance OD and off-resonance OD depends on the one-photon detuning (Δ) as follows:

$$\mathrm{OD}_\mathrm{res} = \frac{\Delta^2 + \gamma^2/4}{\gamma^2/4}\mathrm{OD}_\Delta, \tag{2}$$

where γ is the excited state decay rate. For Rb γ is approximately 6 MHz.

To measure Δ accurately we lowered the atom number in our trap until the OD did not saturate on resonance and plotted out the resonance curve as a function of detuning to accurately locate the line centre. This is shown in figure 2(a).

Images of the MOT for various configurations are shown in figure 3. For these imaging runs, we used a 4.98 s load time followed by 20 ms of ramping fields as described in section 2.2. All fields were then turned off and an image of the MOT was taken 500 μs later (unless otherwise stated), with a comparison image being taken 150 ms later to obtain as precise a measure of I_o as possible while ensuring no atoms were still present. As the imaging beam is on

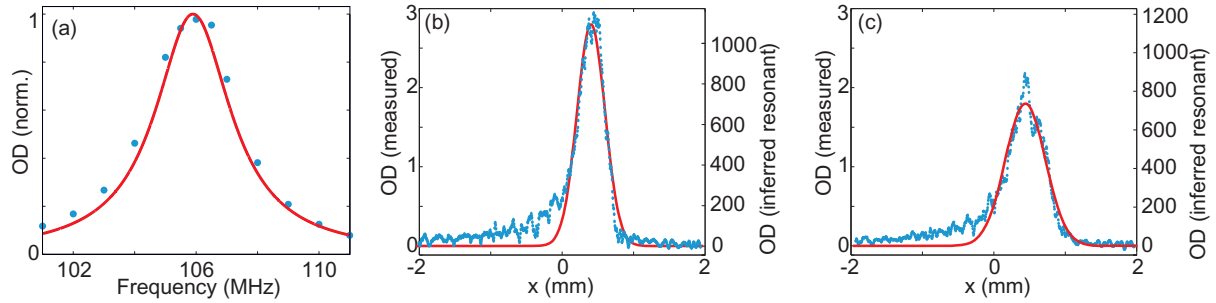

Figure 2. OD characterization. (a) Normalized OD as a function of imaging beam frequency, with low atom number. (b) Averaged scaled (left-hand scale) and unscaled (right-hand scale) OD cross-sections, taken across ten y-plane slices for seven traces, as a function of x position for an imaging beam detuning of -60.8 MHz from resonance (OD scale factor $= 410$) and (c) for $+59.2$ MHz (OD scale factor $= 390$). Points represent data, red lines represent fits (Lorentzian in (a) and Gaussian in (b) and (c)).

the closed D2 $F = 2 \rightarrow F' = 3$ transition, it was necessary to pump atoms back into the $F = 2$ state before these images were taken. This was achieved with a 200 μs pulse of on-resonance repump light immediately before the image. For side-on imaging the imaging beam was detuned by -20 MHz and front-on by -60 MHz to avoid complete absorption and therefore saturation of the measured OD, as well as diffraction effects.

Figure 3 shows images of the atomic ensemble for various MOT parameters. The images in figure 3(a) were taken of a cloud with all the optimization protocols described in sections 2.1 and 2.2, with approximately 4×10^9 atoms present. The peak, front-on OD was measured to be 1000 on resonance with the $F = 2 \rightarrow F' = 3$ transition. This was achieved by detuning the imaging beam approximately 60 MHz for both positive and negative detunings to ensure no diffraction effects were present and using equation (2). Two averaged uncalibrated OD cross-sections, taken across ten y-plane slices, for these detunings are shown in figures 2(b) and (c). The scaled peak ODs are 900 and 1100 for minus and plus detunings respectively. Averaging the maximum peak height of the individual traces gives over 1000 for both plus and minus detuning. The drop in the average cross-sections can therefore be attributed to slight movement of the MOT between images, with a narrower peak seen for the negative detuning. The temperature of this ensemble, determined by measuring the width of the expanding cloud 5, 10 and 15 ms after the fields were turned off, is approximately 200 μK in all directions.

Without the spatial dark spot, figure 3(b)(i) looks very similar to figure 3(a)(i). However, the front-on image in figure 3(b)(ii) shows that the maximum OD drops to 800 with 5×10^9 atoms. Figure 3(c) shows the 2D MOT created without turning on the axial coils. This ensemble is much longer in the z direction than the initial cloud (in fact so long that our imaging beam was not large enough to capture it all), but also contains only a quarter of the atoms. This meant that the peak OD dropped to about the same as that without the dark spot. The temperature in the x and y directions for the 2D MOT was approximately 100 μK but, as there is no trapping in the z direction, the temperature here was much larger.

Figure 3(iv) shows the ensemble without ramping up the 2D MOT magnetic field at the end of the run. This leads to a less-compressed cloud in all three dimensions, though mainly in the x–y plane, and therefore a much lower OD of approximately 500. Though there is less

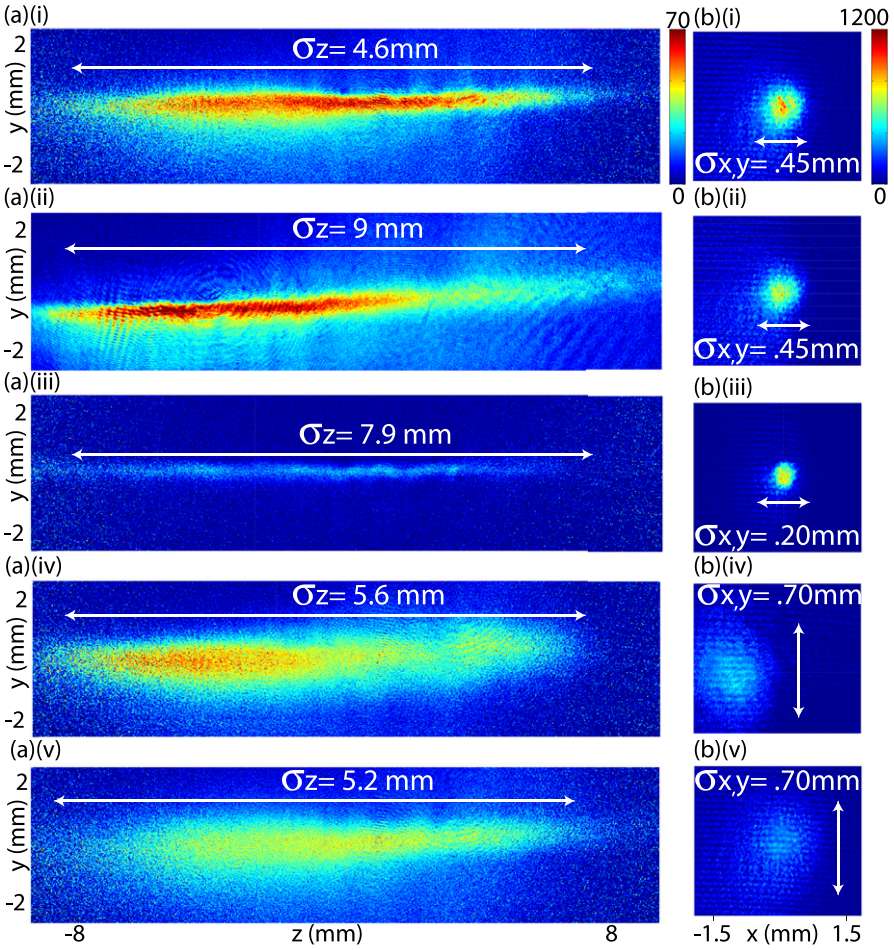

Figure 3. MOT characterization images. (a) Side-on and (b) front-on images of the atomic ensemble for various MOT parameters taken at 500 μs after fields turned off: (i) all optimization protocols described in text; (ii) no dark spot; (iii) no axial gradient; (iv) no magnetic field compression; and (v) same as (i) but 3 ms after fields turned off. Colour bars on (a) traces show OD scales, σ values show the standard deviation of Gaussian fits to ensemble.

magnetic field compression, the temperature of this cloud is the same as the original cloud in the x–y plane, with $T = 200\,\mu$K. However, in the z direction the cloud barely expands over 15 ms.

Finally, figure 3(v) shows the cloud from figure 3(i) expanded for 3 ms as opposed to 500 μs. The temperature of this cloud will be the same as the initial cloud and, due to the expansion, the peak OD has fallen to 400, though the atom number is still around 4×10^9.

3. Gradient echo memory (GEM)

3.1. GEM introduction

As its name suggests, the key to GEM is a linear frequency gradient η placed along an ensemble of two-level absorbers, as illustrated in figure 4. This makes GEM a frequency encoding memory, with information being stored as its spatial Fourier transform along the memory. The details of the scheme are covered in depth in previous papers [11, 18, 42–44].

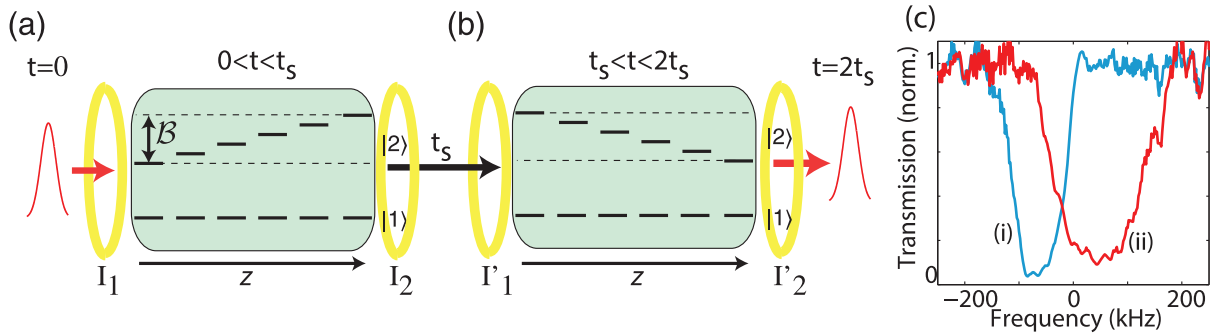

Figure 4. GEM scheme. (a) Storage: a pulse enters an ensemble of atoms with levels $|1\rangle$ and $|2\rangle$ at time 0 where the memory bandwidth $\mathcal{B} = \eta l$. The gradient η is created by a pair of coils with currents $I_2 > I_1$. (b) Retrieval: at time t_s the gradient is switched, with $I_1' = I_2$ and $I_2' = I_1$ and at time $2t_s$ the echo exits the memory. (c) Averaged and demodulated Raman absorption lines showing broadening due to (i) input gradient and (ii) output gradient.

The bandwidth of the system is given by $\mathcal{B} = \eta l$, where l is the length of the memory. When using alkali atoms, GEM is implemented using a ground state coherence, in our case between the $F = 1$ and 2 hyperfine states. These are coupled using a strong off-resonant coupling beam, as shown in figure 1, to make an ensemble of quasi-two-level atoms. The storage efficiency is determined by the off-resonance broadened Raman line to be

$$\epsilon_s = 1 - \exp\left(-2\pi \frac{\mathrm{OD}_{\mathrm{res}}}{\mathcal{B}'} \frac{\Omega_c^2}{\Delta^2}\right), \tag{3}$$

where Ω_c is the Rabi frequency of the coupling field and $\mathcal{B}'$ is the bandwidth normalized by the excited-state decay rate γ. To recall the light the gradient is reversed, with $\eta \to -\eta$. This causes a time reversal of the initial absorption process and the emission of a photon echo from the memory in the forward direction at time $2t_s$, where t_s is the time between pulse arrival and gradient reversal. The monotonicity of the gradient ensures that no light is re-absorbed as it leaves the memory and, as the process is symmetric, the recall efficiency is the same as the storage efficiency, giving a maximum total memory efficiency of $\epsilon_t = \epsilon_s^2$. This does not take into account any decoherence that may go on inside the memory. The detuned Raman absorption nature of GEM (i.e. $\mathrm{OD}_{\mathrm{Ram}} \propto (\Omega_c^2/\Delta^2)\mathrm{OD}_{\mathrm{res}}/\mathcal{B}$, where $\Omega_c/\Delta \ll 1$) means it requires a much higher OD than a transmissive memory like EIT. Measurements of the broadened Raman line are shown in figure 4(c) for both the storage and recall gradients. These measurements show that our writing gradient has a bandwidth of around 50 kHz and the recall gradient has a bandwidth of around 100 kHz.

3.2. GEM using cold atoms

In our experiment the probe, coupling and local oscillator (LO) fields are all derived from the same laser. The laser can either be locked to the D1 $F = 2 \to F' = 2$ transition, using saturated absorption spectroscopy, or placed near this transition, with the frequency being stabilized with a reference cavity. The probe and LO fields are shifted by 6.8 GHz to be resonant with the D1 $F = 1 \to F' = 2$ transition using a fibre-coupled electro-optic modulator. All three fields pass

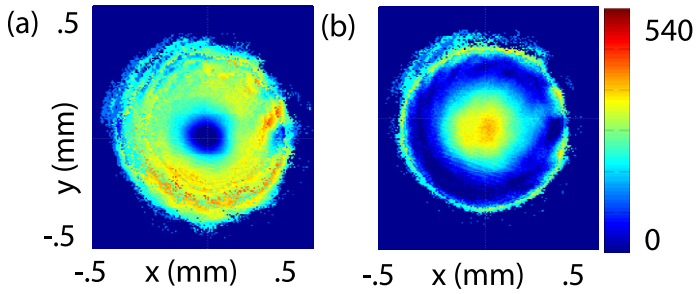

Figure 5. Probe Diffraction. CCD traces of probe transmission through MOT for (a) −40 MHz and (b) +40 MHz. Colour bar shows log absorption scale.

through separate acousto-optic modulators to allow for fine frequency adjustment, as well as gating and pulsing. The experimental set-up for the cold atom GEM experiment is shown in figure 1(b).

The reversible frequency gradients for GEM were created using two coils with a radius of 75 mm placed 70 mm apart around the centre of the MOT. These coils were driven with between 2 and 4 A. We also required that the gradient be switched quickly compared to the storage time and with minimal cross-coupling and oscillation after switching. Using a home-built actively stabilized metal oxide semiconductor field effect transistor (MOSFET) based switch we achieved switching in 1.5 μs to within 1% of the desired current.

The probe beam was focused into the MOT to access the highest ODs available in the atom cloud. Using lens L2 we formed a waist of 50 μm in the atom cloud. Using a CCD we investigated the probe beam transmission through the MOT as a function of detuning from the $F' = 2$ excited state. Two of these traces are shown in figure 5. We observe that the high density of the atom cloud causes lensing of the probe beam, which changes as a function of frequency. These CCD traces, combined with additional data from measurements made using an avalanche photodiode and weak probe pulses, indicate a resonant probe OD of around 300 on the D1 $F = 1 \rightarrow F' = 2$ transition.

To combine the probe and coupling fields we used a non-polarizing 50:50 beam-splitter (BS1 in figure 1). Unlike the probe, we want the coupling field to have a large diameter, to cover the entire ensemble with minimal variation in intensity. We use L1 to make a telescope with L2 (the focusing lens for the probe) to have a collimated coupling field with a waist of 1.25 mm. The reason we use a BS rather than a PBS is that it allows us to vary the probe and coupling polarizations, to which GEM is very sensitive [18]. After the MOT we filter the coupling field from the probe using lens L3 and a rectangular pinhole, with dimensions of $100 \times 200\,\mu\text{m}^2$. This removes over 99% of the coupling field and has a probe transmission efficiency of 90%. The mode selective heterodyne detection then sees no trace of the coupling field.

For the highest efficiency memory we used the MOT shown in figure 3(a) with a 480 ms load time. After this time the fields are ramped down for 20 ms, as described in section 2.2, and then all MOT fields are turned off. At this point the input gradient is turned on with the two GEM coils. After 500 μs, allowing eddy currents generated by the MOT coils to switch off, the coupling field is turned on and then the probe is pulsed into the ensemble. Though the MOT cannot fill completely in the 480 ms load time, by continually running the above sequence and having only a millisecond between turning off the MOT and turning it back on again, the atom number in the MOT saturates after only five cycles of the experiment.

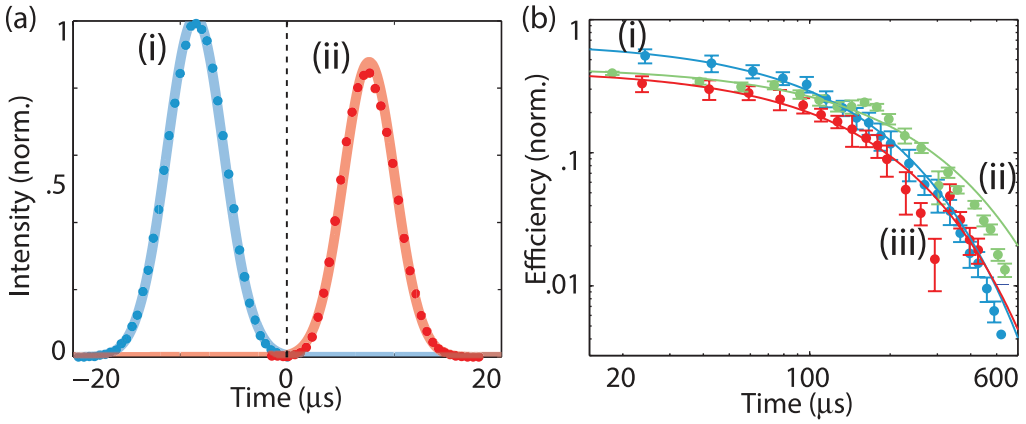

Figure 6. GEM with cold atoms. (a) High efficiency demodulated and squared heterodyne data: (i) input pulse (blue), and (ii) echo (red) at $80 \pm 2\%$ total efficiency. Points correspond to digitally demodulated data, averaged over 10 (17) traces for input (echo) and squared, error from standard deviation. Lines correspond to Gaussian fit. Dashed line indicates magnetic field switching at $t = 0$. (b) Log–log plot of memory efficiency as a function of storage time for (i) MOT shown in figure 3(a) (blue), (ii) MOT shown in figure 3(e) (green) and (iii) MOT shown in figure 3(c) (red).

We found a Gaussian pulse with a full-width-half-maximum of $10\,\mu$s to be optimal for storage. Longer pulses were affected by MOT decay, while shorter pulses required higher bandwidths that reduced the Raman absorption efficiency (see equation (3)). For this pulse length, a one-photon detuning of -250 MHz and approximately $350\,\mu$W in the coupling field (corresponding to a Rabi frequency of 2 MHz), we were able to demonstrate storage with $80 \pm 2\%$ total efficiency. This was measured by squaring the modulated pulse, finding the pulse shape and integrating and averaging over 10 input and 17 output pulses, the error coming from the standard deviation of these traces. This is shown in figure 6(a), with the data being digitally demodulated in phase, averaged and then squared to produce the intensity plot. As heterodyne detection is mode sensitive, care was taken to optimize the visibility for the input pulse, so that any change in the mode during storage would lead to a reduction in the measured efficiency.

To compare our memory to theoretical expectations, we need to know about the decay of the information stored in the memory and the OD. To investigate the decay we delayed the gradient switching time to store the pulse for longer periods inside the memory, while turning off the coupling field during the storage window. For the MOT used to obtain the 80% efficiency above we found an exponential decay with a time constant of $117\,\mu$s. The OD can be found directly from the storage data where we observed 2% leakage of the probe field during the write phase. Assuming symmetric read and write operations, the total efficiency of $20\,\mu$s storage can be estimated as $0.98 \times 0.98 \times \mathrm{e}^{-20/117} = 81\%$. We know from measurements of the broadened Raman lines (figure 4(c)) that the write and read stages are not perfectly symmetric, however the observed efficiency is still compatible with these measured bandwidths. We can also crosscheck this result using equation (3). Taking the resonant OD of 150 (as only half the atoms reside in the m_F state used for the memory), the measured bandwidth of the read and write Raman lines and the decay time, we again estimate 81% total efficiency for our memory.

To investigate the source of the memory decoherence we also measured the decay of the stored light for two other MOT configurations. Firstly, we added a longer waiting period after switching off the MOT: 3 ms (figure 3(v)) instead of 500 μs. This avoids any residual magnetic fields caused by eddy currents and resulted in an exponential time constant of 195 μs, though with a lower initial efficiency due to lower initial OD. As the temperature of clouds (i) and (v) are the same, this indicates that temperature is not limiting the coherence time. This is also apparent from the exponential form of the decay: if it were temperature-limited we would expect a Gaussian decay due to the thermal expansion discussed in section 2.

We also investigated the decay using a cloud without the axial coils (figure 3(c)). The initial efficiency was again lower than with the initial MOT, due to the lower OD and size of the cloud, and the time constant was 133 μs. This indicates the axial diffusion is not the limiting factor for the initial MOT decay, as the initial MOT had a much lower temperature in the z direction. The investigation of decoherence in this system is the subject of ongoing work.

4. Discussion

While 80% total efficiency is, to the best of our knowledge, the highest efficiency so far reported for cold atomic ensembles, we have numerous paths for further improvement on this result. As with all atomic memory experiments, OD is a necessary condition for high efficiency. In our case, even with the large OD we have achieved, it is still the primary limit to our experiment. One limiting factor on OD is that, when pumped into the $F = 1$ state, approximately half the atoms end up in the $m_F = 1$ state used for the memory and half in the $m_F = 0$. If we implemented an optical pumping scheme similar to the one in [45] we anticipate an increase in the OD by a factor of two.

The storage time can also be improved by removing sources of decoherence. One potential factor behind the decoherence could be inhomogeneous background magnetic fields, partly due to eddy currents created by the switch off of the MOT coils. Improving this situation may require improvements to switching electronics and physical redesign of the coil configuration. Atomic diffusion will clearly also play a role, so further reductions in temperature will be advantageous. One more extreme measure would be to transfer atoms into an optical lattice. The increase in coherence time afforded by such a measure must, however, be balanced against the likely decrease in atom number and thus storage efficiency.

Even without further improvement, our memory provides an excellent high-OD platform for numerous other proof-of-principle experiments. We have proposed previously that the magnetic field gradient could be replaced with an optical (ac Stark) gradient [46]. Combining this with spatial light modulators and Pockels cells would give switching down to nanoseconds and fine control over the gradient and therefore allow for precision manipulation of the stored information, as discussed in [32, 47]. Another interesting possibility is to investigate cross-phase modulation [48], where the high OD, small interaction volume and long storage times are highly advantageous.

5. Conclusions

In this paper we have developed a cold atomic ensemble with 4×10^9 atoms and a peak OD of 1000 on the D2 $F = 2 \rightarrow F' = 3$ transition, specifically with quantum memory applications in mind. We used this ultra-high OD system to demonstrate the GEM scheme on the D1 line

with a total efficiency of up to $80 \pm 2\%$ for pulses with a full-width-half-maximum of $10\,\mu$s, still limited primarily by the OD. The decoherence of the system was found to be exponential, with a time constant of 117–195 μs depending on the MOT parameters used, representing an improvement of a factor of 2–4 over the warm GEM experiment.

Acknowledgments

Thanks to Colin Dedman for his help designing the fast switching GEM coils. This research was conducted by the Australian Research Council Centre of Excellence for Quantum Computation and Communication Technology (project number CE110001027). NPR is supported by an Australian Research Council QEII Fellowship. QG is supported by the AFSOR and the Physics Frontier Center at the NIST/UMD Joint Quantum Institute.

References

[1] Bennett C H and Brassard G 1984 Quantum cryptography: public key distribution and coin tossing *Proc. IEEE Int. Conf. on Computers, Systems, and Signal Processing* (*Bangalore, India*) pp 175–9
[2] Wang S, Chen W, Guo J-F, Yin Z-Q, Li H-W, Zhou Z, Guo G-C and Han Z-F 2012 2 GHz clock quantum key distribution over 260 km of standard telecom fiber *Opt. Lett.* **37** 1008–10
[3] Duan L-M, Lukin M D, Cirac J I and Zoller P 2001 Long-distance quantum communication with atomic ensembles and linear optics *Nature* **414** 413–8
[4] Hammerer K, Sørensen A and Polzik E 2010 Quantum interface between light and atomic ensembles *Rev. Mod. Phys.* **82** 1041–93
[5] Sangouard N, Simon C, de Riedmatten H and Gisin N Quantum repeaters based on atomic ensembles and linear optics *Rev. Mod. Phys* **83** 33–80
[6] Wolfgramm F, Xing X, Cerè A, Predojević A, Steinberg A M and Mitchel M W 2008 Bright filter-free source of indistinguishable photon pairs *Opt. Express* **16** 18145–51
[7] Zhang H *et al* 2011 Preparation and storage of frequency-uncorrelated entangled photons from cavity-enhanced spontaneous parametric downconversion *Nature Photon.* **5** 628–32
[8] Glorieux Q, Clark J B, Corzo N V and Lett P D 2012 Generation of pulsed bipartite entanglement using four-wave mixing *New J. Phys.* **14** 123024
[9] Simon C, de Riedmatten H, Afzelius M, Sangouard N, Zbinden H and Gisin N 2007 Quantum repeaters with photon pair sources and multimode memories *Phys. Rev. Lett.* **98** 190503
[10] Collins O A, Jenkins S D, Kuzmich A and Kennedy T A B 2007 Multiplexed memory-insensitive quantum repeaters *Phys. Rev. Lett.* **98** 060502
[11] Hosseini M, Sparkes B M, Campbell G, Lam P K and Buchler B C 2011 High efficiency coherent optical memory with warm rubidium vapour *Nature Commun.* **2** 174
[12] Reim K F, Nunn J, Lorenz V O, Sussman B J, Lee K C, Langford N K, Jaksch D and Walmsley I A 2010 Towards high-speed optical quantum memories *Nature Photon.* **4** 218–21
[13] Reim K F, Michelberger P, Lee K C, Nunn J, Langford N K and Walmsley I A 2011 Single-photon-level quantum memory at room temperature *Phys. Rev. Lett.* **107** 053603
[14] Longdell J J, Fraval E, Sellars M J and Manson N B 2005 Stopped light with storage times greater than one second using electromagnetically induced transparency in a solid *Phys. Rev. Lett.* **95** 063601
[15] Hedges M P, Longdel J J, Li Y and Sellars M J 2010 Efficient quantum memory for light *Nature* **465** 1052–6
[16] Amari A *et al* 2010 Towards an efficient atomic frequency comb quantum memory *J. Lumin.* **130** 1579–85
[17] Bonarota M, Le Gouët J-L and Chanelière T 2011 Highly multimode storage in a crystal *New J. Phys.* **13** 013013

[18] Hosseini M, Sparkes B M, Campbell G T, Lam P K and Buchler B C 2012 Storage and manipulation of light using a Raman gradient-echo process *J. Phys. B: At. Mol. Opt. Phys.* **45** 124004
[19] Higginbottom D, Sparkes B M, Rancic M, Pinel O, Hosseini M, Lam P K and Buchler B C 2012 Spatial-mode storage in a gradient-echo memory *Phys. Rev.* A **86** 023801
[20] Phillips N B, Gorshkov A V and Novikova I 2008 Optimal light storage in atomic vapor *Phys. Rev.* A **78** 023801
[21] Balabas M V, Jensen K, Wasilewski W, Krauter H, Madsen L S, Müller J H, Fernholz T and Polzik E S 2010 High quality anti-relaxation coating material for alkali atom vapor cells *Opt. Express* **18** 5825–30
[22] Balabas M, Karaulanov T, Ledbetter M and Budker D 2010 Polarized alkali-metal vapor with minute-long transverse spin-relaxation time *Phys. Rev. Lett.* **105** 070801
[23] Zhang R, Garner S R and Hau L V 2009 Creation of long-term coherent optical memory via controlled nonlinear interactions in Bose–Einstein condensates *Phys. Rev. Lett.* **103** 233602
[24] Sagi Y, Almog I and Davidson N 2010 Process tomography of dynamical decoupling in a dense cold atomic ensemble *Phys. Rev. Lett.* **105** 053201
[25] Dudin Y O, Li L and Kuzmich A 2013 Light storage on the time scale of a minute *Phys. Rev.* A **87** 031801
[26] Zhang S, Zhou S, Loy M M T and Wong G K L 2011 Optical storage with electromagnetically induced transparency in a dense cold atomic ensemble *Opt. Lett.* **36** 4530–2
[27] Riedl S, Lettner M, Vo C, Baur S, Rempe G and Dürr S 2012 Bose–Einstein condensate as a quantum memory for a photonic polarization qubit *Phys. Rev.* A **85** 022318
[28] Chen Y-H, Lee M-J, Wang I, Du S, Chen Y-F, Chen Y-C and Yu I A 2012 Coherent optical memory with high storage efficiency and large fractional delay *Phys. Rev. Lett.* **110** 083601
[29] Bao X-H *et al* 2012 Efficient and long-lived quantum memory with cold atoms inside a ring cavity *Nature Phys.* **8** 517–21
[30] Arikawa M, Honda K, Akamatsu D, Nagatsuka S, Akiba K, Furusawa A and Kozuma M 2010 Quantum memory of a squeezed vacuum for arbitrary frequency sidebands *Phys. Rev.* A **81** 021605
[31] Glorieux Q, Clark J B, Marino A M and Zhou Z 2012 Temporally multiplexed storage of images in a gradient echo memory *Opt. Express* **20** 12350–8
[32] Sparkes B M, Hosseini M, Cairns C, Higginbottom D, Campbell G T, Lam P K and Buchler B C 2012 Precision dpectral manipulation: a demonstration using a coherent optical memory *Phys. Rev.* X **2** 021011
[33] DePue M T, Winoto S L, Han D J and Weiss D S 2000 Transient compression of a MOT and high intensity fluorescent imaging of optically thick clouds of atoms *Opt. Commun.* **180** 73–9
[34] Lin Y-W, Chou H-C, Dwivedi P P, Chen Y-C and Yu I A 2008 Using a pair of rectangular coils in the MOT for the production of cold atom clouds with large optical density *Opt. Express* **16** 3753–61
[35] Peters T, Chen Y, Wang J-S, Lin Y-W and Yu I A 2009 Optimizing the retrieval efficiency of stored light pulses *Opt. Express* **17** 6665–75
[36] Zhang S, Chen J F, Liu C, Zhou S, Loy M M T, Wong G K L and Du S 2012 A dark-line two-dimensional magneto-optical trap of ^{85}Rb atoms with high optical depth *Rev. Sci. Instrum.* **83** 073102
[37] Metcalf H J and van der Straten P 2003 Laser cooling and trapping of atoms *J. Opt. Soc. Am.* B **20** 887–908
[38] Ketterle W, Davis K B, Joffe M A, Martin A and Pritchard D E 1993 High densities of cold atoms in a dark spontaneous-force optical trap *Phys. Rev. Lett.* **70** 2253–6
[39] Lee H J, Adams C S, Kasevich M and Chu S 1996 Raman cooling of atoms in an optical dipole trap *Phys. Rev. Lett.* **76** 2658–61
[40] Petrich W, Anderson M H, Ensher J R and Cornell E A 1994 Behavior of atoms in a compressed magneto-optical trap *J. Opt. Soc. Am.* B **11** 1332–5
[41] Dalibard J and Cohen-Tannoudji C 1989 Laser cooling below the Doppler limit by polarization gradients: simple theoretical models *J. Opt. Soc. Am.* B **6** 2023–45
[42] Hétet G, Hosseini M, Sparkes B M, Oblak D, Lam P K and Buchler B C 2008 Photon echoes generated by reversing magnetic field gradients in a rubidium vapor *Opt. Lett.* **33** 2323–5
[43] Hosseini M, Sparkes B M, Hétet G, Longdell J J, Lam P K and Buchler B C 2009 Coherent optical pulse sequencer for quantum applications *Nature* **461** 241–5

Chapter 3

Quantum optics in anomalous dispersion media

List of publications related to this chapter :

- **Imaging using quantum noise properties of light**.
  J. B. Clark, Z. Zhou, **Q. Glorieux**, A. M. Marino and P. D. Lett.
  Optics Express **20**, 17050 (2012)

- **Quantum mutual information of an entangled state propagating through a fast-light medium**.
  J. B. Clark, R. T. Glasser, **Q. Glorieux**, U. Vogl, T. Li, K. M. Jones, and P. D. Lett. Nature Photonics **14**, 123024 (2014)

- **Generation of pulsed bipartite entanglement using four-wave mixing**.
  Q. Glorieux, J. B. Clark, N. V. Corzo, and P. D. Lett.
  New Journal of Physics **14**, 123024 (2012). Not included.

- **Extracting spatial information from noise measurements of multi-spatial-mode quantum states**.
  A. M. Marino, J. B. Clark, **Q. Glorieux** and P. D. Lett.
  European Physical Journal D **66**, 288 (2012). Not included.

- **Rotation of the noise ellipse for squeezed vacuum light generated via four-wave mixing**.
  N. V. Corzo, **Q. Glorieux**, A. M. Marino, J. B. Clark, R. T. Glasser and P. D. Lett. Physical Review A **88**, 043836 (2013). Not included.

- **Experimental characterization of Gaussian quantum discord generated by four-wave mixing**.
  U. Vogl, R. T. Glasser, **Q. Glorieux**, J. B. Clark, N. V. Corzo, and P. D. Lett. New Journal of Physics **87**, 010101 (2013). Not included.

- **Advanced quantum noise correlations**.
  U. Vogl, R. T. Glasser, J. B. Clark, **Q. Glorieux**, T. Li, N. V. Corzo, and P. D. Lett. New Journal of Physics **16**, 013011 (2014). Not included.

Introduction

A large part of my work at NIST-JQI has been devoted to the study and use of noise properties of entangled beams generated using four-wave-mixing in warm atomic vapor. It is not possible to describe here all these experiments but I will highlight two results that are valuable in relation to the other works presented in this manuscript.

We have seen in the previous chapter that GEM has the ability to store multiple spatial modes in the transverse direction. In the first experiment that I describe in this chapter, we used the multimode properties of to quantum noise [48] to be able to identify an object with a higher precision than would normally be achieved with a typical laser.

The second result I will comment concerns the study of the opposite process of a quantum memory: advancing quantum information [32]. We shown that under certain conditions, an atomic vapor can exhibit an anomalous dispersion and give rise to a group velocity larger than c. In the context of quantum communication, these results can be shocking as it is clear that no signal can travel faster than light [49]. However, we demonstrated the role of quantum noise to erase all information while velocity becomes larger than c.

3.1 Imaging with the noise of light

Imagine that you have an object (an intensity or a phase mask) that you want to image but you are also limited in the number of photons you can send onto this object. We propose two techniques (one *classical* using thermal noise and one *quantum* using quantum correlations) and compare the uncertainty in shape estimation between both. To simplify the comparison we restricted the shape estimation to a 1D problem.
The resource needed for this experiment is a pair of squeezed vacuum beams generated using four-wave-mixing in a atomic vapor. These beams are too weak to be measured directly with an amplified photodiode and need to be homodyned with local oscillators to be detected. Taken independently both beams (also known as probe and conjugate) exhibit an excess noise compared to a coherent state. They are indeed thermal states. However, when the intensity difference or the phase sum is analyzed, we observed a noise below the shot noise indicating quantum correlations.
The parameter we are trying to estimate is the angle of a bow-tie mask (1D problem) placed on the conjugate path. To do so the local oscillator (LO) is designed with a bow-tie shape of same size and same center as the mask, using a spatial light modulator. However the orientation of the mask is unknown.

The *classical* technique consists in overlapping the bow-tie shaped LO with the conjugate beam (after the mask) and measure the detected noise. The LO is then rotated and when the noise is maximized, the search is finished and the LO angle is an estimation of the mask angle. Indeed the fraction of the conjugate beam which passes through the mask contains spatial modes with extra-thermal noise compared to vacuum. In the limiting case of zero overlap between the LO

and the mask, the LO will just beat with vacuum and detect shot noise because no light coming from the conjugate beams interfere with it.

The *quantum* technique makes use of the second part of the entangled pair (the probe beam), which surprisingly does not have to interact directly with the mask. For this measurement, we simply added a second LO with the same angle to beat with the probe beam and then measured the quadrature that minimized the detected noise. This time, the search is terminated when the quadrature noise is minimal. In the paper *Imaging using the quantum noise properties of light*, we have demonstrated that the precision in the estimation of the mask angle is enhanced by a factor 6 with the quantum technique compared to the classical one, even though the second beam does not interact directly with the mask.

The second experiment described in this paper is a direct application of this principle to the field of pattern recognition. We start by defining a pattern set (the alphabet letters). We are able to imprint this set on the local oscillator with a spatial light modulator as shown in figure 3.1. An unknown mask from the set is placed in the path of the conjugate beam and we compare the two techniques to see if pattern recognition is enhanced using quantum correlations.

On the presented results (mask of the letter Z) by taking into account the uncertainty on the noise measurements it is not possible to conclude on the pattern in the classical case because more than one pattern noise measurement lie within one standard deviation. On the quantum case however, the letter Z is identified with more than 7 standard deviation certainty.

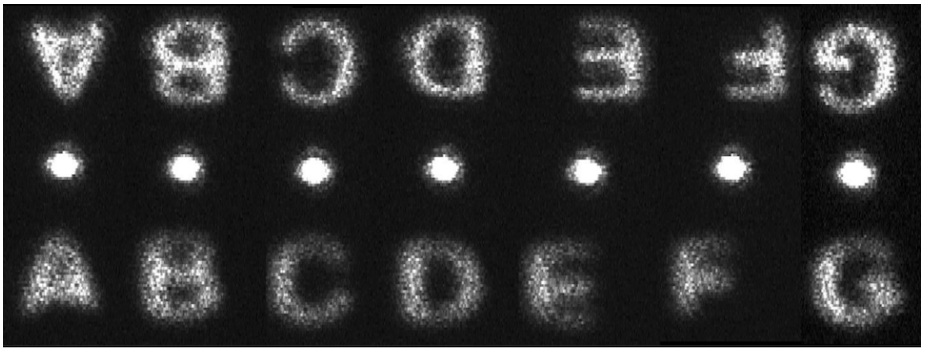

Figure 3.1: Example of probe and conjugate LO shape created using a spatial light modulator. The intense dot in the middle is the (filtered) pump beam. Each letter is an independent image and they are collated for presentation.

Imaging using quantum noise properties of light

Jeremy B. Clark,[1*] **Zhifan Zhou,**[1,2] **Quentin Glorieux,**[1] **Alberto M. Marino,**[1] **and Paul D. Lett**[1]

[1]*Quantum Measurement Division, National Institute of Standards and Technology, and Joint Quantum Institute, NIST and University of Maryland, 100 Bureau Dr., Gaithersburg, MD 20899-8424, USA*

[2]*Quantum Institute for Light and Atoms, State Key Laboratory of Precision Spectroscopy, Department of Physics, East China Normal University, Shanghai 200062, China*

[*]*jeremy.clark@nist.gov*

Abstract: We show that it is possible to estimate the shape of an object by measuring only the fluctuations of a probing field, allowing us to expose the object to a minimal light intensity. This scheme, based on noise measurements through homodyne detection, is useful in the regime where the number of photons is low enough that direct detection with a photodiode is difficult but high enough such that photon counting is not an option. We generate a few-photon state of multi-spatial-mode vacuum-squeezed twin beams using four-wave mixing and direct one of these twin fields through a binary intensity mask whose shape is to be imaged. Exploiting either the classical fluctuations in a single beam or quantum correlations between the twin beams, we demonstrate that under some conditions quantum correlations can provide an enhancement in sensitivity when estimating the shape of the object.

© 2012 Optical Society of America

OCIS codes: (270.0270) Quantum optics; (270.6570) Squeezed states.

References and links

1. V. Giovannetti, S. Lloyd, and L. Maccone, "Advances in quantum metrology," Nature Photon **5**, 222–229 (2011).
2. M. I. Kolobov, "The spatial behavior of non-classical light," Rev. Mod. Phys. **71**, 1539–1589 (1999).
3. M. I. Kolobov, *Quantum Imaging*, 1st ed. (Springer, 2006).
4. N. Corzo, A. M. Marino, K. M. Jones, and P. D. Lett, "Multi-spatial-mode single-beam quadrature squeezed states of light from four-wave mixing in hot rubidium vapor," Opt. Express **19**, 21358–21369 (2011).
5. V. Boyer, A. M. Marino, and P. D. Lett, "Generation of spatially broadband twin beams for quantum imaging," Phys. Rev. Lett. **100**, 143601 (2008).
6. M. I. Kolobov and C. Fabre, "Quantum limits on optical resolution," Phys. Rev. Lett. **85**, 3789–3792 (2000).
7. N. Treps, N. Gross, W. P. Bowen, C. Fabre, H.-A. Bachor, and P. K. Lam, "A quantum laser pointer," Science **301**, 940–943 (2003).
8. V. Giovannetti, S. Lloyd, and L. Maccone, "Sub-Rayleigh-diffraction-bound quantum imaging," Phys. Rev. A **79**, 013827 (2009).
9. N. Treps, U. Andersen, B. Buchler, P. K. Lam, A. Maitre, H.-A. Bachor, and C. Fabre, "Surpassing the standard quantum limit for optical imaging using nonclassical multimode light," Phys. Rev. Lett **88**, 203601 (2002).
10. J. A. Levenson, I. Abram, T. Rivera, and P. Grangier, "Reduction of quantum noise in optical parametric amplification," JOSA B **10**, 2233–2238 (1993).
11. E. Brambilla, L. Caspani, O. Jedrkiewicz, L. A. Lugiato, and A. Gatti, "High-sensitivity imaging with multi-mode twin beams," Phys. Rev. A **77**, 053807 (2008).
12. L. A. Lugiato, and A. Gatti, "Spatial structure of a squeezed vacuum," Phys. Rev. Lett. **70**, 3868–3871 (1993).
13. A. Gatti and L. Lugiato, "Quantum images and critical fluctuations in the optical parametric oscillator below threshold," Phys. Rev. A **52**, 1675–1690 (1995).

#169416 - $15.00 USD Received 25 May 2012; revised 29 Jun 2012; accepted 29 Jun 2012; published 11 Jul 2012

14. A. M. Marino, J. B. Clark, Q. Glorieux, and P. D. Lett, E-print arXiv:1203.0577v1.
15. G. Brida, M. Genovese, and I. Ruo Berchera, "Experimental realization of sub-shot-noise quantum imaging," Nature Photon **4**, 227–230 (2010).
16. A. F. Abouraddy, B. E. A. Saleh, A. V. Sergienko, and M. C. Teich, "Role of entanglement in two-photon imaging," Phys. Rev. Lett. **87**, 123602 (2001).
17. Q. Glorieux, R. Dubessy, S. Guibal, L. Guidoni, J.-P. Likforman, T. Coudreau, and E. Arimondo, "Double-Λ microscopic model for entangled light generation by four-wave mixing," Phys. Rev. A **82**, 033819 (2010).
18. C. F. McCormick, A. M. Marino, V. Boyer, and P. D. Lett, "Strong low-frequency quantum correlations from a four-wave-mixing amplifier," Phys. Rev. A **78**, 043816 (2008).
19. K. McKenzie, E. E. Mikhailov, K. Goda, P. K. Lam, N. Grosse, M. B. Gray, N. Mavalvala, and D. E. McClelland, "Quantum noise locking," J. Opt. B **7**, S421–S428 (2005).
20. V. Boyer, A. Marino, R. C. Pooser, and P. D. Lett, "Entangled images four four-wave mixing," Science **321**, 544 –547 (2008).
21. M. Martinelli, N. Treps, S. Ducci, S. Gigan, A. Maitre, and C. Fabre, "Experimental study of the spatial distribution of quantum correlations in a confocal optical parametric oscillator," Phys. Rev. A **67**, 023808 (2003).
22. A. Gatti, E. Brambilla, M. Bache, and L. A. Lugiato, "Correlated imaging, quantum and classical," Phys. Rev. A **70**, 013802 (2004).
23. C. Kim and P. Kumar, "Quadrature-squeezed light detection using a self-generated matched local oscillator," Phys. Rev. Lett. **73**, 1605–1608 (1994).
24. M. B. Nasr, D. P. Goode, N. Nguyen, G. Rong, L. Yang, B. M. Reinhard, B. E. A. Saleh, M. C. Teich, "Quantum optical coherence tomography of a biological sample," Opt. Commun. **282**, 1154–1159 (2009).

1. Introduction

The use of quantum correlated resources to enhance sensing and measurement has been an active field of research in recent years [1]. Multi-spatial-mode quantum states of light have become available [2–5] and have allowed for the development of imaging techniques that can surpass classical limits on resolution [6–8] or enhance signal-to-noise [9–11]. Here we present a technique that exploits the noise properties of multi-spatial-mode vacuum-squeezed twin beams to detect the shape of an object being probed by one of the beams. While we are able to estimate the shape of the object by monitoring only the fluctuations of the beam that probes it, we obtain an enhancement in this estimation sensitivity under certain conditions by exploiting the quantum correlations between the twin beams.

It is possible to estimate the shape of a binary (hard-apertured) intensity mask by probing it with a light field and performing a homodyne detection of the light that passes through it. The local oscillator (LO) spatially selects which portions of the probing field are detected, so the homodyne detection effectively acts as an imaging device [12,13]. By optimizing the shape of the LO to maximize the mode matching with the probing field after the mask (the LO-mask overlap), the object's shape can be inferred. If the mask is probed with a state of light consisting of a small number of photons, determining the mean value of the field becomes difficult due to unavoidable quantum noise. We can, however, use the same homodyne technique to measure the noise of the field rather than its mean value in order to extract information about the object's shape. Homodyne detection provides the additional advantage of allowing the discrimination of a signal against a background at other wavelengths.

A coherent state would not be a suitable choice to probe the mask since it is a displaced vacuum state. Its noise properties would thus remain unchanged regardless of how the probe field is altered or attenuated by the mask [14]. On the other hand, a state whose quadrature fluctuations are not at the shot noise limit (SNL) can provide information about the shape of the mask. For example, if a thermal state is used, the mask's shape can be estimated by manipulating the shape of the LO to optimize the geometric overlap between the field that passes through the mask and the LO to maximize the detected level of excess noise relative to the SNL. Since thermal states are classically obtainable, we will refer to such a single-beam method as a classical noise imaging technique.

In many situations a reference beam is used to eliminate correlated sources of noise and

#169416 - $15.00 USD Received 25 May 2012; revised 29 Jun 2012; accepted 29 Jun 2012; published 11 Jul 2012
(C) 2012 OSA

to improve the signal-to-noise ratio for a given measurement [15, 16]. We extend this idea to noise imaging by exploiting the quantum correlations between vacuum-squeezed twin beams to improve the estimation of the shape of the mask over the classical noise imaging technique described above. We refer to this two-beam technique as a quantum noise imaging technique. In this paper, we use twin beams generated by four-wave mixing (4WM) to directly compare these two techniques and find that the quantum technique provides an enhanced sensitivity to changes in the LO-mask overlap and thus a greater confidence in estimating the shape of the mask.

2. Four-wave mixing and squeezed light detection

To generate the light states needed for this experiment, we have used 4WM in a double-Λ configuration [17] in a hot ^{85}Rb vapor (Fig. 1(a)-(b)). The 4WM process converts two photons from a single pump beam into a pair of photons emitted into twin fields referred to as the probe and conjugate. These twin beams exhibit strong amplitude correlations such that the amplitude difference noise is below the SNL [18]. Taken individually, these fields are thermal states exhibiting uniformly distributed excess noise.

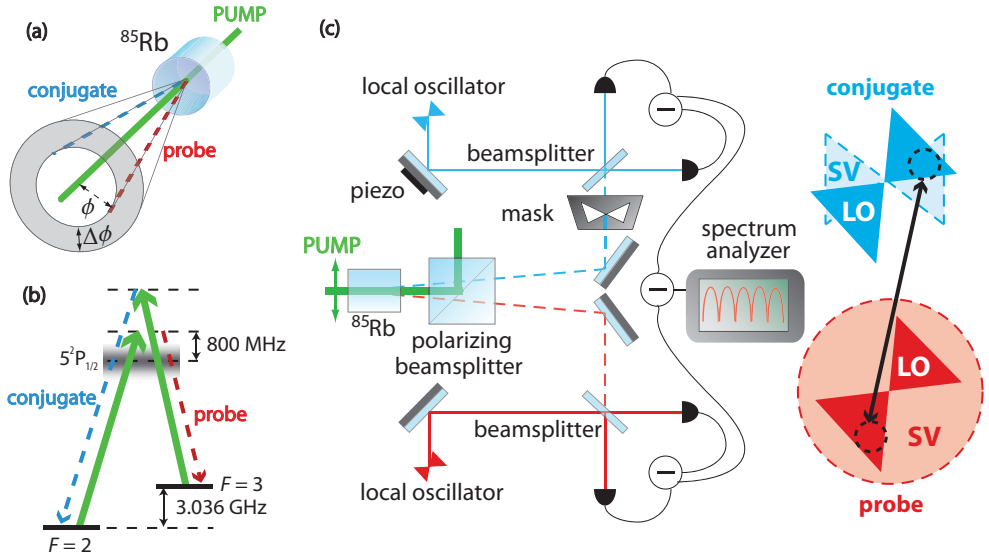

Fig. 1. (a) Four-wave mixing in ^{85}Rb. Probe and conjugate fields are coupled over a range of angles $\Delta\phi$ and selected for measurement via homodyne detection at ϕ. (b) Double-Λ scheme in ^{85}Rb. (c) Experimental set-up. Probe and conjugate local oscillators are shaped into bow ties and are rotated with respect to the mask. Resultant homodyne signals are subtracted. The black dotted circles joined by the arrow indicate coherence areas, localized regions of correlations between the probe and conjugate. LO denotes the local oscillator and SV the squeezed vacuum light.

Quantum correlations between the probe and the conjugate can be measured by performing a balanced homodyne detection of each field and subtracting the homodyne signals for appropriately chosen phases of the LOs. The noise of a single mode's generalized quadrature $\hat{X}_\theta = \frac{1}{\sqrt{2}}(\hat{a}^\dagger e^{i\theta} + \hat{a}e^{-i\theta}) = \hat{X}\cos\theta + \hat{Y}\sin\theta$ is measured by choosing the LO phase θ. We subtract the noise of the probe and conjugate generalized quadratures to obtain the noise of the joint quadrature $\hat{X}^J_\theta = \hat{X}^p_{\theta_p} - \hat{X}^c_{\theta_c}$. Given probe and conjugate LO phases respectively denoted by

#169416 - $15.00 USD Received 25 May 2012; revised 29 Jun 2012; accepted 29 Jun 2012; published 11 Jul 2012
(C) 2012 OSA

θ_p and θ_c, $\hat{X}^J_\theta$ is squeezed under the condition that $\theta_p + \theta_c = \pi$. We therefore only need to control the phase of one of the LOs (using a PZT-mounted mirror) to detect the level of squeezing between the probe and conjugate.

To implement the 4WM process, a linearly polarized intense pump beam (300 mW) is focused down to a $\frac{1}{e^2}$ diameter of 1.2 mm inside a 1.25 cm long ^{85}Rb cell heated to 110°C. The probe and conjugate frequencies are unseeded, so the resulting probe and conjugate fields are generated from spontaneous emission. The frequency of the pump beam is detuned 800 MHz to the blue of the $|5^2S_{1/2}, F = 2\rangle \rightarrow |5^2P_{1/2}, F = 3\rangle$ transition at 795 nm. After separating the pump beam from the probe and conjugate beams with a polarizing beam splitter, each beam is sent to a balanced homodyne detector using a pair of matched photodiodes with quantum efficiencies of approximately 95%. The total optical path losses from the 4WM process to the homodyne detection are approximately 4%.

3. Experimental procedure

To characterize each technique's sensitivity we reduced the LO search to a one-dimensional problem by choosing our mask to be in the shape of a bow tie that can be oriented at an arbitrary angle around its center of symmetry (Fig. 1(c)). The position of the center of symmetry was fixed, and the only free parameter to be estimated was the mask's angular orientation. We generated probe and conjugate LOs with congruent bow tie shapes but rotated at an arbitrary common angle relative to the mask. The estimated parameter is the overlap between the conjugate after the mask and its LO, which is a function of the angle. We then recorded the resultant quadrature noise powers with a spectrum analyzer as a function of the overlap for the classical and quantum noise imaging techniques. In order to reliably measure the amount of squeezing in the quantum case, the phases of the LOs were quantum noise locked [19] such that the twin beam quadrature noise difference was always minimized for each overlap value.

An important feature of the correlated fields generated by our 4WM set-up is that they are multi-spatial-mode [20], which can in general provide greater flexibility in obtaining an enhancement with these states [14]. Quantum correlations between the probe and conjugate are localized to pairwise correlated regions within the beams referred to as coherence areas [21,22] (Fig. 1(c)). In order to measure and compare only correlated coherence areas we symmetrically generate LOs for the probe and conjugate by shaping the probe beam using a spatial light modulator (SLM) to shape the spatial profile of a coherent state at the probe frequency. We then use this beam to seed a second 4WM process (Fig. 2). This technique [23] ensures that only the spatial modes supported by the process will be present in the LOs and that any mode distortions due to Kerr lensing [20] will be accounted for as the beams propagate to the far field. Additionally, the use of a second 4WM process guarantees that the spatial profiles of the probe and conjugate LOs are manipulated synchronously so that only correlated regions of the probe and conjugate fields are detected as the shapes of the LOs are manipulated. Without any mask present, we align the LOs to the twin fields in order to maximize the squeezing. The mask is then inserted into the conjugate field, and we begin the search for the mask's shape by manipulating the transverse profile of the LOs.

We calibrated the LO-mask overlap by splitting the seed beam used to generate the LOs and sending it to seed the 4WM process formerly used to generate the vacuum-squeezed twin beams, so that bright twin beams are obtained in their place. These bright twin beams can then be interfered with their LOs in order to optimize mode matching and ensure proper initial alignment for the homodyne detection. As we rotated the angular orientation of the bow tie shapes on the SLM, we observed that the homodyne mode-matching efficiencies between the bright beams and their LOs stayed near 97% for both the probe and conjugate. We then inserted the mask into the bright seeded conjugate beam and directly detected the fraction of transmitted

#169416 - $15.00 USD Received 25 May 2012; revised 29 Jun 2012; accepted 29 Jun 2012; published 11 Jul 2012
(C) 2012 OSA

power as the angle of the bow tie was changed using the SLM. This procedure allowed us to factor any non-uniformity in the beam's intensity profile into the evaluation of the overlap at any LO orientation.

The noise generated by the homodyne difference signal was detected at 750 kHz using a spectrum analyzer in zero-span mode with a resolution bandwidth of 30 kHz, a video bandwidth of 100 Hz, and a sweep time of 1 s. The detected noise was digitized into 460 points, and the average noise power of these 460 points was taken to be a single quadrature noise measurement. To characterize each measurement's statistical uncertainty, we divided each trace into 46 segments consisting of 10 points each. We adopted this procedure after verifying that clustering the data into 10 point segments maintained statistical independence among tthese segments. The average value of each segment was tabulated, and the standard deviation of these 46 values was calculated to characterize the measurement's statistical uncertainty. Finally, 10 series of measurements were taken at 15 different local oscillator bow tie angles for both the quantum and classical noise imaging techniques. This data is presented for the classical and quantum techniques in Fig. 3(a). Since each series of measurements was separated by approximately 20 minutes, the data in Fig. 3(a) indicates an experimental stability over several hours.

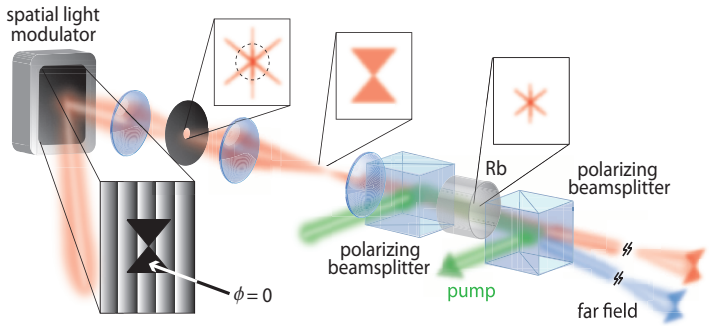

Fig. 2. A spatial light modulator writes a diffraction grating with a region of constant phase in the desired transverse shape of the local oscillator. A coherent state is scattered from the diffraction grating and an f-f optical system and telescope focus the Fourier transform of the pattern into a Rb cell where 4WM occurs, generating two local oscillators at the appropriate frequencies and desired shape in the far field.

We first consider the quantum noise imaging technique (blue triangles in Fig. 3). If the conjugate LO does not spatially overlap with the conjugate field that passes through the mask its measured fluctuations will be near the SNL. On the other hand, since the probe field passes unobstructed to its homodyne detector, its homodyne detection will produce excess noise. Therefore the homodyne difference signal will yield a net excess noise relative to the twin beam SNL. As the overlap between the conjugate and its LO increases, however, the quantum correlations between the twin beams are recovered. Assuming that the noise properties are identical for all the coherence areas, the search for the mask's shape is complete when the amount of squeezing is maximized for the largest LO area possible.

The classical noise imaging technique is implemented by simply blocking the probe beam (red squares in Fig. 3). The only difference is that the conjugate beam, taken alone, is a thermal state with excess noise. In this case, the search for the shape of the mask consists of maximizing the excess noise by manipulating the LO.

#169416 - $15.00 USD Received 25 May 2012; revised 29 Jun 2012; accepted 29 Jun 2012; published 11 Jul 2012
(C) 2012 OSA

4. Results

We wish to quantify the relative sensitivity between the quantum and classical noise imaging techniques in detecting changes in the LO-mask overlap for different overlaps. To do this we introduce the relative uncertainty in the overlap estimation ΔO_{est}:

$$\Delta O_{est} = \frac{\Delta N}{|\frac{\partial N}{\partial O}|}. \tag{1}$$

ΔN represents the measured standard deviation of a given noise power N and $\frac{\partial N}{\partial O}$ is the slope of the noise power as a function of the overlap. In other words, ΔN quantifies the "noise on the noise," which incorporates both sources of statistical uncertainty and technical noise. $\frac{\partial N}{\partial O}$ is set by both the spatial mode composition of the light illuminating the mask as well as the mask's shape [14]. To estimate $\frac{\partial N}{\partial O}$, we computed a linear fit to the noise data at overlaps greater than 0.8 and extrapolated to an overlap of unity. We then included this extrapolated point in a 3rd order polynomial fit and plotted the result in Fig. 3(a). Fig. 3(a) confirms that for overlaps near unity the excess noise and squeezing are maximized for the classical and quantum techniques, respectively.

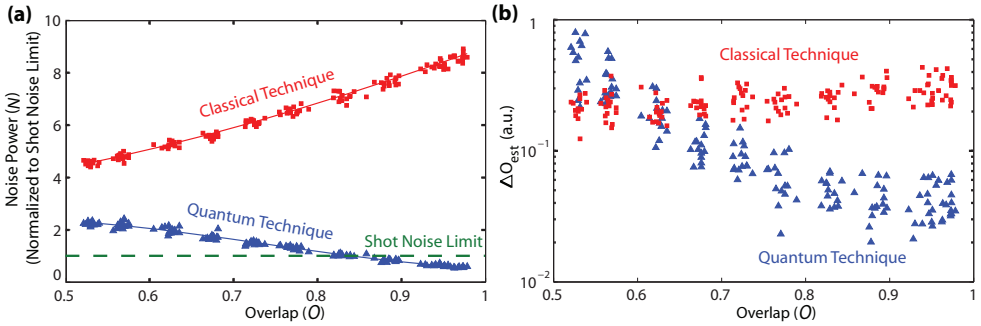

Fig. 3. (a) Mean quadrature noise power N for the conjugate's excess noise (red squares) and twin beam difference signal (blue triangles) as a function of overlap between the mask and the conjugate LO. Standard deviations of the mean are on the order of the marker size and not illustrated. Third order polynomial fits to the data are included. (b) Comparison of the uncertainty in the estimated LO-mask overlap for the classical and quantum techniques, on a log scale, as a function of the overlap for the single and twin beam measurements.

In Fig. 3(b), we present curves comparing ΔO_{est} for the classical and quantum schemes. As Fig. 3(b) suggests, the quantum noise imaging technique provides a higher sensitivity to changes in the overlap than the classical technique. Although the comparable magnitudes of $|\frac{\partial N}{\partial O}|$ indicated in Fig. 3(a) might suggest that the quantum and classical cases should exhibit comparable values for ΔO_{est}, the difference between the curves in Fig. 3(b) can be explained by the variation of ΔN with overlap. Specifically, the value of ΔN is expected to scale with the noise power N. For a given overlap the magnitudes of $|\frac{\partial N}{\partial O}|$ are similar for each technique, but the smaller value of ΔN for the quantum technique will yield a smaller value of ΔO_{est}.

#169416 - $15.00 USD Received 25 May 2012; revised 29 Jun 2012; accepted 29 Jun 2012; published 11 Jul 2012
(C) 2012 OSA

Since the objective of these techniques is to estimate the shape of the mask, we wish to operate in the regime where the overlap is close to unity. For overlaps of 0.9 and above, the quantum case provides an enhancement over the classical case by a factor of 6.3 ± 0.4, corresponding to enhancement in the estimation of the angle by a factor of 3.8 for small angles. The enhancement factor of 6.3 was calculated by averaging ΔO_{est} for overlaps above 0.9 in Fig. 3(b) for the quantum and classical techniques. The angular enhancement factor of 3.8 was obtained by separately calibrating the measured LO-mask overlap as a function of the angle between the LO bow tie and the mask. The indicated uncertainties here and in the figures represent one standard deviation, combined statistical and systematic uncertainties.

We have verified that the classical technique is limited by fluctuations of the conjugate field. On the other hand, we are able to observe excess technical noise introduced by the quantum noise lock used for the measurement of the squeezed noise power for the quantum technique. This leads to a degradation in sensitivity when estimating the angle of the mask. Since this technical noise is not present on the excess noise measurements of the classical technique it decreases the enhancement provided by quantum noise imaging technique over the classical technique. Accordingly, even larger enhancements should be possible. The advantage that can be obtained with the quantum technique over the single-beam classical technique is dependent on the amount of squeezing present [14]. Losses after the twin beam source will erode this advantage depending on how they are distributed between the probe and conjugate. In particular, unbalanced losses between the beams would alter the sensitivity and could eliminate any advantage.

5. "Alphabet gun" test

While we have shown that the quantum noise imaging technique can improve the sensitivity in determining the maximum LO-mask overlap, we also show that this technique can be used with a simple search algorithm to recognize a mask among a given set of choices. We place a mask cut into the shape of the letter Z into the path of the conjugate field and then shape the probe and conjugate LOs with the SLM to form the various letters of the Latin alphabet (Fig. 4(a)). All letters are positioned such that their glyph widths exactly overlap (Fig. 5). Each letter essentially functions as a guess for the shape of the mask. With no mask inserted into the path of the conjugate beam, each choice of LO letter yields slightly different levels of detected single beam excess noise and twin beam squeezing due to the spatial mode structure of the twin beams. These noise levels serve as baselines for comparison when the mask is inserted. We then look at the deviation from these baselines upon insertion of the mask:

$$D^i = \frac{N^i_{masked}}{N^i_{baseline}}. \tag{2}$$

D^i denotes the deviation in the noise power for LO letter i, N^i_{masked} is the noise power recorded by the homodyne detection with the mask present, and $N^i_{baseline}$ signifies the unmasked baseline noise power.

For the classical technique, the presence of the mask leads to varying degrees of reduction in the measured excess noise (Fig. 4(b)). For the quantum technique, the mask causes the measured quadrature-difference noise to increase and, for most choices of LO letter, for the squeezing to be lost. In fact, only the correct choice of the LO letter (Z) continued to yield any squeezing. It should be noted that the letter I in the chosen font did not produce a strong enough LO to elevate the single beam shot noise significantly above the electronic noise floor, so it is not included in Fig. 4(b)-(c).

Although both the classical and quantum estimation techniques correctly suggest that the letter Z is the best choice of LO, the quantum technique provides a higher degree of confidence.

#169416 - $15.00 USD Received 25 May 2012; revised 29 Jun 2012; accepted 29 Jun 2012; published 11 Jul 2012
(C) 2012 OSA

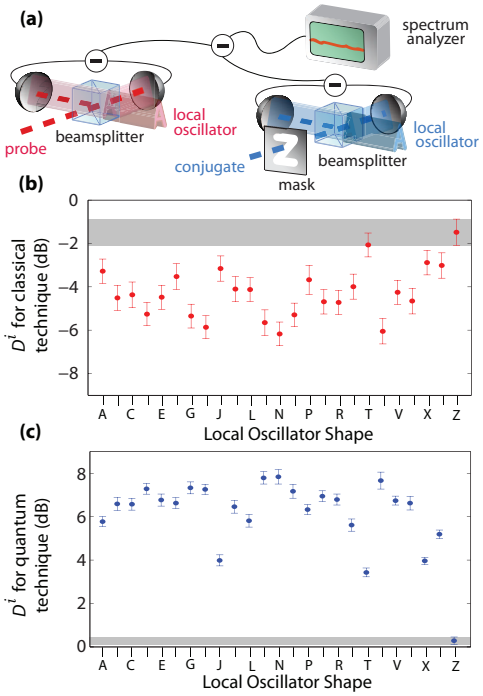

Fig. 4. (a) Probe and conjugate LOs are generated in the shape of each letter of the alphabet and used in a balanced homodyne detection. The conjugate field illuminates the mask whose shape is to be estimated. (b) Deviation from initial excess noise for the classical noise imaging technique upon insertion of the mask versus choice of letter for the local oscillator. (c) Deviation from initial squeezing level for the quantum noise imaging technique upon insertion of the mask. The baseline of squeezing between the twin beams for the LO letter Z is -2.2 dB, measured without the mask. With the mask inserted, only the mask shaped as the letter Z maintains any squeezing. The gray regions in (b)-(c) represent the value of D^i and its associated uncertainty for the correct LO choice, Z. The letter "I" in the chosen font did not produce a bright enough local oscillator to elevate the quadrature noise power above the electronic noise floor of our detectors.

Fig. 5. Local oscillators used for the alphabet gun test (Media 1).

#169416 - $15.00 USD Received 25 May 2012; revised 29 Jun 2012; accepted 29 Jun 2012; published 11 Jul 2012
(C) 2012 OSA

Uncertainties in the deviation incorporate contributions from both the baseline and masked noise measurements. These uncertainties are plotted along with their associated changes in squeezing and excess noise in Fig. 4. For the quantum case (Fig. 4(c)), the correct choice of LO is separated from the next closest choice (the letter T) by over 7 standard deviations. For the classical case, however, the quadrature noises for the letters T and Z lie within their respective uncertainties.

6. Conclusion

In conclusion, we have demonstrated the ability to estimate the shape of a binary intensity mask using homodyne detection of the noise of vacuum-squeezed twin beams used to illuminate the object. In the classical and quantum techniques described, the mask is exposed to exactly the same state of light, which contains too few photons for direct detection of the amplitude quadrature and too many photons for current photon counters. These techniques might therefore prove useful for imaging applications where a minimal exposure to light is critical (e.g. when dealing with low optical damage thresholds or when it is desirable that the detection go unnoticed). A promising application is related to imaging of biological samples under controlled conditions where squeezing could be maintained and the exposure of the sample minimized [24].

The classical noise imaging technique exploits the fact that, taken individually, each of the twin beams behaves like a thermal state of a light characterized by uniform excess quadrature noise. Although the excess noise properties of a single beam can be used, we have demonstrated that the quantum correlations of the twin beams offer an enhancement in sensitivity for the regime of high LO-mask overlap. As explained in [14], these correlations must be quantum for an enhancement to be possible. Additionally, we showed that a mask can be recognized among a given alphabet of choices with increased confidence using the quantum noise imaging technique. As one can notice in the associated video, the resolution with which we generate the LOs is limited. The constraint on the resolution is the limited pump power available for the 4WM process, which places a practical upper bound on the pump's available transverse size. Increasing the pump's transverse size at a given intensity would increase the resolution of the LOs [11] and should improve our ability to estimate the shape of the mask.

Finally, we note that one could in principle identify a phase mask separate from, or in addition to, an intensity mask with a similar technique. The search for a phase mask would require a scan over the LO phase in only the beam that passes through the mask. Such a search would not be possible, however, using the "classical technique" since for a thermal beam all phases have the same noise level.

#169416 - $15.00 USD Received 25 May 2012; revised 29 Jun 2012; accepted 29 Jun 2012; published 11 Jul 2012
(C) 2012 OSA

3.2 How quantum noise affects the propagation of information.

We have already discussed various approaches to delay light and quantum information carried by entanglement. Although entanglement cannot be used to signal superluminally [50], it is thought to be an essential resource in quantum information science [51, 52]. It is then of fundamental interest to study what happens to entanglement when part of an entangled system propagates through a fast light medium. Much work has been done to understand fast-light phenomena associated with anomalous dispersion, which gave rise to group velocities that are greater than the speed of light in vacuum, as described in chapter 1 [53]. For classical pulses propagating without the presence of noise, it has been well established theoretically that the "pulse front" propagates through a linear, causal medium at the speed of light in vacuum [54]. It is often argued that this part of the pulse carries the entirety of the pulse's classical information content since the remainder of the signal can in principle be inferred by measuring the pulse height and its derivatives, just after the point of non-analyticity has passed [55, 56]. Experimentally, in the inevitable presence of quantum noise, pulse fronts may not convey the full story of what is readily observed in the laboratory.
In the paper *Quantum mutual information of an entangled state propagating through a fast-light medium*, we discuss in details the detrimental role of quantum noise. Instead of using a pulse with a given shape, in this work we encode the information in correlated quantum noise, and therefore the definition of a "pulse front" becomes impossible. The fluctuations of the probe and conjugate electric fields are not externally imposed, and they present no obvious pulse fronts or non-analytic features to point to as defining the signal velocity. As such, classically-rooted approaches to defining the signal or information content of the individual modes are not readily applicable to this system. To quantify the quantity of information usable in the entangled beams we use the criteria of inseparability (Fig. 3.2 for details). As a reminder, note that an inseparability lower than 2 guarantees the presence of entanglement.

The entangled beams are generated using four-wave-mixing in a hot atomic vapor, and one of the two beams then propagates through a tunable fast-light medium (with group velocity larger than c). This fast light medium can be tuned to slow-light by changing the experimental parameters and this allows for direct comparison. Due to the Kramers-Kronig relation, a group velocity larger than c, is systematically associated with gain or loss through the medium. The main point of our study is to understand the role of this gain or loss on the quantum information encoded in our beams.

The first step consists in measuring the arrival time of the cross-correlation maximum (or minimum) when the conjugate beam propagates in vacuum (actually in air) and compare it to the case of propagation in a fast-light medium. This approach is analogous to the classical technique of measuring the arrival time of a light pulse maximum. After accumulating enough statistics, we have observed an advancement of the normalized correlation peak by 3.7 ns $\pm$ 0.1 ns. Compared to the 300 ns of correlation time, this corresponds to a un-ambiguous relative advancement of more than 1%.

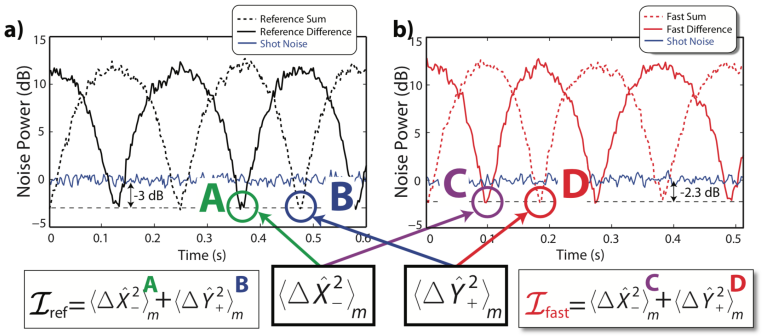

Figure 3.2: Determination of inseparability $\mathcal{I}$ using a spectrum analyzer. Part a) corresponds to the reference case while b) corresponds to data taken with fast light. The minimum noise power of the homodyne difference signal corresponds to squeezing of the $\hat{X}$ quadrature difference (i.e. $\langle \hat{X}_-^2 \rangle$) while the minimum noise power of the homodyne sum gives the squeezing of phase sum $\langle \hat{Y}_+^2 \rangle$. With the fast-light cell inserted into the path of the conjugate, we were able to see $\mathcal{I} < 2$. The figure shows how the inseparability can be calculated (from the data obtained from the spectrum analyzers) by adding together the values of the appropriate minima and averaging. Adapted from [26]

However this advancement is coming with a reduction of the quadrature squeezing from -3 dB below the shot noise in the case of free-space to -2.3 dB in the case of fast-light media (Fig. 3.2). Obviously this reduction is not observed when comparing the cross-correlation maximum or normalized. Therefore, in a second set of measurements, we report the inseparability as function of time. Similarly we see an advancement of the inseparability peak in the case of the fast-light medium. This was expected as the inseparability is computed from normalized cross-correlation maximum and minimum (see figure 3.2 for details).

More insights can be found in the behaviour of the leading edge of inseparability. Indeed, the inseparability can be used to define the mutual information (using the covariance matrix) and therefore, a larger value of inseparability means more mutual information shared between the two sides of the entangled pair. If at some moment in time, the inseparability has a larger value than later it means that the amount of information is larger. What we observe in the experiment is that the noise added by the fast light medium, consistently reduces the value of inseparability of the leading edge in order that it never outperforms the case of free-space. In the opposite case of slow light, we also have shown clear evidence of delaying not only the maximum of inseparability but also the trailing edge.

It is interesting to contrast this asymmetry in the fast- and slow-light behaviour of the mutual information with the results of previous experiments studying the velocity of classical information propagating through dispersive media. In refs [55] and [57], new information associated with a 'non-analytic' point in the field was found to propagate at c in the presence of slow- and fast-light media alike.

nature photonics

LETTERS

PUBLISHED ONLINE: 25 MAY 2014 | DOI: 10.1038/NPHOTON.2014.112

Quantum mutual information of an entangled state propagating through a fast-light medium

Jeremy B. Clark[1], Ryan T. Glasser[1], Quentin Glorieux[1,2], Ulrich Vogl[3], Tian Li[1], Kevin M. Jones[4] and Paul D. Lett[1]*

It is widely accepted that information cannot travel faster than *c*, the speed of light in vacuum[1–3]. Here, we investigate the behaviour of quantum correlations and information in the presence of dispersion. To do so we send one half of an entangled state of light through a gain-assisted slow- or fast-light medium and detect the transmitted quantum correlations and quantum mutual information[4–6]. We show that quantum correlations can be advanced by a small fraction of the correlation time, even in the presence of noise added by phase-insensitive gain. Additionally, although the peak of the quantum mutual information between the modes can be advanced, we find that the degradation of the mutual information due to added noise appears to prevent an advancement of the leading edge. In contrast, we demonstrate a significant delay of both the leading and trailing edges of the mutual information in a slow-light system.

Many experiments have demonstrated the ability to manipulate the group velocities of optical pulses moving through atomic vapours[7–11]. For classical pulses propagating without the presence of noise, it has been well established theoretically[12,13] that the initial turn-on point of a pulse (the 'pulse front') propagates through a linear causal medium at the speed of light in vacuum. It is often argued[14] that this signal carries the entirety of the pulse's classical information content, because the remainder of the pulse can in principle be inferred from the pulse height and its derivatives just after the point of non-analyticity has passed.

Experimentally, particularly in the inevitable presence of quantum noise, pulse fronts may not convey the full story of what is readily observed in the laboratory. It is thus interesting to consider other operational definitions of a signal that apply to particular systems. For example, Stenner and colleagues[15] studied the propagation of classical information encoded in bright, actively shaped optical pulses travelling through a fast-light medium. These experiments revealed that the operational information velocity is actually slowed to speeds less than *c*. Although noise may have affected the experimental results, these experiments were not conducted in a regime where quantum noise necessarily played a crucial role. Meanwhile, adopting a definition of signal velocity based on observing a given signal-to-noise ratio, Kuzmich and colleagues showed how quantum noise associated with gain-assisted fast light would be expected to limit the early detection of smooth, narrowband pulses consisting of only a few photons[16].

Here, we adopt an alternative definition of a signal, choosing it to be the random, but strongly correlated quantum fluctuations of two spatially separated parts of a bipartite entangled state. The entangled state in this experiment was generated via four-wave mixing (4WM) in a warm vapour of ^{85}Rb (ref. 17), which converts two photons from a strong pump beam into 'twin' photons emitted into spatially separated modes referred to as the probe and the conjugate (Fig. 1a). Although entanglement cannot be used to signal superluminally[18], it is thought to be an essential resource in quantum information science[5,6]. Accordingly, the prospect of storing[19] or delaying[20] entanglement has attracted significant interest.

The fluctuations of the probe and conjugate fields are not externally imposed and they present no obvious pulse fronts or non-analytic features to point to as defining the signal velocity. As such, classically rooted approaches to defining the signal or information content of the individual modes are not readily applicable to this system. Despite the randomness of these fluctuations, information is shared between the modes. We take the quantum mutual information as our information measure, which removes the ambiguity of defining the arrival time of such information in the presence of noise, quantum or otherwise. The quantum mutual information for bipartite Gaussian states is readily accessible via optical homodyne measurements[5,6] and naturally provides a consistent description of information in this system.

We studied how the dispersion associated with phase-insensitive gain[3] affects these correlations by inserting a second vapour cell into the path of the conjugate and driving a second 4WM process with a separate pump (Fig. 1b). We show that when one mode of the two-mode state passes through this fast-light medium, the peak of the quantum mutual information between the modes is advanced, but the arrival of the leading edge is not. We also show that—in contrast—the leading and trailing edges of the mutual information are both delayed when one of the modes propagates through a gain-assisted slow-light medium.

The real and imaginary parts of the nonlinear susceptibility $\chi^{(3)}$ that govern the response of the second 4WM process to the conjugate can be described by a set of equations similar to the Kramers–Kronig relations applicable to linear dielectric media[21]. Using these relations as a guide (Fig. 1c), we changed the detuning of the pump beam used to drive the second 4WM process so that the conjugate frequency overlapped with the region of anomalous dispersion.

By performing separate balanced homodyne detections of the probe and conjugate modes, we measured the fluctuations of the in-phase $(\hat{X})$ and out-of-phase $(\hat{Y})$ amplitudes of the electromagnetic field in each beam, which are referred to as the field quadratures. Taken individually, the probe and conjugate beams exhibit quadrature fluctuations that exceed the shot-noise limit. Taken together, however, these fluctuations display strong correlations beyond the limits achievable classically. To characterize the strength of the correlations, it is helpful to introduce the joint quadrature operators $\hat{X}_- = (\hat{X}_p - \hat{X}_c)/\sqrt{2}$ and $\hat{Y}_+ = (\hat{Y}_p + \hat{Y}_c)/\sqrt{2}$, where

[1]Quantum Measurement Division, National Institute of Standards and Technology and Joint Quantum Institute, NIST & the University of Maryland, Gaithersburg, Maryland 20899, USA, [2]Laboratoire Kastler Brossel, Université Pierre et Marie Curie, Ecole Normale Supérieure and CNRS, UPMC Case 74, 4 place Jussieu, 75252 Paris Cedex 05, France, [3]Max Planck Institute for the Science of Light, Günther-Scharowsky-Strasse 1, Building 24, 91058 Erlangen, Germany, [4]Physics Department, Williams College, Williamstown, Massachusetts 01267, USA. *e-mail: paul.lett@nist.gov

© 2014 Macmillan Publishers Limited. All rights reserved.

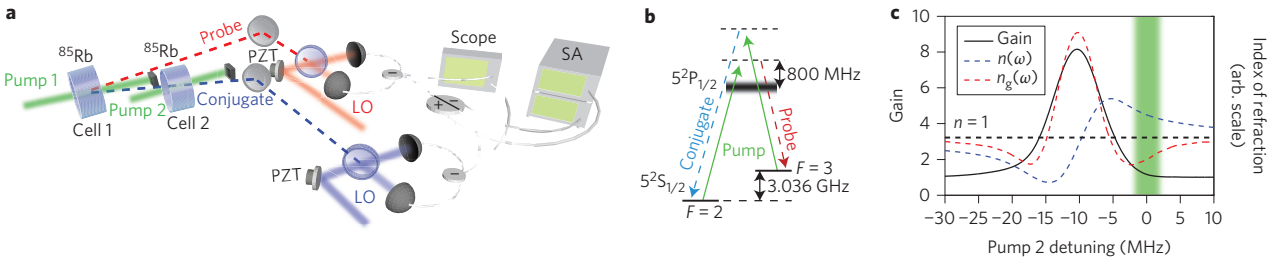

Figure 1 | Experimental set-up. a,**b**, Vacuum-squeezed twin beams are generated in cell 1 using 4WM in a double-lambda configuration (**b**). A region of anomalous dispersion for the conjugate is created in a second vapour cell using a second 4WM process driven by pump 2, whose frequency is independently tunable with respect to pump 1 (Supplementary Section 1). The phase of the local oscillators (LOs) is scanned using piezo-electric transducers (PZTs) to verify the presence of entanglement. The sum and difference signals of the homodyne detections are recorded on a pair of spectrum analysers (SAs) to detect quantum correlations. An oscilloscope is triggered to detect time traces of the individual homodyne detectors given a predetermined threshold of squeezing heralded by the SAs. **c**, Measured gain profile (black solid line) of the second 4WM process as a function of the detuning of pump 2 relative to pump 1. From the gain profile, we numerically compute the associated refractive index $n(\omega)$ and group index n_g. In determining the advancement, we confine our attention to fluctuations in the frequency band (shaded green) where we observe quantum correlations generated in cell 1. We tune the second pump frequency so that the bandwidth of anomalous dispersion coincides with the bandwidth where we observe quantum correlations.

subscripts p and c denote the probe and conjugate fields, respectively. For the appropriate choice of local oscillator phases[17], the fluctuations of one of the joint quadratures ($\langle \Delta \hat{X}_-^2 \rangle$ or $\langle \Delta \hat{Y}_+^2 \rangle$) fall below the shot-noise limit (are 'squeezed').

We verified the presence of entanglement by calculating a related quantity, the inseparability $\mathcal{I}$:

$$\mathcal{I} \equiv \langle \Delta \hat{X}_-^2 \rangle_{\mathrm{m}} + \langle \Delta \hat{Y}_+^2 \rangle_{\mathrm{m}} \qquad (1)$$

Here $\langle \Delta \hat{X}_-^2 \rangle_{\mathrm{m}}$ is the minimum value of the difference signal, $\langle \Delta \hat{Y}_+^2 \rangle_{\mathrm{m}}$ is the minimum value of the sum, and each term is normalized to the shot-noise limit. An inseparability of $\mathcal{I} < 2$ is a necessary and sufficient condition to conclude that any bipartite Gaussian state is entangled[22].

Studies of bright beam propagation through fast-light media[23] have investigated the trade-off between the magnitude of the advancement and the amount of added noise[24,25] as a function of detuning. Here, we choose a detuning of the second pump that produces a readily detectable advancement of the conjugate fluctuations without significantly deteriorating the inseparability. By operating in a regime of low gain ($G \approx 1.1$), we maintained an inseparability of $\mathcal{I} = 1.2$ under fast-light conditions, confirming the persistence of entanglement between the probe and conjugate after the conjugate passes through the fast-light medium (Fig. 2a,b).

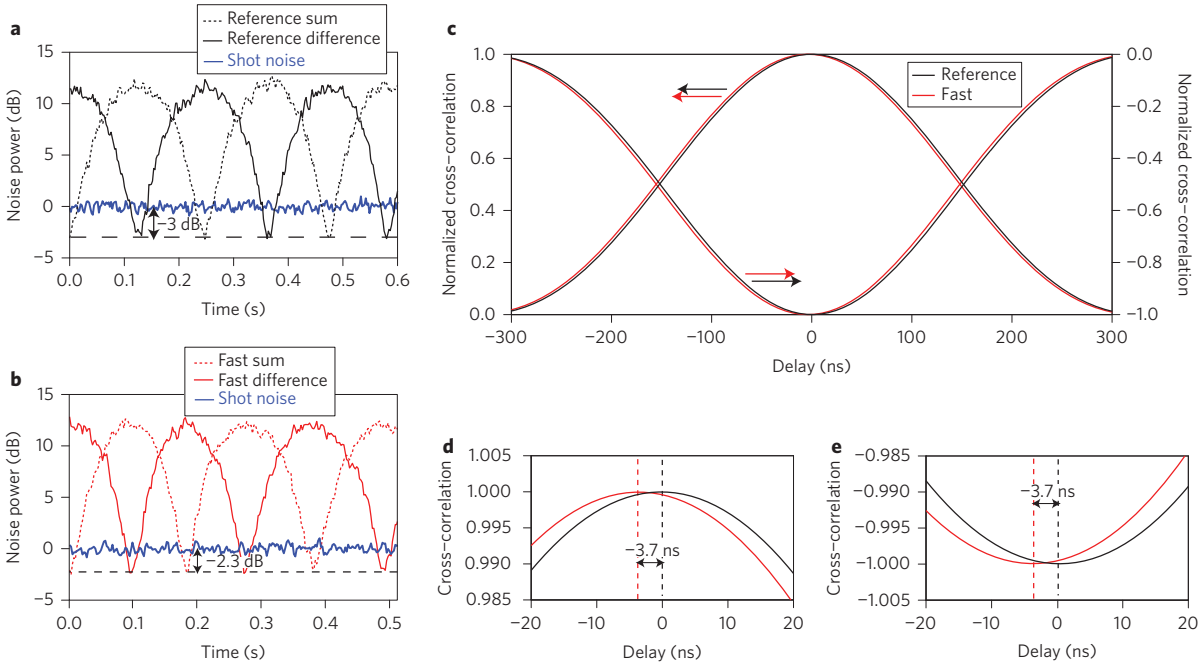

Figure 2 | Persistence of correlations associated with entanglement in the presence of anomalous dispersion. a, We observe up to −3 dB of squeezing with an associated inseparability $\mathcal{I} \approx 1$ when the second (fast-light) 4WM process is suppressed. **b**, In the presence of a small phase-insensitive gain giving rise to anomalous dispersion, the squeezing reduces to −2.3 dB and $\mathcal{I}$ increases to 1.2, which is still sufficient to show entanglement ($\mathcal{I} < 2$). **c**, Average normalized cross-correlation functions for the correlated and anti-correlated joint quadratures. The left axis applies to the reference and advanced curves for the correlated quadratures, and the right axis applies to the anti-correlated quadratures (indicated by arrows). When calculating the cross-correlation functions, the reference and fast-light data are both subject to the same passband filter used to calculate $\mathcal{I}$ (Supplementary Sections 3.1 and 3.2). **d**,**e**, Closer looks at the peak correlation (**d**) and anti-correlations (**e**) portrayed in **c**.

© 2014 Macmillan Publishers Limited. All rights reserved.

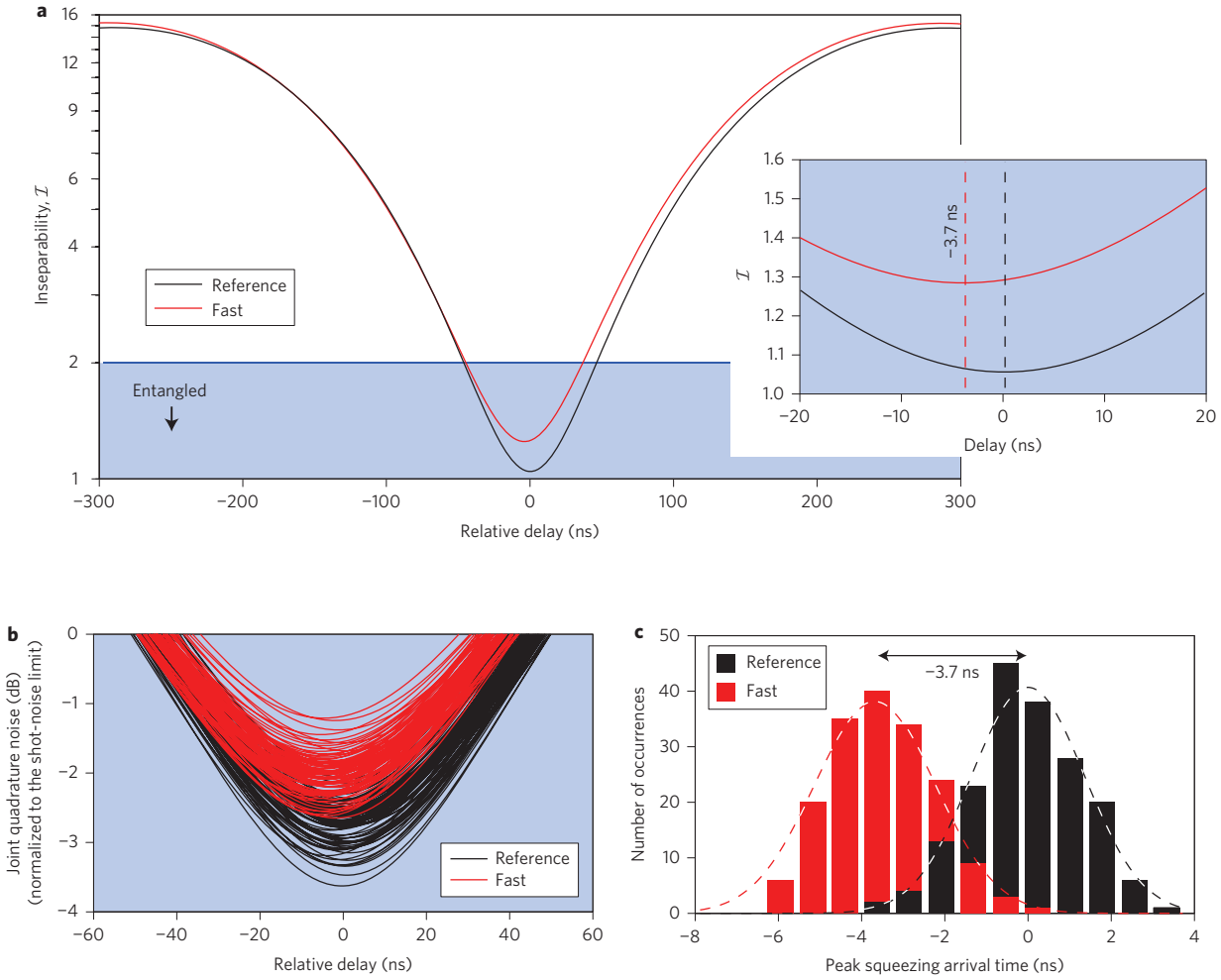

Figure 3 | Observed advance in the quantum correlations. a, Average advance and accompanying degradation of the inseparability, $\mathcal{I}$ ($\mathcal{I} < 2$ implies entanglement), in the presence of anomalous dispersion (fast, red curves) and upon blocking the second pump (reference, black curves). The subpanel provides a closer look at the minima of the inseparability curves. **b**, Sampling of the squeezing versus delay over 200 experimental iterations used to compute the average $\mathcal{I}$. **c**, Histogram of the sampled minima of the joint quadrature noise (that is, maximum squeezing) versus the relative probe–conjugate delay. From the sampled shots we extract an advance of 3.7 ± 0.1 ns, where the uncertainty has been estimated by computing the standard deviation of the mean.

We confirm that the fluctuations of the continuous-wave (c.w.) conjugate are advanced through the fast-light cell by computing the normalized cross-correlation function (see Methods and Supplementary Section 3.1) of the detected probe and conjugate quadratures for both the reference and fast-light cases (Fig. 2c–e). After averaging 200 time traces, we conclude that the peak of the cross-correlation function is shifted forward in time by 3.7 ± 0.1 ns, corresponding to a fractional advance of ∼1% relative to the cross-correlation width (∼300 ns). Here, the uncertainty is estimated by taking the standard deviation of the mean for the cross-correlation peak advancements over all the experiments.

Although useful to clearly see an advancement of the correlations, the normalized cross-correlation function of the field quadratures does not capture how the noise added through phase-insensitive gain affects the entanglement. We therefore plot the inseparability $\mathcal{I}$ as a function of the relative delay (Fig. 3a). The delay is implemented in software in exactly the same manner as when calculating the cross-correlation function. Although the minimum value of $\mathcal{I}$ is advanced in time for the fast-light case, its degradation acts, within experimental uncertainty, to prevent the leading edge from advancing forward in time. Figure 3b presents a sampling of the delay-dependent squeezing measurements used to calculate the inseparability, which indicates an advance in the maximum squeezing of 3.7 ± 0.1 ns (Fig. 3c).

In our experiment there is no imposed 'signal' as such. However, the fluctuations on one beam carry information about the fluctuations on the other. We capture this by calculating the quantum mutual information between the two beams (Fig. 4), working from the same basic data as used to calculate the delay-dependent inseparability. The mutual information $I(\rho)$ is defined in terms of the von Neumann entropy $S_V(\rho) = -\mathrm{Tr}(\rho \log \rho)$ according to

$$I(\rho) = S_V(\rho_1) + S_V(\rho_2) - S_V(\rho) \qquad (2)$$

where ρ denotes the full state density matrix and $\{\rho_1, \rho_2\}$ denote the reduced density matrices of the subsystems. The mutual information quantifies the total (classical plus quantum) correlations between the probe and conjugate[26]. In good agreement with the squeezing and cross-correlation measurements, we observe an advancement of 3.7 ± 0.1 ns of the peak of the delay-dependent mutual information, paired with a degradation due to uncorrelated noise added by the fast-light cell (Supplementary Section 5). This degradation appears to prevent us from observing an

© 2014 Macmillan Publishers Limited. All rights reserved.

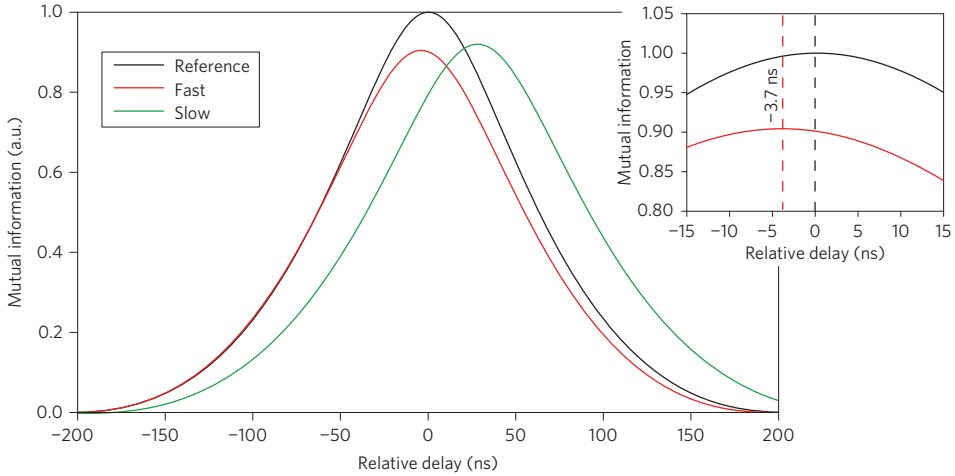

Figure 4 | Comparison of computed quantum mutual information between the c.w. probe and conjugate as a function of relative delay for fast and slow light. The smooth shape of the curves results from the large amount of data (180 files consisting of 1×10^7 points per file) used to calculate the mutual information. When considering fast-light advancement of the conjugate (red trace), we observe an advance in the peak of the mutual information of 3.7 ± 0.1 ns. The subpanel provides a closer look at the maxima of the mutual information curves for the reference and fast-light cases. There is no statistically significant advance of the leading edge of the mutual information in the case of fast-light propagation. Repeating the same analysis for slow-light propagation of the probe we observe significant delays of both the leading and trailing edges of the mutual information (green trace).

advance of the leading edge of the fast-light mutual information (red curve in Fig. 4).

We then tuned the temperature and the pump detuning of the second 4WM process to delay the propagation of the probe, as in ref. 20. We slowed the probe to the greatest extent possible while limiting the degradation of the inseparability to the same level as in the fast-light case. The behaviour of the mutual information after a slow-light delay is plotted alongside the reference and fast-light cases in Fig. 4 (green trace). We are able to observe significant delays of the leading and trailing edges of the mutual information when compared to the reference case.

It is interesting to contrast this asymmetry in the fast- and slow-light behaviour of the mutual information with the results of previous experiments studying the velocity of classical information propagating through dispersive media. In refs 15 and 27, new information associated with a 'non-analytic' point in the field was found to propagate at c in the presence of slow- and fast-light media alike. This behaviour can be understood to be a consequence of the field's frequency components that lie outside the relevant bandwidth where the medium exhibits steep dispersion.

Our results highlight the role played by both the detection and information encoding methods in such experiments. In the present experiments the signal beam is not pulsed, so there is no externally imposed non-analytic point. The individual probe and conjugate beams are noisy c.w. squeezed-vacuum beams, carrying information that is correlated and common to the two beams. Our experiments clearly show that the arrival time of the mutual information contained within the detection bandwidth is affected by the fast- and slow-light media. Although the normalized correlation function, the peak of the inseparability and the peak of the mutual information can all be advanced, our results suggest that the leading edge of the mutual information cannot be advanced beyond the reference situation. Further work will be required to determine if this is a fundamental limit in this measurement context. The experiment clearly shows that the mutual information can be delayed. We speculate that a combination of distortion effects and quantum noise added by phase-insensitive gain act to limit the advance of the mutual information differently from the delay. We hope that these experimental observations stimulate a sharpening of our understanding of the role of quantum noise in limiting the transport of information.

Methods

Data acquisition and frequency filtering. The local oscillator phases were allowed to drift and the oscilloscope was triggered to record time traces of each individual homodyne detection when the phases were appropriate to observe the squeezing in either joint quadrature (Supplementary Section 2). The traces were Fourier-transformed for analysis, and all analysis was confined to power spectral densities within a bandwidth of 100 kHz–2 MHz. This corresponds to the frequency bandwidth where we were able to show entanglement ($\mathcal{I} < 2$) without the presence of dispersion.

Calculating the correlation measures. We evaluated the inseparability over the same 100 kHz–2 MHz bandwidth for all reference, fast- and slow-light experiments. To calculate the mutual information, we made use of the fact that any bipartite Gaussian state can be completely characterized by the variances and covariances of the field quadratures[28,29]. These variances and covariances were evaluated using the same bandwidth used to compute the inseparability. Finally, we evaluated the cross-correlation functions after filtering the probe and conjugate homodyne time traces with a 100 kHz–2 MHz band-pass filter (Supplementary Section 3.1).

Received 19 September 2013; accepted 18 April 2014; published online 25 May 2014

References

1. Garrison, J. C., Mitchell, M. W., Chiao, R. Y. & Bolda, E. L. Superluminal signals: causal loop paradoxes revisited. *Phys. Lett. A* **245,** 19–25 (1998).
2. Milonni, P. W. *Fast Light, Slow Light and Left-handed Light* (Taylor & Francis, 2010).
3. Boyd, R. W. Slow and fast light: fundamentals and applications. *J. Mod. Opt.* **56,** 1908–1915 (2009).
4. Nielsen, M. A. & Chuang, I. L. *Quantum Computation and Quantum Information* (Cambridge Univ. Press, 2000).
5. Braunstein, S. L. & van Loock, P. Quantum information with continuous variables. *Rev. Mod. Phys.* **77,** 513–577 (2005).
6. Weedbrook, C. *et al.* Gaussian quantum information. *Rev. Mod. Phys.* **84,** 621–669 (2012).
7. Glasser, R. T., Vogl, U. & Lett, P. D. Stimulated generation of superluminal light pulses via four-wave mixing. *Phys. Rev. Lett.* **108,** 173902 (2012).
8. Camacho, R. M., Pack, M. V., Howell, J. C., Schweinsberg, A. & Boyd, R. W. Wide-bandwidth, tunable, multiple-pulse-width optical delays using slow light in cesium vapor. *Phys. Rev. Lett.* **98,** 153601 (2007).
9. Hau, L. V., Harris, S. E., Dutton, Z. & Behroozi, C. H. Light speed reduction to 17 metres per second in an ultracold atomic gas. *Nature* **397,** 594–598 (1999).
10. Glasser, R. T., Vogl, U. & Lett, P. D. Demonstration of images with negative group velocities. *Opt. Express* **20,** 13702–13710 (2012).
11. Keaveney, J., Hughes, I. G., Sargsyan, A., Sarkisyan, D. & Adams, C. S. Maximal refraction and superluminal propagation in a gaseous nanolayer. *Phys. Rev. Lett.* **109,** 233001 (2012).

© 2014 Macmillan Publishers Limited. All rights reserved.

12. Brillouin, L. Über die Fortpflanzung des Lichtes in dispergierenden Medien. *Ann. Phys. (Leipz.)* **349,** 203–240 (1914).
13. Sommerfeld, A. Ein Einwand gegen die Relativtheorie der Elektrodynamik und seine Beseitigung. *Phys. Zeit.* **8,** 841–842 (1907).
14. Chiao, R. Y. & Steinberg, A. M. in *Progress in Optics* Vol. 37 (ed. Wolf, E.) 345–405 (Elsevier, 1997).
15. Stenner, M. D., Gauthier, D. J. & Neifeld, M. A. The speed of information in a 'fast-light' optical medium. *Nature* **425,** 695–698 (2003).
16. Kuzmich, A., Dogariu, A., Wang, L. J., Milonni, P. W. & Chiao, R. Y. Signal velocity, causality, and quantum noise in superluminal light pulse propagation. *Phys. Rev. Lett.* **86,** 3925–3929 (2001).
17. Boyer, V., Marino, A. M., Pooser, R. C. & Lett, P. D. Entangled images from four-wave mixing. *Science* **321,** 544–547 (2008).
18. Peres, A. & Terno, D. R. Quantum information and relativity theory. *Rev. Mod. Phys.* **76,** 93–123 (2004).
19. Lvovsky, A. I., Sanders, B. C. & Tittel, W. Optical quantum memory. *Nature Photon.* **3,** 706–714 (2009).
20. Marino, A. M., Pooser, R. C., Boyer, V. & Lett, P. D. Tunable delay of Einstein–Podolsky–Rosen entanglement. *Nature* **457,** 859–862 (2009).
21. Hutchings, D. C., Sheik-Bahae, M., Hagan, D. & Stryland, E. Kramers–Krönig relations in nonlinear optics. *Opt. Quantum Electron.* **24,** 1–30 (1992).
22. Duan, L.-M., Giedke, G., Cirac, J. I. & Zoller, P. Inseparability criterion for continuous variable systems. *Phys. Rev. Lett.* **84,** 2722–2725 (2000).
23. Vogl, U. *et al.* Advanced quantum noise correlations. *New J. Phys.* **16,** 013011 (2014).
24. Caves, C. M. Quantum limits on noise in linear amplifiers. *Phys. Rev. D.* **26,** 1817–1839 (1982).
25. Boyd, R. W., Shi, Z. & Milonni, P. W. Noise properties of propagation through slow- and fast-light media. *J. Opt.* **12,** 104007 (2010).
26. Ollivier, H. & Zurek, W. H. Quantum discord: a measure of the quantumness of correlations. *Phys. Rev. Lett.* **88,** 017901 (2001).
27. Stenner, M. D., Gauthier, D. J. & Neifeld, M. A. Fast causal information transmission in a medium with a slow group velocity. *Phys. Rev. Lett.* **94,** 053902 (2005).
28. Serafini, A., Illuminati, F. & De Siena, S. Symplectic invariants, entropic measures and correlations of Gaussian states. *J. Phys. B* **37,** L21–L28 (2004).
29. Vogl, U. *et al.* Experimental characterization of Gaussian quantum discord generated by four-wave mixing. *Phys. Rev. A* **87,** 010101 (2013).

Acknowledgements

This research was supported by the Physics Frontiers Center at the Joint Quantum Institute and the Air Force Office of Scientific Research. Q.G. performed this work with the support of the Marie Curie IOF FP7 Program (Multimem–300632), while U.V. was supported by the Alexander von Humboldt Foundation and R.T.G. was supported by a National Research Council Research Associateship Award at NIST. J.B.C. acknowledges support from the National Science Foundation.

Author contributions

J.B.C., R.T.G., Q.G. and U.V. analysed the data. J.B.C., R.T.G., U.V. and P.D.L. conceived and designed the experiments. J.B.C., R.T.G., Q.G. and U.V. contributed materials and analysis tools. J.B.C., R.T.G., Q.G., U.V. and T.L. performed the experiments. J.B.C., R.T.G., Q.G., U.V., K.M.J. and P.D.L. wrote the paper.

Additional information

Supplementary information is available in the online version of the paper. Reprints and permissions information is available online at www.nature.com/reprints. Correspondence and requests for materials should be addressed to P.D.L.

Competing financial interests

The authors declare no competing financial interests.

© 2014 Macmillan Publishers Limited. All rights reserved.

Chapter 4

Hydrodynamics of light

List of publications related to this chapter :

- **Injection of Orbital Angular Momentum and Storage of Quantized Vortices in Polariton Superfluids.**
  T. Boulier, E. Cancellieri, N. D. Sangouard, **Q. Glorieux**, A. V. Kavokin, D. M. Whittaker, E. Giacobino, and A. Bramati.
  Phys. Rev. Lett. **116**, 116402 (2016)

- **Observation of the Bogoliubov dispersion in a fluid of light**.
  Q. Fontaine, T. Bienaimé, S. Pigeon, E. Giacobino, A. Bramati, **Q. Glorieux**.
  Phys. Rev. Lett., *Accepted* , (2018).

- **Coherent merging of counterpropagating exciton-polariton superfluids.**
  T. Boulier, S. Pigeon, E. Cancellieri, P. Robin, E. Giacobino, **Q. Glorieux** and A. Bramati.
  Phys. Rev. B **98**, 024503 (2018).
  Not included.

- **Lattices of quantized vortices in polariton superfluids.**
  T. Boulier, E. Cancellieri, N. D Sangouard, R. Hivet, **Q. Glorieux**, E. Giacobino, A. Bramati.
  Comptes Rendus Académie des Sciences **17**, 893 (2016).
  Not included.

- **Vortex chain in a resonantly pumped polariton superfluid.**
  T. Boulier, H. Tercas, DD. Solnyshkov, **Q. Glorieux**, E. Giacobino, G. Malpuech, A. Bramati.
  Scientific Reports **5**, 9230 (2015).
  Not included.

4.1 What is a fluid of light ?

We know, since Einstein, that vacuum photons are well described as massless non-interacting particles, behaving as an ideal gas. In this chapter we discuss experiments where photons acquire a sizeable effective mass and tunable interactions mediated by a coupling with matter, forming a **fluid of light.** This approach relies on a description of these hybrid photons in terms of quasi-particle of light generically known as polariton [6].

4.1.1 Hydrodynamic formulation of the non-linear Schrödinger equation

The non-linear Schrödinger equation is used to describe a large variety of phenomena. This equation can be written in a mathematical form, with t and ∇^2 dimensionless:

$$i\frac{\partial A}{\partial t} = \left(-\frac{1}{2}\nabla^2 + g|A|^2\right) A. \tag{4.1}$$

A is an arbitrary quantity and g is the non-linear coupling coefficient.

In this manuscript, we will use this equation (with some modifications) to study the time evolution of excitons polaritons in a microcavity (see 4.2) and the spatial evolution of an electric field propagating in a non-linear medium (see 4.5). In chapter 5, we will also discuss its relevance in slow light and quantum memory experiments.

In the context of fluid of light, it is useful to use the hydrodynamic formulation of the non-linear Schrödinger equation [58, 59, 60]. To show that this approach is very general, I will do this derivation in the case of the Gross-Pitaevskii equation which describes the dynamics of an atomic Bose-Einstein condensate [61]. The Gross-Pitaevskii equation is a time dependant non-linear Schrödinger equation including a potential term:

$$i\hbar\frac{\partial \psi(\mathbf{r},t)}{\partial t} = \left(-\frac{\hbar^2}{2m}\nabla^2 + V(\mathbf{r}) + g|\psi(\mathbf{r},t)|^2\right)\psi(\mathbf{r},t), \tag{4.2}$$

where $\psi(\mathbf{r},t)$ is the condensate wave-function, $V(\mathbf{r})$ is an external potential and g is the non-linear coupling coefficient, which is real. As usual the term $|\psi(\mathbf{r},t)|^2$ gives the local density of the condensate. To find an hydrodynamic formulation, we need to extract a quantity analogue to a local velocity. This can be done combining the time evolution of ψ and ψ^* such as we find

$$\frac{\partial|\psi|^2}{\partial t} + \nabla\cdot\left[\frac{\hbar}{2mi}\left(\psi^*\nabla\psi - \psi\nabla\psi^*\right)\right] = 0. \tag{4.3}$$

We can note that we would have obtained the same equation in the absence of external potential $V(\mathbf{r})$ and in the absence of the non-linear term $g|\psi(\mathbf{r},t)|^2$ as both these terms are real. Indeed this derivation has first been made by Madelung for the usual (linear) Schrödinger equation [62, 63].

We note $\rho = |\psi(\mathbf{r},t)|^2$ the local density. We can see that Eq. 4.3 has the form of a continuity equation for ρ, and may be written as:

$$\frac{\partial\rho}{\partial t} + \nabla\cdot(\rho\mathbf{v}) = 0, \tag{4.4}$$

where we have introduced a quantity $\mathbf{v}$ analogue to a velocity:

$$\mathbf{v} = \frac{\hbar}{2mi} \frac{\psi^* \nabla\psi - \psi \nabla\psi^*}{|\psi(\mathbf{r},t)|^2}. \tag{4.5}$$

It is possible to obtain a simpler expression for the velocity by applying the Madelung transformation to $\psi(\mathbf{r},t)$ and using the real part of the wavefunction $\sqrt{\rho}$ and its phase ϕ:

$$\psi(\mathbf{r},t) = \sqrt{\rho(\mathbf{r},t)} e^{i\phi(\mathbf{r},t)}. \tag{4.6}$$

This allows to write the velocity as:

$$\mathbf{v} = \frac{\hbar}{m} \nabla\phi. \tag{4.7}$$

For example, this derivation can be done in a similar way for the time-evolution of an electromagnetic field in a cavity filled by a $\chi^{(3)}$ non-linear medium [64, 65, 66, 67, 68]. The equation is slightly modified (due to cavity losses [67]) but the main idea remains: the light intensity corresponds to the fluid density, the spatial gradient of its phase to the fluid velocity and the collective behaviour originates from the effective photon-photon interactions due to the non–linearity of the medium inside the cavity.

Historically, the first connection made between superfluid hydrodynamics and non-linear optics dates back to the 80's. Back then, P. Coullet *et al.* related optical phase singularities to quantized vortices in superfluid [69]. A seminal attempt to experimental investigation of superfluid behaviour in a system based on non-linear medium in a macroscopic cavity [70] has been followed by a series of theoretical articles by R. Chiao on superfluidity of light in an atomic medium within a Fabry–Perot cavity [71]. Surprisingly, no experiments were reported thereafter, possibly because large non-linearities and high-Q cavities were hardly available at the time. In parallel, non-linear resonator filled with dye has been investigated and have allowed for the observation of photon BEC [72].

4.2 General overview of exciton-polaritons in a semiconductor microcavity

Modern research on quantum fluids of light has shifted to exciton-polaritons in micro-cavities. These semiconductor nanostructures, thanks to the progress in nano–fabrication, offer unprecedented control of light-matter interaction. In these systems, photons entering a Fabry–Perot cavity strongly couple to excitonic dipolar transitions through quantum wells located at the cavity electric-field maxima. This leads to the creation of massive interacting bosonic quasi-particles known as exciton-polaritons.

Where does the photon effective mass comes from ?

From the confinement inside a Fabry-Perot cavity.

If you take an optical cavity of length L and a refractive index n_c, then the resonance condition leads to $p\lambda_p = 2n_cL$, with p a positive integer and λ_p

the wavelength associated to the mode p. The dispersion relation of light with wavevector $\mathbf{k}$ is:

$$E_c(\mathbf{k}) = \frac{\hbar c}{n_c}|\mathbf{k}| = \frac{\hbar c}{n_c}\sqrt{k_x^2 + k_y^2 + k_z^2}. \tag{4.8}$$

If we assume the cavity to be along the z direction, the quantification of the modes inside the cavity leads to:

$$k_z = p\frac{\pi}{n_c L}. \tag{4.9}$$

We restrict ourselves to small angle of incidence θ on the cavity plane and therefore $k_z = |\mathbf{k}|\cos(\theta) \gg k_x, k_y$. We note the in-plane wavevector $k_\perp = \sqrt{k_x^2 + k_y^2}$. We obtain the general dispersion relation for a cavity:

$$\hbar\omega_c \simeq \frac{\hbar c k_z}{n_c} + \frac{\hbar^2 k_\perp^2}{2m^*}, \tag{4.10}$$

with the definition of an effective mass $m^* = n_c \hbar k_z c$. In typical cavities we have $m^* \sim 5.10^{-7} m_e$, with m_e the electron mass. In this work, we will use microcavities made of GaAs and of length 2λ. The cavity finesse is $F = 3000$.

Where does the interactions comes from ?

From the quantum wells excitons embedded within the microcavity.

A quantum well in a semiconductor consist on thin layer (nano-scale) of small band gap semiconductor, *sandwiched* between two other semiconductor with wider band gap. In our case, we are talking about an InGaAs layer embedded in GaAs. The material discontinuity in the growth direction leads to a confinement of the electronic excitations inside the well region and a discretization of their states inside the well. In semiconductor, the absorption of a photon of adequate wavelength can promote an electron of the valence band (below the Fermi energy) to the conduction band (above the Fermi energy). This will leave an empty spot in the valence band that can be treated as a quasi-particle of positive charge called hole. Both excitations having opposite electronic charge can bound via Coulombian interaction. The energy of the electron-hole pair being reduced, they form a pseudo-particle named exciton. The exciton is then analogue to the 1s orbital of the hydrogen atom, with a positive charge of large mass (the hole) and a negative charge of light mass (the electron) bounded by the Coulombian interaction. For Wannier-Mott exciton, the exciton size is larger than the typical crystal inter-atomic distance.

Excitons can be approximated as bosonic quasi-particles interacting mediated hard-core interaction [73]. Defining a creation operator $\hat{b}_\mathbf{q}$, for an exciton with wavevector $\mathbf{q}$. The interaction hamiltonian is then written as:

$$\hat{H}_{XX} = \frac{1}{2}\sum_{\mathbf{k},\mathbf{k'},\mathbf{q}} V_{XX}\hat{b}^\dagger_{\mathbf{k}+\mathbf{q}}\hat{b}^\dagger_{\mathbf{k'}-\mathbf{q}}\hat{b}_\mathbf{k}\hat{b}_{\mathbf{k'}}. \tag{4.11}$$

This expression describes a scattering process with destruction of 2 excitons at wavevectors $\mathbf{k}$ and $\mathbf{k'}$ and the creation of 2 excitons at wavevectors $\mathbf{k}+\mathbf{q}$ and

$\mathbf{k}' - \mathbf{q}$. We assume the interaction potential V_{XX} to be constant with $\mathbf{q}$ because we are interested at small wavevectors compared to the inverse of the exciton length scale.

I have briefly described the cavity part which gives an effective mass to the photons and the quantum well which will provide the interactions. In the next paragraph, I bring together (strongly) these elements and I introduce the concept of exciton-polaritons.

Exciton-polaritons

The physics of coupling between these two systems is a fantastic example for undergraduate quantum mechanics class. One starts with two bosonic particles associated with the creation operators $\hat{a}^\dagger_{\mathbf{k}}$ and $\hat{b}^\dagger_{\mathbf{k}}$ for cavity photons and excitons respectively. These particles have their own eigen-energies $E_c = \hbar\omega_c$ for the cavity photons and $E_X = \hbar\omega_X$ for the excitons. The hamiltonian of the uncoupled system is clearly diagonal. One adds a coherent coupling energy $\hbar\Omega_R$ between them and the system is not diagonal anymore. After a simple 2-by-2 matrix diagonalization, one obtains the two new eigen-states and eigen-energies, named upper and lower polaritons[1].

We will briefly derive this. In the photon-exciton basis we can write the hamiltonian $\hat{H}$ as:

$$\hat{H} = \begin{bmatrix} E_c & \hbar\Omega_R \\ \hbar\Omega_R & E_X \end{bmatrix}. \tag{4.12}$$

Diagonalization of this hamiltonian gives rise to two new bosonic particles associated with their creation operators $\hat{p}^\dagger_{\mathbf{k}}$ and $\hat{u}^\dagger_{\mathbf{k}}$ for the lower and upper polaritons respectively. As bosonic particles, these operators follow the usual commutation relations. The new eigen-energies are :

$$\begin{aligned} \omega_{UP}(\mathbf{k}) &= \frac{\omega_C(\mathbf{k}) + \omega_X(\mathbf{k})}{2} + \frac{1}{2}\sqrt{[\omega_C(\mathbf{k}) - \omega_X(\mathbf{k})]^2 + 4\Omega_R^2}, \\ \omega_{LP}(\mathbf{k}) &= \frac{\omega_C(\mathbf{k}) + \omega_X(\mathbf{k})}{2} - \frac{1}{2}\sqrt{[\omega_C(\mathbf{k}) - \omega_X(\mathbf{k})]^2 + 4\Omega_R^2}. \end{aligned} \tag{4.13}$$

ω_{LP} and ω_{UP} are associated to the lower and upper polaritons respectively. The eigen-energy is then the mean of the exciton energy and photon energy, with a correction that is the root mean square of the coupling Rabi frequency Ω_R and half of the cavity-exciton detuning $\delta = \omega_C(\mathbf{k}) - \omega_X(\mathbf{k})$.
The polariton eigen-states can be written using the Hopfield coefficients [75]:

$$\begin{cases} \hat{p}_{\mathbf{k}} = X_{\mathbf{k}}\hat{b}_{\mathbf{k}} + C_{\mathbf{k}}\hat{a}_{\mathbf{k}} \\ \hat{u}_{\mathbf{k}} = X_{\mathbf{k}}\hat{a}_{\mathbf{k}} - C_{\mathbf{k}}\hat{b}_{\mathbf{k}} \end{cases} \tag{4.14}$$

[1] Obviously, for this simple treatment we have neglected the exciton-exciton interactions described in the previous section. For a more detailed description please refer to [74]

with

$$X_{\mathbf{k}} = \frac{1}{\sqrt{1+\left[\frac{\Omega_R}{\omega_{LP}(\mathbf{k})-\omega_C(\mathbf{k})}\right]^2}} \qquad (4.15)$$
$$C_{\mathbf{k}} = \frac{-1}{\sqrt{1+\left[\frac{\omega_{LP}(\mathbf{k})-\omega_C(\mathbf{k})}{\Omega_R}\right]^2}}.$$

To give an intuition of the behaviour of these pseudo particles we have plotted in Figure 4.1 the dispersion relation for the upper and lower polaritons for different detunings $\delta = \omega_X(\mathbf{k}) - \omega_C(\mathbf{k})$. This situation is similar to what we realize experimentally [76]. The exciton mass is much larger than the cavity photon effective mass and therefore the dispersion of exciton is almost flat on this scale. To tune the detuning δ we can only control the cavity energy. To do so, the cavity is slightly wedged in one direction, providing a large choice of cavity-exciton detunings by pumping at different positions in the sample. From this figure we can understand intuitively the effect of detuning. For positive detuning (Fig. 4.1-a), the lower polariton branch becomes more excitonic at $\mathbf{k} = 0$ and therefore this enhances the polariton-polariton interactions. On the opposite side, for negative detuning (Fig. 4.1-c), the lower polariton branch becomes more photonic. This can be used to reduce the effective mass and to get more light outside of the system. An important characteristic of this system is that we are only concern on the 2D evolution that in the transverse (cavity) plane.

Strong coupling condition

In the previous paragraph, I have explained what are exciton-polaritons. However, I have skipped one important discussion about strong coupling. Indeed, exciton and photon have a finite lifetime in this system. Photon lifetime τ_C can be obtained from the quality factor Q of the cavity as:

$$\tau_C = \frac{Q}{\omega_C}. \qquad (4.16)$$

For the GaAs cavities we have used in this manuscript, the typical value of τ_C is 20 ps and quality factor are in the order of 10^4.
Exciton lifetime is far less under control and depends mainly of surface irregularities inside the wells. These two quantities give rise to a broadening of the energy by a width $\hbar$ times the inverse of the lifetime. Typical broadening for a GaAs cavity is $\hbar\Gamma_C \sim 50$ μeV.

On the other hand the Rabi frequency can be estimated from the oscillator strength of the exciton f, the size of the cavity L and the exciton mass M:

$$\Omega_r = \sqrt{\frac{fe^2}{2n_c^2 LM\varepsilon_0}}. \qquad (4.17)$$

However this expression assumes a perfect overlap of the exciton and the photon wavefunctions. Quantum wells must be placed carefully in the anti-nodes of the

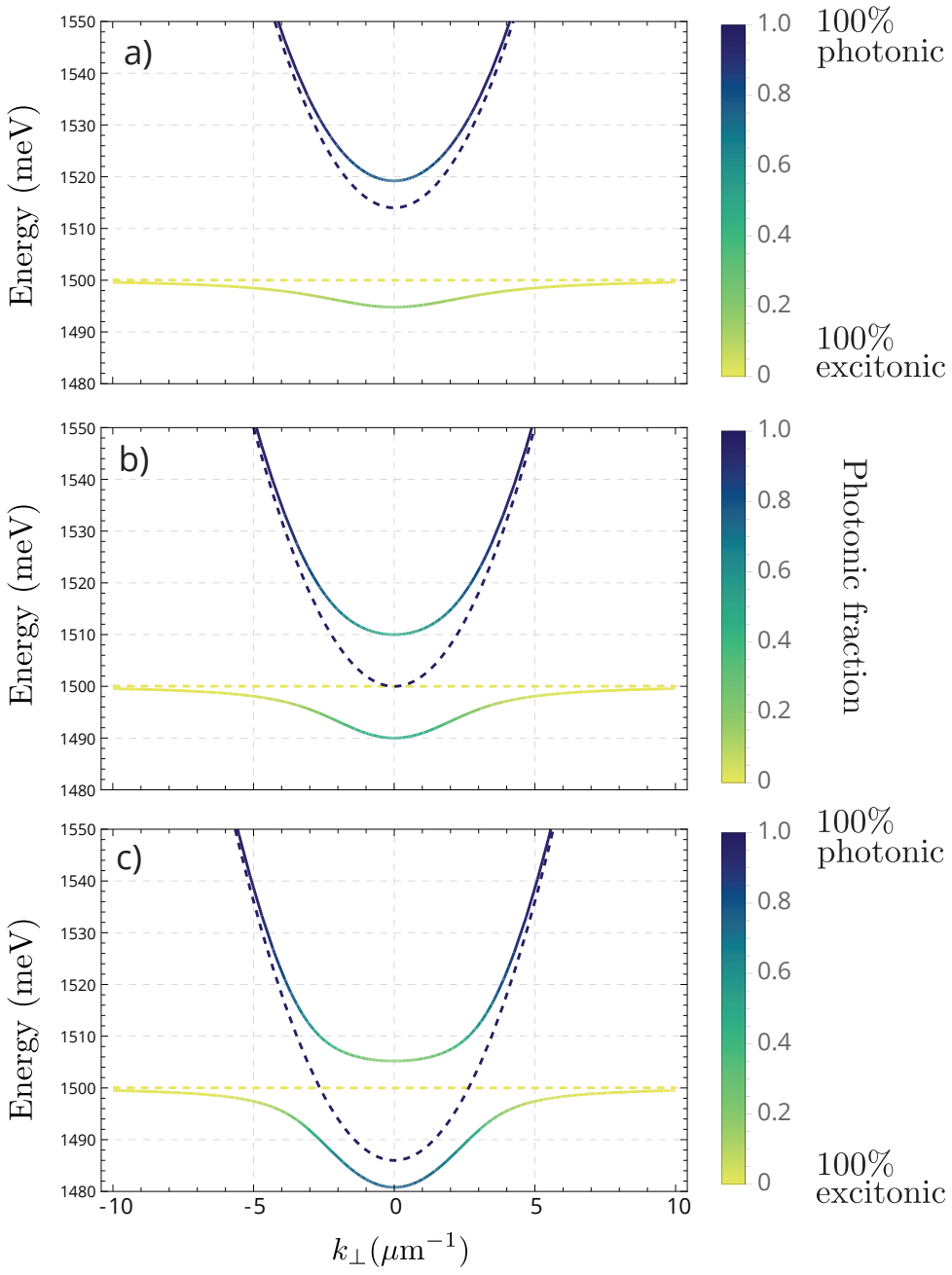

Figure 4.1: Dispersion of upper and lower polaritons. Yellow dashed is the bare exciton dispersion and blue dashed is the bare cavity dispersion. The relative photonic fraction is given in the colorbar. Exciton energy: $Ex = 1500$ meV, Coupling frequency: $\Omega_R = 10$ meV, a) Blue detuned cavity $Ec = 1515$ meV (Marignan), b) Cavity on-resonance $Ec = 1500$ meV, Red detuned cavity $Ec = 1485$ meV.

electromagnetic field in order to optimize the coupling. It is common to increase the Rabi frequency by adding more wells as it scales with the square root of the number of wells (because the effective oscillator strength scales as the number of wells).

We can now give an *graphical* understanding of the strong coupling. The strong coupling condition is achieved when the Rabi frequency is large enough so that polariton states can be distinguished form the uncoupled exciton and photon states. This condition directly depends on the exciton and cavity photon linewidth and can be written:

$$\Omega_R > \Gamma_C, \Gamma_X. \tag{4.18}$$

If this condition is not satisfied, there is no need to talk about polariton states.

4.2.1 Driven-dissipative Gross-Pitaevskii equation

Remarkably, the time evolution of the exciton-polaritons wave-function follows dynamics similar to the Gross-Pitaevksii equation 4.2 describing the evolution of a dilute atomic Bose-Einstein condensate or a monochromatic light propagating in a $\chi^{(3)}$ non-linear media as presented in section 4.1.1. However, for exciton-polaritons, it includes additional non-equilibrium features, streaming from their intrinsic **driven-dissipative nature**. The evolution equation for the lower polaritons reads [77]:

$$i\hbar\frac{\partial\psi(\mathbf{r},t)}{\partial t} = \left(-\frac{\hbar^2}{2m^*}\nabla_\perp^2 + V(\mathbf{r}) - i\frac{\hbar\gamma_{LP}}{2} + g|\psi(\mathbf{r},t)|^2\right)\psi(\mathbf{r},t) + P(\mathbf{r},t), \tag{4.19}$$

with m^* the effective mass of lower polaritons.

On one side, due to the finite reflectively of the cavity's mirrors, photons have a finite lifetime such that eventfully, they exit the cavity. This, which can be seen as a drawback, has proved to be essential as it allows for the detection and measurement of polaritons (via their photonic component). This leads to a dissipation term in the equation proportional to the polariton linewidth: $\hbar\gamma_{LP}$. On the other hand, if photons exit the cavity (after 20 ps typically), new particles must be added (continuously) to the system to maintain a constant number of particles. This is done by pumping the cavity with an external field and leads to a driving term $P(\mathbf{r},t)$ in the equation. Finally, we should restrict the evolution to the plane of the cavity and therefore the 3D spatial derivative is changed to 2D $\nabla_\perp$.

An important feature of polariton physics is therefore that it is out of equilibrium, as particles constantly leave the system. However, with the seminal observation of **exciton-polaritons BEC** [78, 79] and the demonstration of **superfluidity** through resonant Rayleigh scattering [80, 81], this system has become a realistic tool for quantum hydrodynamics. It is worthy to notice that the possibility to observe such fluid of light is allowed by the conjunction of relatively strong $\chi^{(3)}$ non-linearity and a very low effective mass. The latter is essential as it provides for a very fast dynamics to form the fluid in a time scale smaller than the dissipation. This allows for the formation of long-range correlations for example.

4.3 Superfluidity

To conclude this short introduction to light hydrodynamics, I will cover the concept of superfluidity and apply it to light. Superfluidity is the property of a fluid to flow without viscosity below a certain temperature. It has been discovered in Helium 4 cooled at 2 K by Kapitza [82], Allen and Misener [83] in 1937, about 60 years before the first observation of an atomic BEC [84].

However, in 1938 London highlights that superfluid transition temperature and BEC temperature for an ideal gas at the same density are similar and he proposes a link between the two phenomena [85]. Unfortunately, this explanation is not relevant for liquid Helium 4, due to the strong interactions which break the ideal gas model.

In 1941, Landau introduced a novel model based on two fluids: one classical and one condensed which was much more accurate to describe the physics of liquid Helium [86, 87]. He also proposed various criteria to define superfludity. These criteria are still used today to assess superfluidity and to measure the condensed fraction.

Rotating fluid

These criteria are based on a conceptually simple experiment. A fluid (presumably a superfluid) is placed in a bucket and the bucket is rotated. For a superfluid, under the critical velocity, the fluid does not move with the bucket. Above the critical velocity, quantized vortices appear in the fluid. This effect has been observed for the first time by Hess and Fairbank in 1967 [88]. I discuss this criteria in more details in the section 4.4, as we have used a similar technique to store quantized vortices in a polariton superfluid.

Persisting current

Another approach is to put in rotation a classical fluid and then cool it down below the critical point. If now, one removes the rotating mechanism, a superfluid will rotate for a virtually infinite time. This effect has been observed in 1964 in liquid Helium [89] and in 2007 in a BEC with interactions [90]. We can note an interesting proposal to observe a similar mechanism in photon fluid proposed in Ref. [91].

Landau criteria for superfluidity

To derive these criteria we consider a uniform Bose gas with interaction (a uniform quantum fluid) in its ground state. Imagine that we move at velocity $\mathbf{v}$ a solid obstacle through the fluid.

We want to know at which critical velocity v_c, it starts to become possible to create an elementary excitation in the fluid. It is more convenient to work in the reference frame of the obstacle, as the obstacle exerts a time-independent potential to the fluid in this frame. Let us recall the standard Galilean transformations to write the energy $E(\mathbf{v})$ in the frame moving at velocity $\mathbf{v}$ as function

of the energy E and $\mathbf{p}$ the momentum of the fluid in one frame of reference:

$$E(\mathbf{v}) = E - \mathbf{p} \cdot \mathbf{v} + \frac{1}{2} M \mathbf{v}^2, \tag{4.20}$$

where M is the total mass of the system.

If we apply it to our case, we can write the energy of the ground state as:

$$E(\mathbf{v}) = E_0 + \frac{1}{2} M \mathbf{v}^2, \tag{4.21}$$

where E_0 is the ground state energy in the frame where the fluid is at rest, and $\mathbf{p} = 0$. We note ϵ_p the energy cost to add a single excitation of momentum $\mathbf{p}$ to the system. In the original frame the energy of the state with a single excitation is:

$$E_{ex} = E_0 + \epsilon_p, \tag{4.22}$$

and therefore in the moving frame:

$$E_{ex}(\mathbf{v}) = E_0 + \epsilon_p - \mathbf{p} \cdot \mathbf{v} + \frac{1}{2} M \mathbf{v}^2. \tag{4.23}$$

We can now make the difference between Eq. 4.23 and Eq. 4.21 to obtain the energy to create an excitation in the moving frame. Thus at a velocity

$$v = \frac{\epsilon_p}{p}, \tag{4.24}$$

it becomes possible for the obstacle to create an excitation with momentum parallel to $\mathbf{v}$ and at higher velocities, the excitation momentum will have an angle to $\mathbf{v}$. We can conclude with the Landau critical velocity v_c defined as the minimum velocity at which it is possible to create excitation:

$$v_c = \min \left(\frac{\epsilon_p}{p} \right). \tag{4.25}$$

Below the critical velocity there is no mechanism to create elementary excitations and the liquid will exhibit superfluidity. We can note that for a parabolic dispersion of the elementary excitations $\epsilon(p) \propto p^2$, the critical velocity is 0. On the other hand, a linear dispersion $\epsilon(p) \propto p$ will allow for superfluidity.

Suppression of Rayleigh scattering

An important experiment, done in the LKB group before I joined, has demonstrated superfluidity of polaritons using the setup described in the section 4.2. A polariton flow is sent towards a defect and depending on velocity and density of the fluid, elementary excitations are created or not [81]. This experiment is really the foundation of most of the work done in polariton hydrodynamics afterwards and I will review it briefly.

A microcavity is pumped at a small angle by a resonant laser field. The light enters the cavity and hybridizes with excitons to create polaritons with a momentum equal to the projection of the incident laser wavevector in the cavity plane. Some defects can be found in microcavities due to scratches or imperfect

growth, which can be used to study the scattering behaviour of polaritons and probe the superfluidity. In Fig. 4.2 a) we see the polariton fluid hitting the defect and creating fringes upstream the defect. This situation is at low driving intensity, which is equivalent to a low density of polaritons inside the cavity. In this regime the non-linear interaction can be neglected. Two interpretations can be given to these fringes:

- We can think as opticians and interpret this pattern as an interference pattern between incoming photons and photons scattered by the defect. The fringe distance will change when varying the projection of the incident laser wavevector in the cavity plane. This can be verified experimentally.
- The second interpretation comes from the hydrodynamic language. When a normal fluid propagates and hits a defect, characteristic waves appear upstream of the defect similar to water hitting a bridge pile.

In Fig. 4.2 b), we show the k-space (the emission angle of the cavity). The black spot at $k_x = 0$ et $k_y = -0.3\mu\text{m}^{-1}$ is the pumping laser. We can observe a redistribution of the impulsion around a ring at constant k which is Rayleigh scattering on the defect.

To switch to the superfluid regime, we do not have to cool down the fluid as in liquid Helium experiments, but we increase the density. This regime is shown in Fig. 4.2 c) and d). The disappearance of interference fringes is understood intuitively with the hydrodynamic interpretation because the fluid of light, now flows without viscosity. Correspondingly, the Rayleigh scattering vanishes.

The optics interpretation is more obscure as it is a cancellation of the diffraction on the defect due the non-linear effects. We see here for the first time, why the hydrodynamic interpretation is useful to analyze and study optical phenomena that are difficult to predict with the non-linear optics usual toolbox. I will follow this approach in various experiments presented in this chapter.

Finally we can break superfluidity by increasing the velocity above the critical speed v_c. This experiment is reported in Fig. 4.3 c) and d). We will see in the next section that the dispersion elementary excitations in a polariton fluid is linear at low wavevector, and this allows to define a speed of sound c_s which is the critical velocity. In this case, we observe an analogue of the Cerenkov effect. Indeed the excitations created in the fluid have a speed greater than the sound velocity in the medium, and we can observe the characteristic cone upstream of the defect.

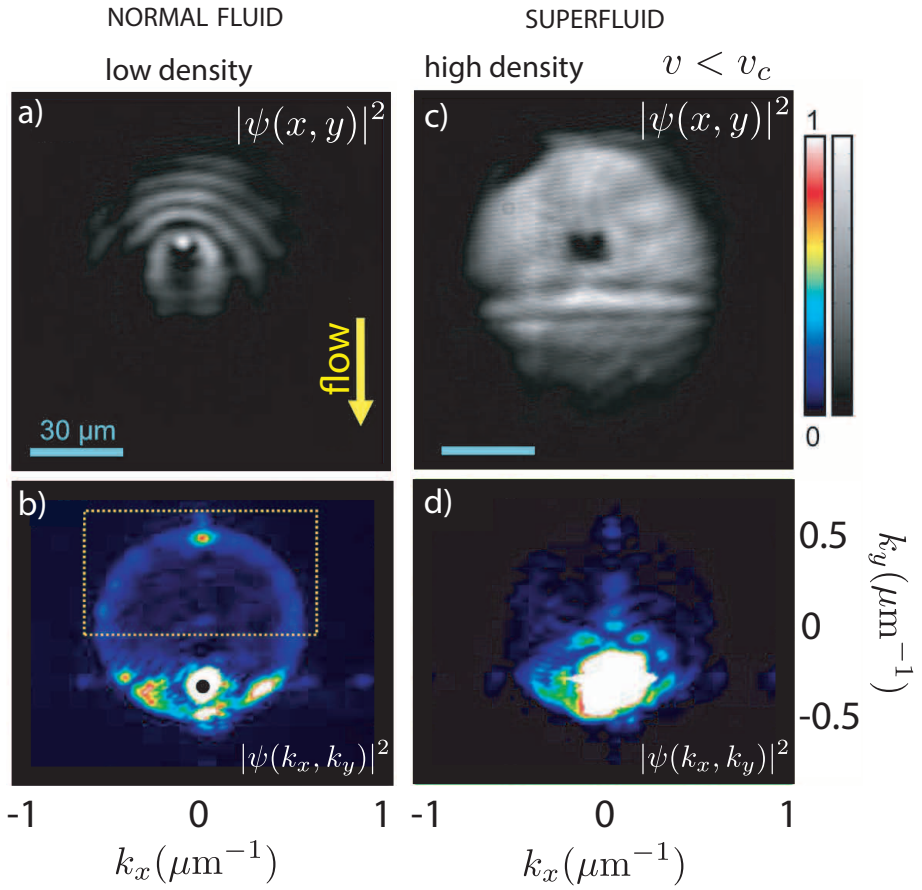

Figure 4.2: Comparison between a normal fluid (at low density a. and b.) and a superfluid (at high density c. and d.). The flow speed v is downwards in real space images a) and c). Interference fringes in a) are due to scattering on the defect. They vanish for higher intensity due to superfluid flow. In k-space images, the Rayleigh scattering is clearly visible in b) and absent in d) due to superfluidity. For the superfluid case $v < v_c$. Adapted from [81]

.

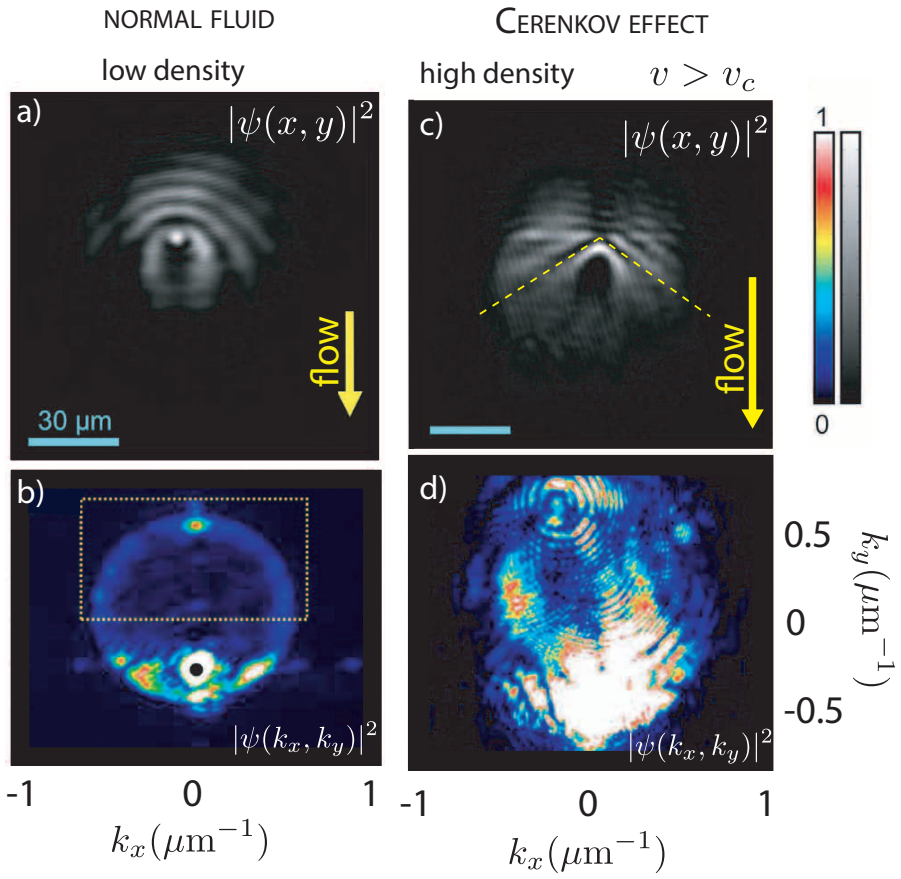

Figure 4.3: Comparison between a normal fluid (at low density a. and b.) and a superfluid (at high density c. and d.) above the critical speed. The flow speed v is downwards in real space images. For c) $v > v_c$. We can observe the break of superfluidity with the apparition of a Cerenkov cone at the defect position in c). The angle of the cone gives the critical velocity (which is the speed of sound in this case). In k-space images, the Rayleigh scattering is clearly visible in b). For the Cerenkov case d) polaritons are scattered at impulsion larger than the k_in as expected by the Landau theory. Adapted from [81].

4.4 Injection of angular momentum in polariton superfluids

A rich variety of photon hydrodynamical effects have been observed, from the unperturbed superfluid stream flowing around a defect [81], to the appearance of a Cerenkov cone in a supersonic flow [81] presented in the previous section. Other works from the LKB group have focused on the formation of topological excitations such as quantized vortices and dark solitons [76, 92]. In this section I give the details about recent experiments done at LKB, where we have achieved the controlled injection of orbital angular momentum in a polariton superfluid using two different techniques.

We have discussed in paragraph 4.3 a method proposed by Landau to probe superfluidity using a rotating bucket. We have revisited this idea by forcing the rotation of a polariton fluid and study the apparition of quantized vortices. Quantized vortices are topological excitations characterized by the vanishing of the field density at a given point (the vortex core) and the quantized winding of the field phase from 0 to 2π around it.

Injection of angular momentum using a Laguerre-Gauss pump

The first method we have studied was to pump the microcavity with a Laguerre-Gauss mode of increasing charge. We have reported the formation of a ring-shaped array of same sign vortices [93]. As previously discussed in the linear regime, an interference pattern is visible. This pattern has a spiral shape and contains phase defects are visible. In the nonlinear (superfluid) regime, the interference disappears and up to eight vortices appear, minimizing the energy while conserving the quantized angular momentum (see figure 4.4).

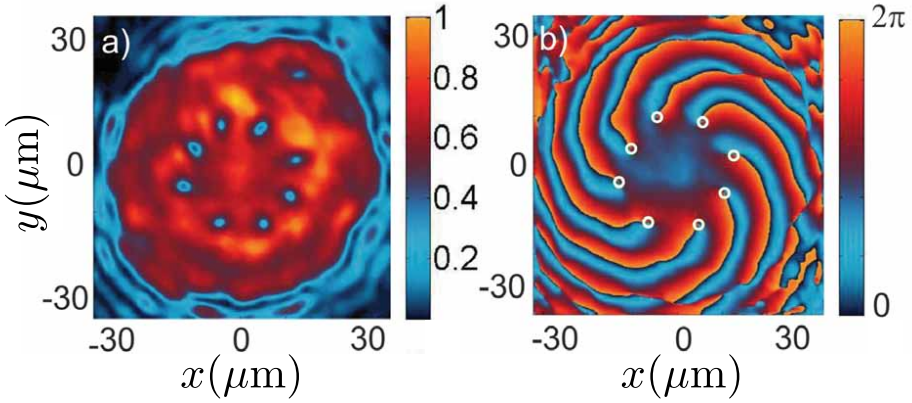

Figure 4.4: Nucleation of same sign vortices. Experimental real space images of the polariton field in the nonlinear regime. a) Polariton density and b) phase pattern. Figure from Ref. [93]

Injection of angular momentum using a 4 tilted pumps

The second experiment studies the propagation of 4 superfluids created with the same pump field at 4 different positions arranged in a square, all with an inward flow. The pump is chosen to be resonant to allow for a fine tuning of the polariton density without generating excitonic reservoir and, consequently, a precise control of the non-linearities in the system.

If we send these fluids toward the center we simply observe the merging of the 4 converging fluids. However, if we tilt the in-plane flow as presented in the figure 1 of PRL 116, 116402 (see below), we can inject an orbital angular momentum in the system and we see the apparition of quantized vortices. We can evaluate the injected orbital angular momentum per photon L in unit of $\hbar$ as:

$$\frac{L}{\hbar} = R|\mathbf{k}| \sin\phi, \tag{4.26}$$

with R is the pump distance to the square center, $\mathbf{k}$ is the in-plane pump wavevector (choose identical for the 4 pumps) and ϕ is the tilt angle between the pump in-plane direction and the square center.

The separation between the pumps is small enough to ensure the four polariton populations can meet, resulting in significant density at the square center. However to ensure that in the central region polaritons are free to evolve, we have cut the beam Gaussian tails to reduce direct illumination.

We use two different techniques for detection: the direct density measurement and a phase measurement. The polariton phase is measured with an off-axis interferometry setup: a beam splitter divides the real space image into two parts, one of which is expanded to generate a flat phase reference beam, used to make an off-axis interference pattern. With this method, the vortex position on the image is independent of the phase of the reference beam. The actual phase map is then numerically reconstructed with a phase retrieval algorithm.

What is striking in this experiment is that even though the orbital angular momentum injected is a continuous quantity, the number of topological defects remains a quantized quantity. We have verified that the number of injected vortices (up to 5) matches a simple model including only the tilt angle (see figure 4 of PRL 116, 116402).

In conclusion we have observed the injection of angular momentum and the storage of topological charges in a non-equilibrium superfluid of light.

These results are presented in the paper attached below [76]. **Injection of Orbital Angular Momentum and Storage of Quantized Vortices in Polariton Superfluids.** T. Boulier, E. Cancellieri, N. D. Sangouard, **Q. Glorieux**, A. V. Kavokin, D. M. Whittaker, E. Giacobino, and A. Bramati. Phys. Rev. Lett. **116**, 116402 (2016).

Injection of Orbital Angular Momentum and Storage of Quantized Vortices in Polariton Superfluids

T. Boulier,[1] E. Cancellieri,[2] N. D. Sangouard,[1] Q. Glorieux,[1] A. V. Kavokin,[3,4] D. M. Whittaker,[2] E. Giacobino,[1] and A. Bramati[1,*]

[1]*Laboratoire Kastler Brossel, UPMC-Sorbonne Universités, CNRS, ENS-PSL Research University, Collège de France, 4, place Jussieu Case 74, F-75005 Paris, France*

[2]*Department of Physics and Astronomy, University of Sheffield, Hicks Building, Hounsfield Road, Sheffield S3 7RH, United Kingdom*

[3]*School of Physics and Astronomy, University of Southampton, Highfield, Southampton SO17 1BJ, United Kingdom*

[4]*CNR-SPIN, Viale del Politecnico 1, Rome I-00133, Italy*

(Received 9 July 2015; revised manuscript received 29 January 2016; published 18 March 2016)

We report the experimental investigation and theoretical modeling of a rotating polariton superfluid relying on an innovative method for the injection of angular momentum. This novel, multipump injection method uses four coherent lasers arranged in a square, resonantly creating four polariton populations propagating inwards. The control available over the direction of propagation of the superflows allows injecting a controllable nonquantized amount of optical angular momentum. When the density at the center is low enough to neglect polariton-polariton interactions, optical singularities, associated with an interference pattern, are visible in the phase. In the superfluid regime resulting from the strong nonlinear polariton-polariton interaction, the interference pattern disappears and only vortices with the same sign are persisting in the system. Remarkably, the number of vortices inside the superfluid region can be controlled by controlling the angular momentum injected by the pumps.

DOI: 10.1103/PhysRevLett.116.116402

Introduction.—In planar semiconductor microcavities, the strong coupling between light (photons) and matter (excitons) [1] gives rise to exciton-polaritons, with specific properties such as a low effective mass, inherited from their photonic component, and strong nonlinear interactions due to their excitonic part. These quasiparticles offer a great opportunity to revisit in solid-state materials the interaction between light and matter, first explored in atomic physics. Polaritonic systems are easily controllable by optical techniques and, due to their finite lifetimes, are ideal systems for studying out-of-equilibrium phenomena [2,3]. In analogy with the atomic case [4,5], the superfluid behavior of polariton quantum fluids has been theoretically predicted [6] and experimentally confirmed [7–9].

Quantized vortices are topological excitations characterized by the vanishing of the field density at a given point (the vortex core) and the quantized winding of the field phase from 0 to 2π around it. Together with solitons, they have been extensively studied and observed in nonlinear optical systems [10], superconductors [11], superfluid ^{4}He [12], and more recently in cold atoms [13–15]. Even though vortices have already been theoretically proposed [16] and experimentally observed [17–21] in polariton fluids, more detailed studies of vortices and vortex arrays are still needed in order to achieve a better understanding of polariton superfluidity and vortex dynamics, as well as to achieve the implementation of quantum technologies [22–24].

Polariton systems have been shown to reveal a large variety of effects with the formation of stable vortices [20,25] and half-vortices [26,27], as well as the formation of single vortex-antivortex (V-AV) pairs [17,18,28], and spin vortices [29]. The formation of lattices of vortices and of V-AV pairs has been theoretically predicted for cavity polaritons [30–32] and observed in the case of patterns induced by metallic deposition on the surface of the cavity [33]. Such lattices are also observable when the interplay between the excitation shape and the underlying disorder pins the vortices, allowing their detection in time-integrated experiments [21].

In the present work, we use four laser beams arranged in a square to resonantly inject polaritons going towards the center of the square. By slightly tilting the pumping direction of the laser beams, the four convergent polariton populations can be made to propagate with a small angle with the direction to the center (see Fig. 1), therefore injecting a controlled angular momentum into the polariton fluid. At the same time, the resonant pumping configuration allows a fine-tuning of the polariton density without generating an excitonic reservoir, and, consequently, a precise control of the nonlinearities in the system, in contrast with the case of out-of-resonant schemes [25,34,35].

With this setup, we demonstrate a new technique for the injection of topological charges in polariton superfluids, a problem of major relevance in driven-dissipative open systems strongly coupled to the environment. Moreover, our study indicates that, in the steady-state regime, the angular momentum continuously injected by the pumps compensates the loss of angular momentum by the system.

 © 2016 American Physical Society

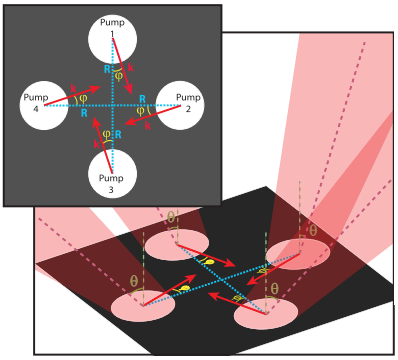

FIG. 1. Schematic representation of the four pumps arriving on the sample. The laser beam is focused on a pinhole before being divided into four equal beams. They are focused on the sample ($a = 12\ \mu$m waist) so that they form four polariton fluids propagating towards each other. θ is the incidence angle, giving the norm of the polariton wave vector $\mathbf{k}$. The in-plane polariton propagation direction is set by the azimuthal angle φ. The blue dashed lines show the direction to the center ($\varphi = 0$) while the red arrows show the polariton direction of propagation for $\theta \neq 0$. R is the distance of the pumps to the center [$R = 25(3)\ \mu$m].

Experiment.—The sample is a 2λ − GaAs planar microcavity containing three $In_{0.05}Ga_{0.95}As$ quantum wells. The finesse is about 3000, which amounts to a polariton linewidth smaller than 0.1 meV and a Rabi spliting $\Omega_R = 5.1$ meV. A wedge between the two cavity Bragg mirrors allows controlling the photon-exciton energy detuning at normal incidence δ, by choosing the appropriate region on the cavity. All measurements presented here were done in a region where the natural cavity disorder is minimum. This region has a slightly positive detuning ($\delta = +0.5$ meV), which provides a good balance between strong interactions and long propagation distance. The lower-polariton resonance at $|\mathbf{k}| = 0$ and $\delta = 0$ is at 837 nm. The cavity is pumped resonantly with a single mode *cw* Ti:sapphire laser, frequency locked to an optical cavity.

The laser is spatially filtered by a 50 μm pinhole so that the Gaussian tail is cut to minimize pump overlap. Three beam splitters divide the laser into four beams of equal intensities, as shown in Fig. 1. The four arms are sent along similar trajectories by dielectric mirrors. Each laser beam is then focused on the sample with a single condenser lens. The pumps are circularly polarized by a quarter-wave plate before hitting the sample. In this way we obtain only one kind of polariton population and avoid any effect due to spin-dependent interactions [36]. For each pump, the real space positions and the angle of incidence can be controlled independently.

The four resonant pumps are spatially arranged on the sample to form a square and are described by $F(\mathbf{r}) = \sum_{j=1}^{4} F_j(\mathbf{r}) \exp(-i\mathbf{k}_j \cdot \mathbf{r})$, where the $F_j(\mathbf{r})$ are the four spatial profiles. Their position in k space is chosen so that polaritons from each pump propagate towards the square center. The four in-plane wave vectors are chosen with the same norm $|\mathbf{k}_j| = |\mathbf{k}|$, meaning that all four pumps hit the sample with the same angle of incidence θ. For a fixed θ, we tilt the in-plane direction of propagation by an angle φ relative to the direction of the center (see Fig. 1). This allows sending onto the cavity a continuous orbital angular momentum (OAM) per photon [37,38], in unit of $\hbar$ that can be evaluated as

$$\frac{L}{\hbar} = \frac{1}{\mathcal{N}} \iint dx dy F^*(\mathbf{r}) \hat{L}_z F(\mathbf{r}) = R|\mathbf{k}| \sin\varphi, \qquad (1)$$

where $\hat{L}_z = \hbar[x(\partial/\partial y) - y(\partial/\partial x)]$ is the z component of the angular momentum, R is the pump distance to the square center, and $\mathcal{N} = \iint d\mathbf{r} F^*(\mathbf{r}) F(\mathbf{r})$ is the normalization constant. Equation (1) has been derived considering a perfectly symmetric system and nonoverlapping pumps with circular profiles induced by the pinhole. As shown in the Supplemental Material [39], in the steady-state regime, the average angular momentum per photon injected by the pumps is equal to the average angular momentum per polariton inside the cavity. Note that since the spatial independence of the injected fields lifts the constraint of the phase circulation quantization, a noninteger (i.e., real-valued) OAM can be injected, which is impossible for a single Laguerre-Gauss field.

The separation between the pumps is small enough so that the four polariton populations can meet, resulting in a significant density at the square center. Cutting the beam Gaussian tails results in negligible direct illumination in the central region of the square. This ensures that in the central region polaritons are free to evolve. If both θ and φ are nonzero, the four polariton populations meet in the system center and an angular momentum is injected.

An objective collects the sample emission and the time-averaged detection is made simultaneously through direct imaging with CCD cameras in real space and momentum space. The energy is measured with a spectrometer. We only collect circularly polarized light, therefore filtering out any spin-flip effect. The polariton phase is measured with an off-axis interferometry setup: a beam splitter divides the real space image into two parts, one of which is expanded to generate a flat phase reference beam, used to make an off-axis interference pattern. With this method, the vortex position on the image is independent of the phase of the reference beam [40]. The actual phase map is then numerically reconstructed with a phase retrieval algorithm.

Numerical method.—To describe the configuration under study, we numerically solve the driven-dissipative scalar Gross-Pitaevskii equation. The field variable $\psi \equiv \psi(\mathbf{r}) = \langle \hat{\psi}(\mathbf{r}) \rangle$ is the mean value of the real-space polariton field operator $\hat{\psi}(\mathbf{r})$. This equation describes the mean field for bidimensional interacting particles with a pump and a decay term as

$$i\hbar \frac{\partial \psi}{\partial t} = \left(-\frac{\hbar^2 \nabla^2}{2m^*} - \frac{i\hbar\gamma}{2} + g|\psi|^2 \right)\psi + \hbar\gamma F(\mathbf{r}) e^{i\Delta t}, \qquad (2)$$

where m^* is the polariton effective mass equal to 9.7×10^{-5} the electron mass, γ is the decay rate deduced from the

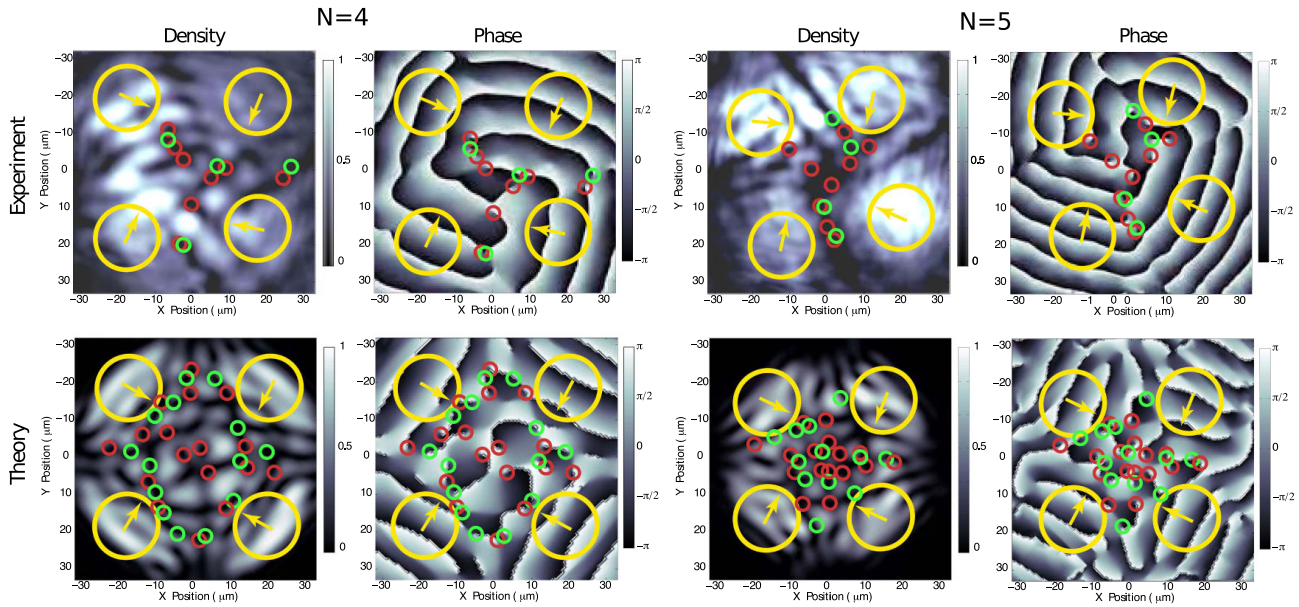

FIG. 2. Experimental (top) and theoretical (bottom) density and phase maps for $\theta = 3.5°$, $\varphi = 21°$ [$L = 4.0(5)$], and $\varphi = 26°$ [$L = 4.9(6)$] in the low density regime. An interference pattern is visible together with phase singularities of both signs. Since the injected angular momentum is not zero, the number of (+) singularities (red circles) is different from the number of (−) singularities (green circles).

polariton lifetime (here, $1/\gamma = 12$ ps), $g = 5$ μeVμm^2 is the polariton-polariton interaction, and $\Delta = \omega_l - \omega_{LP}(|\mathbf{k}|)$ is the energy detuning between the pump laser frequency (ω_l) and the lower polariton branch at $|\mathbf{k}|$, here 0.3 meV. This detuning allows us to compensate for the shift of the lower polariton branch appearing at higher intensities and to have high densities in the superfluid regime. Direct comparison with the experiment is performed by extracting the steady-state density $|\psi|^2$ and phase $\arg(\psi)$. In these conditions, the simulations give a nonturbulent steady-state regime. Therefore, the resulting density and phase maps shown in Fig. 2 are equivalent to time-averaged maps, as in the experiment.

Results.—To highlight the role of polariton-polariton interactions, we study the system as a function of the polariton density. We identify two different regimes: a linear regime at low polariton density, where interactions can be neglected, and a nonlinear regime at high density, where polaritons have a superfluid behavior [8,41,42]. Moreover, in the superfluid state we observe the vanishing of the interference visible in the linear regime when two or more fluids meet [43]. This phenomenon was predicted and observed to be accompanied by the annihilation of all vortex-antivortex pairs [44,45].

For low densities, as shown in Fig. 2, a square interference pattern is visible. This is the behavior expected for noninteracting polaritons, which are similar to cavity photons. Moreover, phase singularities of both signs are visible. It is important to note that, in the linear regime, no healing length can be defined in the density. Therefore, the hydrodynamic definition of a vortex core cannot be applied. In this regime, we observe an unequal number of singularities of opposite signs. The difference between the number of vortices and antivortices ($N \equiv N_+ - N_-$) is equal to the integer part of the angular momentum L expected from Eq. (1). This shows that our technique allows the injection of topological charges by means of OAM. These observations are in agreement with the fact that the sample disorder only generates V-AV pairs [16,18,20,32]. Figure 2 gives an example of a low density regime for $\varphi = 21°$ and $\varphi = 26°$ for a fixed incident angle $\theta = 3.5°$ ($|\mathbf{k}| = 0.45$ μm^{-1}), corresponding to $L = 4.0(5)$ and $L = 4.9(6)$, respectively (uncertainty based on the error in the evaluation of R). Equation (2) provides qualitatively correct predictions in the linear regime. A difference in the number of V-AV pairs between experiment and simulation can be ascribed to imperfections of the sample, which at low density play an important role. In this regime the system reaches a steady state with vortices lying in fixed positions. This is confirmed by the simulations, as said before, and by high values of visibility (not shown here) all over the pumped region, apart from the vortex cores.

By increasing the density to the point where, in the central region, the polariton fluid reaches the superfluid regime (see Fig. 3), the interference pattern disappears and all V-AV pairs annihilate, showing the interaction-driven nature of this phenomenon [43,44]. The nonzero angular momentum injected by the pumps results in the presence of elementary vortices of the same sign remaining in the superfluid. Their size is of the order of the healing length (about 2 μm) that can be unambiguously defined [7,8,43]. Up to five vortices were observed without any antivortex. Figure 3 shows the experimental results for $\varphi = 5.5°$ [$L = 1.1(1)$], $\varphi = 10°$ [$L = 2.0(2)$], and $\varphi = 21°$

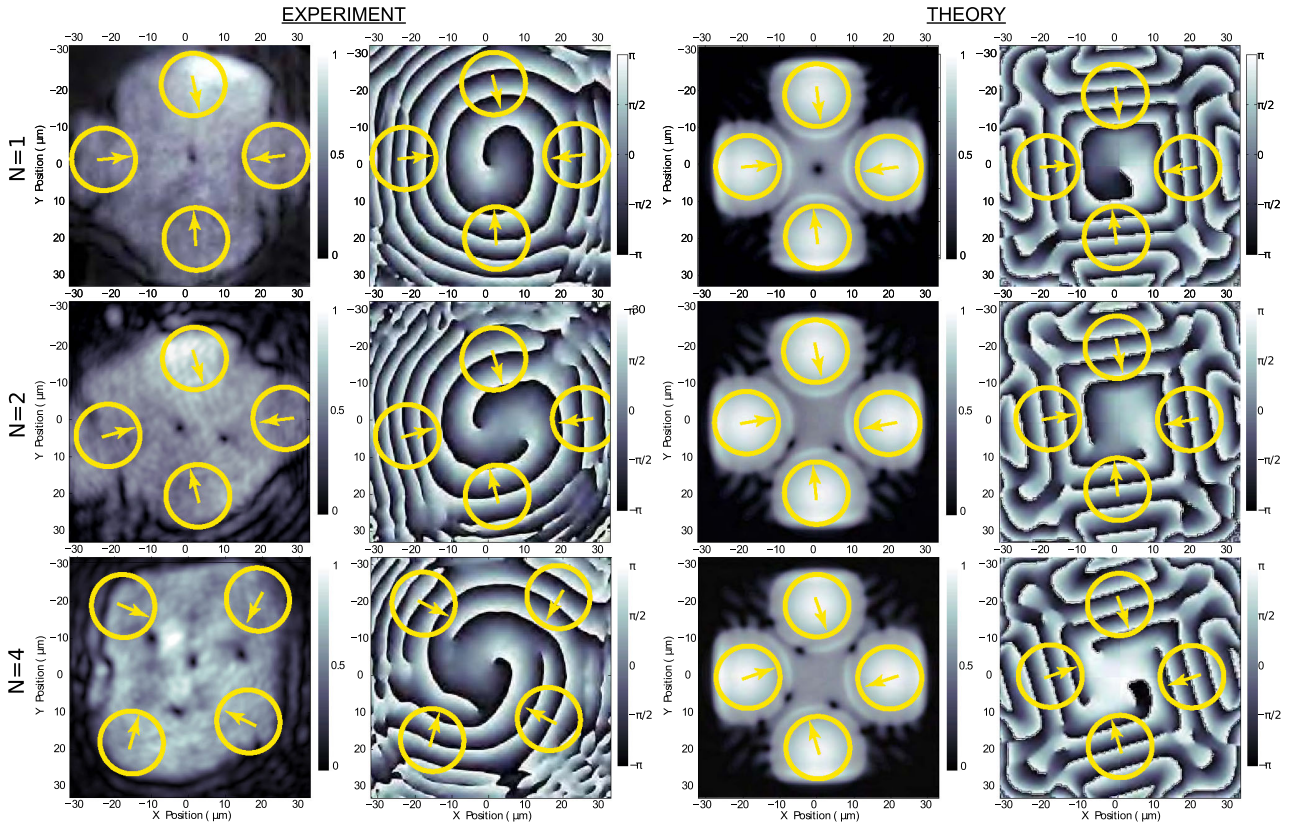

FIG. 3. Experimental (left) and theoretical (right) density and phase maps for $L = 1.1(1)$, 2.0(2), 4.0(5) (from top to bottom) at high density. The vortex number N is equal to the integer part of L. The vortices are visible as black dots in the density, each associated with a phase singularity. On average, $|\mathbf{k}| = 0.45\ \mu\text{m}^{-1}$ and (from top to bottom) $\varphi = 5.5°$, 10°, 21°.

$[L = 4.0(5)]$, for a fixed $\theta = 3.5°$ giving $|\mathbf{k}| = 0.45\ \mu\text{m}^{-1}$. As expected, the number of vortices increases with φ.

A comparison between the observed number of vortices N in the superfluid regime and the value of L computed from the classical approach Eq. (1) is presented in Fig. 4(a). The agreement is good within the uncertainty on φ and R, showing the validity of our approach that allows the storage of quantized vortices by injecting orbital angular momentum. The vortex position is observed to depend strongly on each pump phase, which suggests that the vortex lattice shape is related to the geometry of the polariton superflow. This, together with the presence of disorder in the sample, can explain the discrepancies in the vortex position in the model and in the experiment. In the numerical simulations, the pumps phase and position are set slightly different in order to reproduce the asymmetry of the experimental case.

Finally, in the high density case, it is interesting to look at the Mach number map, which is defined as the ratio between the local velocity of the fluid and the local speed of sound (proportional to the square root of the polariton density). Figure 4(b) shows the Mach number map for $L = 4.0(5)$ corresponding to the bottom panels of Fig. 3. As expected from the absence of interference pattern, the fluid is subsonic ($M < 1$), which means that it is in the superfluid regime [7,8]. Note, however, that polaritons within each vortex are strongly supersonic. Indeed, at the vortex core, the Mach number is expected to diverge, and experimental values up to $M = 100$ are obtained.

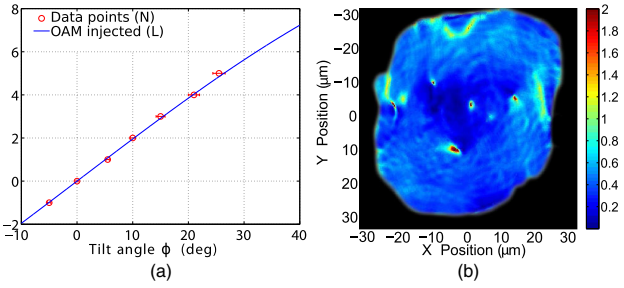

FIG. 4. (a) Plot of the observed number of vortices N (red circles) and of the continuous angular momentum L from Eq. (1) (blue line) as a function of the azimuthal angle φ. (b) Experimental map of the Mach number for the case of $L = 4.0(5)$. The black zones signify areas outside of the superfluid, where the polariton density is too low to define a Mach number. In the blue zone, the fluid is subsonic. However, polaritons within each vortex are strongly supersonic. Note that the Mach number scale is limited between 0 and 2, while at the vortex core the Mach number diverges and experimental values up to 100 are obtained.

Conclusion.—We designed a scheme that allows the injection of a controlled angular momentum in a bidimensional polariton superfluid. The scheme makes use of four coherent polariton populations. While in the linear regime interferences appear and phase singularities of opposite charges are clearly visible, the vanishing of all possible pairs happens at sufficiently high density, and only same sign vortices survive as expected for a coherent superfluid. We therefore observed the injection of angular momentum and the storage of topological charges in a nonequilibrium superfluid of light. Together with the recent result obtained in Ref. [43], this is an interesting achievement in polariton physics. Up to now, only vortex-antivortex pairs [17,18,20,21,34], single vortex [9,46], and vortices with high L confined by an excitonic reservoir [25] have been observed. Our method allows us to very efficiently imprint large values of orbital angular momentum and observe several vortices with a topological charge of 1. With a large number of vortices, this result opens the way to the study of vortex-vortex interactions, vortex lattices, and their collective modes [47,48]. The technique presented in this Letter, coupled with the use of a time-resolved setup, could also lead to interesting new studies in the physics of vortices in a turbulent regime [18].

We acknowledge the financial support of the ANR Quandyde (ANR-11-BS10-001) and EPSRC Grant No. EP/J007544, and Iacopo Carusotto and Paulo Maia Neto for very helpful discussions.

*bramati@lkb.umpc.fr

[1] C. Weisbuch, M. Nishioka, A. Ishikawa, and Y. Arakawa, Observation of the Coupled Exciton-Photon Mode Splitting in a Semiconductor Quantum Microcavity, Phys. Rev. Lett. **69**, 3314 (1992).

[2] H. Deng, H. Haug, and Y. Yamamoto, Exciton-polariton Bose-Einstein condensation, Rev. Mod. Phys. **82**, 1489 (2010).

[3] I. Carusotto and C. Ciuti, Quantum fluids of light, Rev. Mod. Phys. **85**, 299 (2013).

[4] F. Dalfovo, S. Giorgini, L. P. Pitaevskii, and S. Stringari, Theory of Bose-Einstein condensation in trapped gases, Rev. Mod. Phys. **71**, 463 (1999).

[5] S. Burger, F. S. Cataliotti, C. Fort, F. Minardi, M. Inguscio, M. L. Chiofalo, and M. P. Tosi, Superfluid and Dissipative Dynamics of a Bose-Einstein Condensate in a Periodic Optical Potential, Phys. Rev. Lett. **86**, 4447 (2001).

[6] I. Carusotto and C. Ciuti, Probing Microcavity Polariton Superfluidity through Resonant Rayleigh Scattering, Phys. Rev. Lett. **93**, 166401 (2004).

[7] A. Amo *et al.*, Collective fluid dynamics of a polariton condensate in a semiconductor microcavity, Nature (London) **457**, 291 (2009).

[8] A. Amo, J. Lefrère, S. Pigeon, C. Adrados, C. Ciuti, I. Carusotto, R. Houdré, E. Giacobino, and A. Bramati, Superfluidity of polaritons in semiconductor microcavities, Nat. Phys. **5**, 805 (2009).

[9] D. Sanvitto *et al.*, Persistent currents and quantized vortices in a polariton superfluid, Nat. Phys. **6**, 527 (2010).

[10] A. S. Desyatnikov, L. Torner, and Y. S. Kivshar, Optical vortices and vortex solitons, Prog. Opt. **47**, 291 (2005).

[11] U. Essmann and H. Träuble, The direct observation of individual flux lines in type II superconductors, Phys. Lett. A **24**, 526 (1967).

[12] G. W. Rayfield and F. Reif, Quantized vortex rings in superfluid helium, Phys. Rev. **136**, A1194 (1964).

[13] K. W. Madison, F. Chevy, W. Wohlleben, and J. Dalibard, Vortex Formation in a Stirred Bose-Einstein Condensate, Phys. Rev. Lett. **84**, 806 (2000).

[14] J. Denschlag *et al.*, Generating solitons by phase engineering of a Bose-Einstein condensate, Science **287**, 97 (2000).

[15] L. Khaykovich *et al.*, Formation of a matter-wave bright soliton, Science **296**, 1290 (2002).

[16] S. Pigeon, I. Carusotto, and C. Ciuti, Hydrodynamic nucleation of vortices and solitons in a resonantly excited polariton superfluid, Phys. Rev. B **83**, 144513 (2011).

[17] G. Roumpos, M. D. Fraser, A. Löffler, S. Höfling, A. Forchel, and Y. Yamamoto, Single vortex-antivortex pair in an exciton-polariton condensate, Nat. Phys. **7**, 129 (2011).

[18] G. Nardin, G. Grosso, Y. Léger, B. Pięłka, F. Morier-Genoud, and B. Deveaud-Plédran, Hydrodynamic nucleation of quantized vortex pairs in a polariton quantum fluid, Nat. Phys. **7**, 635 (2011).

[19] D. Sanvitto *et al.*, All-optical control of the quantum flow of a polariton condensate, Nat. Photonics **5**, 610 (2011).

[20] K. G. Lagoudakis, M. Wouters, M. Richard, A. Baas, I. Carusotto, R. André, L. S. Dang, and B. Deveaud-Plédran, Quantized vortices in an exciton-polariton condensate, Nat. Phys. **4**, 706 (2008).

[21] F. Manni, T. C. H. Liew, K. G. Lagoudakis, C. Ouellet-Plamondon, R. André, V. Savona, and B. Deveaud, Spontaneous self-ordered states of vortex-antivortex pairs in a polariton condensate, Phys. Rev. B **88**, 201303 (2013).

[22] W. Zhenghan, *Topological Quantum Computation* (American Mathematical Society, Providence, RI, 2010), Vol. 112.

[23] M. Freedman, A. Kitaev, M. Larsen, and Z. Wang, Topological quantum computation, Bull. Am. Math. Soc. **40**, 31 (2003).

[24] C. Nayak, S. H. Simon, A. Stern, M. Freedman, and S. D. Sarma, Non-Abelian anyons and topological quantum computation, Rev. Mod. Phys. **80**, 1083 (2008).

[25] R. Dall, M. D. Fraser, A. S. Desyatnikov, G. Li, S. Brodbeck, M. Kamp, C. Schneider, S. Höfling, and E. A. Ostrovskaya, Creation of Orbital Angular Momentum States with Chiral Polaritonic Lenses, Phys. Rev. Lett. **113**, 200404 (2014).

[26] K. Lagoudakis, T. Ostatnicky, A. V. Kavokin, Y. G. Rubo, R. André, and B. Deveaud-Plédran, Observation of half-quantum vortices in an exciton-polariton condensate, Science **326**, 974 (2009).

[27] H. Flayac, I. A. Shelykh, D. D. Solnyshkov, and G. Malpuech, Topological stability of the half-vortices in spinor exciton-polariton condensates, Phys. Rev. B **81**, 045318 (2010).

[28] G. Tosi *et al.*, Onset and Dynamics of Vortex-Antivortex Pairs in Polariton Optical Parametric Oscillator Superfluids, Phys. Rev. Lett. **107**, 036401 (2011).

[29] S. Dufferwiel *et al.*, Spin Textures of Exciton-Polaritons in a Tunable Microcavity with Large TE-TM Splitting, Phys. Rev. Lett. **115**, 246401 (2015).
[30] J. Keeling and N. G. Berloff, Spontaneous Rotating Vortex Lattices in a Pumped Decaying Condensate, Phys. Rev. Lett. **100**, 250401 (2008).
[31] A. V. Gorbach, R. Hartley, and D. V. Skryabin, Vortex Lattices in Coherently Pumped Polariton Microcavities, Phys. Rev. Lett. **104**, 213903 (2010).
[32] T. C. H. Liew, Y. G. Rubo, and A. V. Kavokin, Generation and Dynamics of Vortex Lattices in Coherent Exciton-Polariton Fields, Phys. Rev. Lett. **101**, 187401 (2008).
[33] K. Kusudo, N. Y. Kim, A. Löffler, S. Höfling, A. Forchel, and Y. Yamamoto, Stochastic formation of polariton condensates in two degenerate orbital states, Phys. Rev. B **87**, 214503 (2013).
[34] G. Tosi, G. Christmann, N. G. Berloff, P. Tsotsis, T. Gao, Z. Hatzopoulos, P. G. Savvidis, and J. J. Baumberg, Geometrically locked vortex lattices in semiconductor quantum fluids, Nat. Commun. **3**, 1243 (2012).
[35] P. Cristofolini, A. Dreismann, G. Christmann, G. Franchetti, N. G. Berloff, P. Tsotsis, Z. Hatzopoulos, P. G. Savvidis, and J. J. Baumberg, Optical Superfluid Phase Transitions and Trapping of Polariton Condensates, Phys. Rev. Lett. **110**, 186403 (2013).
[36] M. Vladimirova, S. Cronenberger, D. Scalbert, K. V. Kavokin, A. Miard, A. Lemaître, J. Bloch, D. Solnyshkov, G. Malpuech, and A. V. Kavokin, Polariton-polariton interaction constants in microcavities, Phys. Rev. B **82**, 075301 (2010).
[37] A. M. Amaral, E. L. Falcão-Filho, and C. B. de Araújo, Characterization of topological charge and orbital angular momentum of shaped optical vortices, Opt. Express **22**, 30315 (2014).
[38] L. Allen and M. Padgett, The Poynting vector in Laguerre-Gaussian beams and the interpretation of their angular momentum density, Opt. Commun. **184**, 67 (2000).
[39] See Supplemental Material at http://link.aps.org/supplemental/10.1103/PhysRevLett.116.116402 for a theoretical calculation of the conservation of the orbital angular momentum injected by the pump in the polariton superfluid in the steady state regime.
[40] E. L. Bolda and D. F. Walls, Detection of Vorticity in Bose-Einstein Condensed Gases by Matter-Wave Interference, Phys. Rev. Lett. **81**, 5477 (1998).
[41] A. Amo *et al.*, Polariton superfluids reveal quantum hydrodynamic solitons, Science **332**, 1167 (2011).
[42] R. Hivet *et al.*, Half-solitons in a polariton quantum fluid behave like magnetic monopoles, Nat. Phys. **8**, 724 (2012).
[43] T. Boulier, H. Terças, D. D. Solnyshkov, Q. Glorieux, E. Giacobino, G. Malpuech, and A. Bramati, Vortex chain in a resonantly pumped polariton superfluid, Sci. Rep. **5**, 9230 (2015).
[44] E. Cancellieri, T. Boulier, R. Hivet, D. Ballarini, D. Sanvitto, M. H. Szymanska, C. Ciuti, E. Giacobino, and A. Bramati, Merging of vortices and antivortices in polariton superfluids, Phys. Rev. B **90**, 214518 (2014).
[45] R. Hivet, E. Cancellieri, T. Boulier, D. Ballarini, D. Sanvitto, F. M. Marchetti, M. H. Szymanska, C. Ciuti, E. Giacobino, and A. Bramati, Interaction-shaped vortex-antivortex lattices in polariton fluids, Phys. Rev. B **89**, 134501 (2014).
[46] L. Dominici *et al.*, Vortex and half-vortex dynamics in a nonlinear spinor quantum fluid, Sci. Adv. **1**, e1500807 (2015).
[47] V. K. Tkachenko, Stability of vortex lattices, Sov. Phys. JETP **23**, 1049 (1966).
[48] I. Coddington, P. Engels, V. Schweikhard, and E. A. Cornell, Observation of Tkachenko Oscillations in Rapidly Rotating Bose-Einstein Condensates, Phys. Rev. Lett. **91**, 100402 (2003).

4.5 Fluid of light in the propagating geometry

As we have seen in the previous section, fluids of light allow to revisit quantum gases experiments with the advantage of the precise control in state preparation and detection of optical systems. So far I have presented results about cavity-based platforms which have intrinsic losses and therefore are restricted to driven-dissipative dynamics. In 2016, I have started a new thematic in the LKB group to overcome this limitation with a different way of doing quantum simulation with light, by removing the need for a Fabry-Perot cavity. This approach brings complementary results to the exciton-polaritons experiments and gives the possibility for our group to compare driven-dissipative and conservative dynamics with fluids of light. Similarly to exciton-polaritons, it relies on the formal mapping between the dynamics of the problem we wish to simulate and the quantum system we will use to do it.

The system we propose to use is light propagating through a warm atomic vapor and I show that this system can be theoretically described by a nonlinear Schrödinger equation similar to Eq. 4.2. To validate experimentally this approach, I present recent results about the dispersion relation of elementary excitations in this system and show that they follow a Bogoliubov spectrum similar to atomic BEC or photon BEC[72] experiments.

4.5.1 Bogoliubov dispersion relation

Before going in the details of our system, I review briefly the physics of elementary excitations in the Gross-Pitaevskii equation (Eq. 4.2). More specifically, I derive the Bogoliubov dispersion relation for a uniform Bose gas in the absence of external potential.

We start by writing the quantum state as a mean field plus a small perturbation to linearize the Gross-Pitaevskii equation:

$$\Psi(\mathbf{r},t) = [\psi_0(\mathbf{r},t) + \delta\psi(\mathbf{r},t)]. \tag{4.27}$$

Here $\psi_0(\mathbf{r},t)$ is the condensate wavefunction in the unperturbed state. It can then be written:

$$\psi_0 = \sqrt{n(\mathbf{r})}\mathrm{e}^{-i\mu t/\hbar}, \tag{4.28}$$

where $n(\mathbf{r}$ is the equilibrium density of particles and μ is the chemical potential. For a uniform system $n(\mathbf{r}$ is independent of $\mathbf{r}$ and μ is given by $\mu = |\psi_0|^2 g = ng$. For $\delta\psi(\mathbf{r},t)$, we are interested in solution of the form:

$$\delta\psi(\mathbf{r},t) = \left[u(\mathbf{r})\mathrm{e}^{-i\omega t} - v^*(\mathbf{r})\mathrm{e}^{i\omega t}\right]\mathrm{e}^{-i\mu t/\hbar}. \tag{4.29}$$

with ω a real quantity. Inserting this ansatz in the linearized Gross-Pitaevskii equation we obtain two coupled equations for $u(\mathbf{r})$ and $v(\mathbf{r})$ known as the Bogoliubov equations:

$$\begin{aligned}\left[-\frac{\hbar^2}{2m}\nabla^2 + gn - \hbar\omega\right] u(\mathbf{r}) - gn\; v(\mathbf{r}) = 0 \\ \left[-\frac{\hbar^2}{2m}\nabla^2 + gn + \hbar\omega\right] v(\mathbf{r}) - gn\; u(\mathbf{r}) = 0\end{aligned} \tag{4.30}$$

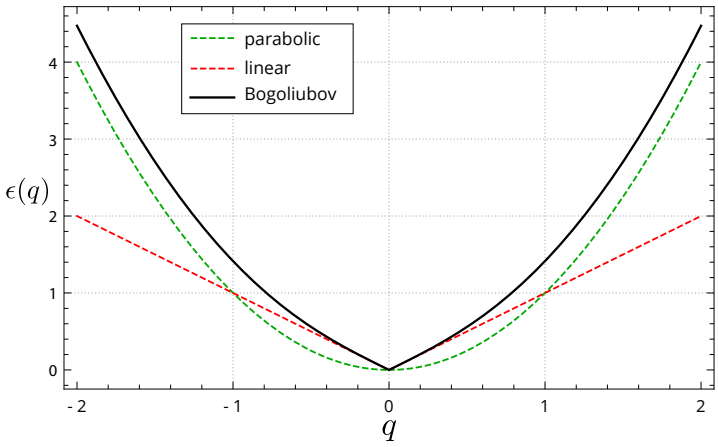

Figure 4.5: Dispersion relation for massive particles (dashed green), for sound waves (dashed red) and for Eq. 4.33 (black). $c_s = 1$ and $\epsilon(q)$ in $\hbar$ unit.

Because of the translational invariance in a uniform Bose gas we can take $u(\mathbf{r})$ et $v(\mathbf{r})$ to be of the form of plane waves:

$$u(\mathbf{r}) = u_q e^{i\mathbf{qr}} \text{ and } v(\mathbf{r}) = v_q e^{i\mathbf{qr}}. \tag{4.31}$$

By injecting these expressions in Eq. 4.30 we obtain two equations that are consistent only if the determinant of the coefficients vanishes. Finally we obtain:

$$(\hbar\omega)^2 = \left[\frac{\hbar^2 q^2}{2m} + gn\right]^2 - (gn)^2 \tag{4.32}$$

We take the positive energy solutions and we obtain the Bogoliubov dispersion relation:

$$\epsilon(q) = \hbar\omega(q) = \sqrt{\varepsilon_0(q)} \cdot \sqrt{\varepsilon_0(q) + 2gn}. \tag{4.33}$$

Here we have introduced the notation $\varepsilon_0(q) = \frac{\hbar^2 q^2}{2m}$ for the energy of the free-particle without interaction.

We can see from this expression that the Bogoliubov dispersion differs from the massive particle parabolic dispersion only at small q when $2gn \leq \varepsilon_0(q)$. In the limit $2gn/\varepsilon_0(q) \gg 1$, we can approximate Eq. 4.33 by

$$\epsilon(q) = \hbar\sqrt{\frac{gn}{m}}q. \tag{4.34}$$

In this limit, the spectrum become linear (sound-like) and we can define a speed of sound c_s that scales with the square root of the density:

$$c_s = \sqrt{\frac{gn}{m}}. \tag{4.35}$$

If we use the Landau criteria for superfluidity (Eq. 4.25), we can see that this dispersion allows for a minimum of the quantity $\frac{\epsilon(q)}{q}$ which is precisely equal to c_s.

4.5.2 Non-linear propagation in a $\chi^{(3)}$ medium

In the absence of sources, the propagation of light in a medium of refractive index n is given by the Helmholtz equation:

$$\nabla^2 E - \frac{n^2}{c^2}\frac{\partial^2 E}{\partial t^2} = 0, \tag{4.36}$$

where E is the electric field amplitude and c is the speed of light in vacuum. To take into account the propagation in a non-linear medium of we need to a non-linear polarization term P_{NL} in the form:

$$\nabla^2 E - \frac{n^2}{c^2}\frac{\partial^2 E}{\partial t^2} = \frac{1}{\varepsilon_0 c^2}\frac{\partial^2 P_{NL}}{\partial t^2}. \tag{4.37}$$

n is the linear part of the refractive index.
For a $\chi^{(3)}$ non-linear medium we have $P_{NL} = \varepsilon_0 \chi^{(3)} E^3$. We assume the electric field to be monochromatic (at frequency ω_0) and to propagate along z. We introduce k_0, the wavenumber of E, and we decompose the envelope E_0 from the oscillating part:

$$E(x, y, z, t) = E_0(x, y, z)e^{i(k_0 z - \omega_0 t)}. \tag{4.38}$$

We can inject this expression of E into Eq. 4.37 to get

$$\nabla_\perp^2 E_0 + \frac{\partial^2 E_0}{\partial z^2} + 2ik_0\frac{\partial E_0}{\partial z} - \left(k_0^2 - n^2\frac{\omega_0^2}{c^2}\right)E_0 = -\chi^{(3)}|E_0|^2\frac{\omega_0^2}{c^2}E_0, \tag{4.39}$$

where $\nabla_\perp^2$ is the Laplacian in the transverse (x, y) plane. We then take into account that E_0 is slowly varying along z, known as the paraxial approximation, to eliminate the second derivative of E_0 along z. We can rewrite Eq. 4.39 with this simplification:

$$\nabla_\perp^2 E_0 + 2ik_0\frac{\partial E_0}{\partial z} - \left(k_0^2 - n^2\frac{\omega_0^2}{c^2}\right)E_0 + \chi^{(3)}|E_0|^2\frac{\omega_0^2}{c^2}E_0 = 0. \tag{4.40}$$

We can decompose the linear part of the refractive index as $n = n_0 + \delta n(\mathbf{r})$ with a mean index plus a local perturbation (supposed weak). As $k_0 = n_0\omega_0/c$, we can rewrite Eq. 4.40 as:

$$i\frac{\partial E_0}{\partial z} = -\frac{1}{2k_0}\nabla_\perp^2 E_0 - \frac{\delta n k_0}{n_0}E_0 - \frac{k_0\chi^{(3)}}{2n_0^2}|E_0|^2 E_0. \tag{4.41}$$

This equation is analogue to the Gross-Pitaevskii equation (Eq. 4.2). We will therefore be able to use the same formalism, and in particular we can expect a Bogoliubov dispersion relation for the small perturbation on the electric field. We introduce the light intensity I and the non-linear index n_2. We have:

$$n_2 = \frac{3\chi^{(3)}}{2n_0^2\varepsilon_0 c} \text{ and } I = |E_0|^2 n_0 \varepsilon_0 c/2. \tag{4.42}$$

This allows to write an important quantity experimentally: the non-linear contribution to the index of refraction: $\Delta n = n_2 I$.

To precise the analogy with the Gross-Pitaevskii equation (GPE), I have rewritten Eq. 4.2 and compared it to Eq. 4.40.

$$\begin{aligned} i\hbar\frac{\partial\psi(\mathbf{r},t)}{\partial t} &= \left(-\frac{\hbar^2}{2m}\nabla^2 + V(\mathbf{r}) + g\,|\psi(\mathbf{r},t)|^2\right)\psi(\mathbf{r},t) \\ i\frac{\partial E_0(\mathbf{r}_\perp,z)}{\partial z} &= \left(-\frac{1}{2k_0}\nabla_\perp^2 - \frac{\delta n(\mathbf{r}_\perp)k_0}{n_0} - \frac{k_0\chi^{(3)}}{2n_0^2}|E_0|^2\right)E_0(\mathbf{r}_\perp,z). \end{aligned}$$

The first remark is that the left term in GPE is a time derivative as it is a spatial derivative along the propagation direction for Eq. 4.40. The dynamics in Eq. 4.40 is then 2D in the transverse plane written $\mathbf{r}_\perp = (x, y)$. Each slice at a given z is equivalent to a time-snapshot in the GPE. More precisely we can fix the initial state by designing a given field at the input of the medium $z = 0$ and measure the evolution after an effective time by imaging the intensity and phase at the output of the medium $z = L$.

We can now propose a mapping of the different quantity to directly write the expected Bogoliubov dispersion for small perturbation in Eq. 4.40.

$$\begin{aligned} \text{GPE} &\leftrightarrow \text{Non-linear Optics} \\ \psi(\mathbf{r},t) &\leftrightarrow E_0(\mathbf{r}_\perp,z) \\ m/\hbar &\leftrightarrow k_0 \\ V(\mathbf{r})/\hbar &\leftrightarrow -\delta n(\mathbf{r}_\perp)k_0/n_0 \\ g/\hbar &\leftrightarrow -\frac{k_0\chi^{(3)}}{2n_0^2} \end{aligned}$$

We also need to *translate* the frequency ω and the wavenumber q of the Bogoliubov excitations. As time is mapped to z, ω is mapped to a spatial frequency in the propagation direction. It is denoted Ω_B to avoid confusion. We have:

$$\begin{aligned} \mathbf{q} &\leftrightarrow \mathbf{k}_\perp \\ \omega(\mathbf{q}) &\leftrightarrow \Omega_B(\mathbf{k}_\perp) \end{aligned}$$

We can now rewrite the Bogoliubov dispersion in the Non-linear Optics analogy:

$$\epsilon(\mathbf{k}_\perp) = \Omega_B(\mathbf{k}_\perp) = \sqrt{\frac{{\mathbf{k}_\perp}^2}{2k_0}}\cdot\sqrt{\frac{{\mathbf{k}_\perp}^2}{2k_0} - \frac{k_0\chi^{(3)}}{n_0^2}|E_0|^2}. \tag{4.43}$$

Similarly to Bose gases, we can define two limits depending on the value of the wavevector $\mathbf{k}_\perp$ compared to the inverse of the healing length ξ defined as:

$$\xi = -\frac{1}{k_0}\sqrt{\frac{2n_0^2}{\chi^{(3)}|E_0|^2}}. \tag{4.44}$$

For $\mathbf{k}_\perp \gg 1/\xi$, we have a parabolic dispersion. For $\mathbf{k}_\perp \ll 1/\xi$ we observe a sonic dispersion with a speed of sound c_s defined as:

$$c_s = \sqrt{-\frac{\chi^{(3)}|E_0|^2}{2n_0^2}}. \tag{4.45}$$

Measure of the Bogoliubov dispersion

So far, I have shown theoretically that we can consider the propagation in a $\chi^{(3)}$ analogue to the dynamic of a Bose gas in 2D [2]. We have recently pushed forward this effort with the experimental verification of this proposal. Using the vocabulary of Bose gases, in this context, offers modern perspectives on non–linear and quantum optics experiments.

To date, experimental implementations are still in their infancy with experiments in photo–refractive crystals [95, 96, 97], and thermo-optic non–linear medium [98]. In a non-local $\chi^{(3)}$ thermo-optic medium (methanol), the Bogoliubov dispersion of a fluid of light has been studied [98] and indication of superfluid behaviour has been observed [99]. Similarly, an iodine solution has been used to create an event horizon in light fluid acoustic black hole analogue [100]. Even though these results highlight the potential of the quantum fluid interpretation, the non-locality of these media (thermo-optic non-linearity is affected by heat diffusion) is detrimental for simulating system with local interactions. By using warm atomic vapors as $\chi^{(3)}$ medium we have access to tunable and local interactions. Interestingly, a few works on the elimination of diffraction in a slow light atomic medium [101, 102], are using similar ideas without explicitly connecting to fluid of light.

In our implementation, we use the following protocol:

- We create a uniform background fluid with a pump laser propagating in a near resonance atomic vapor.
- We add a small perturbation by interfering a localize probe beam at the same frequency at an angle with respect to the background wavevector.
- We study the propagation of this perturbation by measuring the distance propagated in the transverse plane by these narrow wavepackets at the end of the medium.
- From this measurement of the group velocity, we simply integrate with respect to the wavevector and obtain the dispersion relation.

We have obtained a dispersion fitting a Bogoliubov spectrum confirming the theoretical prediction. For more details the results are presented in the article attached. I just add two comments (please read the paper first): one to provide an intuitive explanation of this surprising effect and the second to connect this effect to four-wave-mixing.

Anomalous refraction In our experiment [1] the refraction law is indeed strongly modified compared to the linear case of Snell law (See figure 4.6). It is well known that imaging inside a non-linear medium is not a recommended task for this reason. What I want to show here, is that the quantum fluid language provide an intuitive vision of this phenomenon. For small angles ($\mathbf{k}_\perp < \xi$), the probe beam light emerges always at the same place in the output plan independently of the angle. This is strange because changing the incident angle

[2] A fully quantum theoretical framework for fluids of light in the same configuration has been recently proposed [94].

should normally change the refracted angle. This invariance is understood in the fluid context as a simple consequence of the constant group velocity or similarly of the linear dispersion. Moreover, the probe position in the output plane depends on the pump intensity. Again, if one thinks in terms of fluids, it modifies the speed of sound and therefore the position in the output plane.

For larger angle ($\mathbf{k}_\perp \gg \xi$), we found again a more usual behaviour with the position of the beam at the output directly linked to the incident angle. We are in the limit of parabolic dispersion, which means that the group velocity is proportional to $\mathbf{k}_\perp$ and therefore the position in the output plane ($z = L$) is $\mathbf{k}_\perp L$. We can switch back to a simple geometric explanation as long as we stay in the paraxial approximation. Coming with this explanation using only the non-linear optics phenomenon is not possible, especially the means to estimate the angle where the two regimes changes (ξ). This is one of the strength of fluid of light language: to be able to bring new tools to explain non-linear and quantum optics experiment.

Four-wave-mixing This experiment is "nothing else than" degenerate four-wave-mixing. One takes two photons from the pump and transfers one to the probe and one to the conjugate. However, we need to be careful when using this vocabulary. What the fluid of light language taught us, is that inside the medium we should not talk about probe and conjugate but more precisely about two Bogoliubov modes u_q and v_q propagating at $+\mathbf{q}$ and $-\mathbf{q}$ (using the notation of 4.31). The most striking case is when $\mathbf{k}_\perp = 0$. In this situation of colinear four-wave-mixing, probe and conjugate are at $\mathbf{k}_\perp = 0$, however we still have two Bogoliubov modes at $+\mathbf{q}$ and $-\mathbf{q}$ inside the medium as demonstrated by imaging the output (see figure 4.6).

Probe and conjugate, as commonly use in four-wave-mixing, are actually far field denomination only. What I present in the figure 4.6, is the incident probe beam, which splits in pairs of mode at $+\mathbf{q}$ and $-\mathbf{q}$ inside the medium forming a ring. After the medium, all these modes will combine and contribute to create a probe and a conjugate at $+\mathbf{k}_\perp$ and $-\mathbf{k}_\perp$ in the far field. There is no reason, in general, for $\mathbf{k}_\perp$ and $\mathbf{q}$ to be the same. When, we inject at mode at $\mathbf{k}_\perp \neq 0$, we break the symmetry between for the ring of Bogoliubov modes. In the far field we observed a difference in intensity between probe and conjugate which is known in non-linear optics as phase matching. We note that if the probe and pump have different frequency the phase matching condition would not be at $k_\perp = 0$ anymore as in chapter 3.

An important prediction from the Bose gases physics is that the creation of Bogoliubov modes results from a quench: a sudden (non-adiabatic) change of one parameter of the system. Here, the interactions appears suddenly at the medium input. What this prediction tells us is that four-wave-mixing should not occur if we were able to ramp adiabatically the interactions. This interesting (and surprising) prediction remains to be verified experimentally.

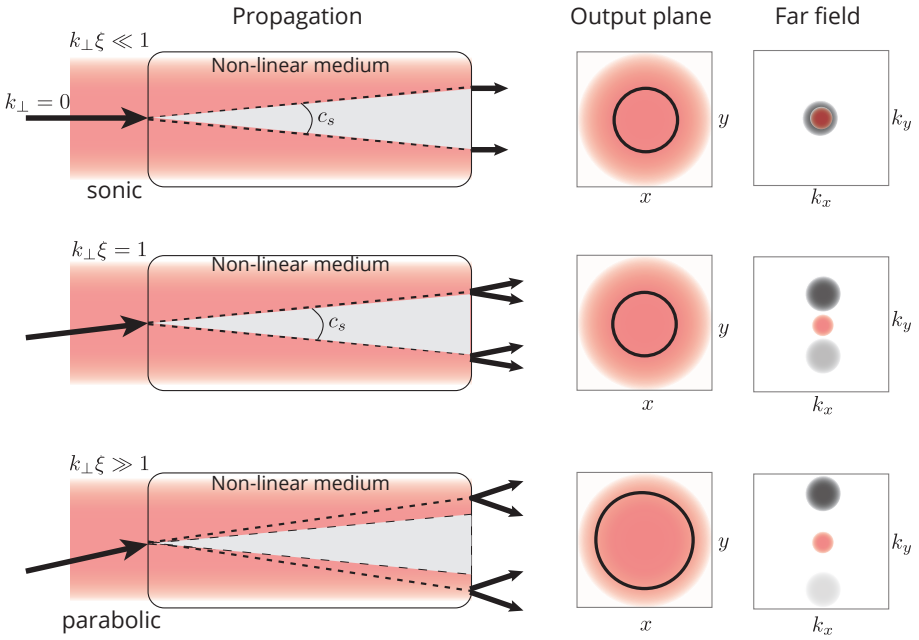

Figure 4.6: I represent here three limit cases for the propagation of a weak probe in a non-linear medium. On the first line I draw the case $\mathbf{k}_\perp = 0$. We can see that even for $\mathbf{k}_\perp = 0$, the Bogoliubov excitations (in dashed lines inside the medium) propagate at a finite speed c_s. If we increase the incident angle ($\mathbf{k}_\perp$) while staying in the limit $\mathbf{k}_\perp < 1/\xi$ the ring in the output plane does not change as the Bogoliubov modes always propagate at c_s (shown on the second line). If we break this condition $\mathbf{k}_\perp \gg 1/\xi$, Bogoliubov excitations behave like free particles and therefore an increasing $\mathbf{k}_\perp$ results in an increasing diameter of the ring (shown on the bottom line) At the output of the medium two modes are emitted to the far field at $\mathbf{k}_\perp$ and $-\mathbf{k}_\perp$. These modes are usually called probe and conjugate in the language of four-wave-mixing. Due to phase matching condition, increasing $\mathbf{k}_\perp$ lead to a reduction of the power in the $-\mathbf{k}_\perp$ mode.

Editors' Suggestion

Observation of the Bogoliubov Dispersion in a Fluid of Light

Q. Fontaine, T. Bienaimé, S. Pigeon, E. Giacobino, A. Bramati, and Q. Glorieux*
Laboratoire Kastler Brossel, Sorbonne Université, CNRS, ENS-PSL Research University, Collège de France, Paris 75005, France

(Received 30 July 2018; published 31 October 2018)

Quantum fluids of light are a photonic counterpart to atomic Bose gases and are attracting increasing interest for probing many-body physics quantum phenomena such as superfluidity. Two different configurations are commonly used: the confined geometry where a nonlinear material is fixed inside an optical cavity and the propagating geometry where the propagation direction plays the role of an effective time for the system. The observation of the dispersion relation for elementary excitations in a photon fluid has proved to be a difficult task in both configurations with few experimental realizations. Here, we propose and implement a general method for measuring the excitations spectrum in a fluid of light, based on a group velocity measurement. We observe a Bogoliubov-like dispersion with a speed of sound scaling as the square root of the fluid density. This Letter demonstrates that a nonlinear system based on an atomic vapor pumped near resonance is a versatile and highly tunable platform to study quantum fluids of light.

DOI: 10.1103/PhysRevLett.121.183604

Superfluidity is one of the most striking manifestations of quantum many-body physics. Initially observed in liquid helium [1,2], the realization of atomic Bose-Einstein condensates (BECs) has allowed detailed investigations of this macroscopic quantum phenomenon, exploiting the precise control over the system parameters. Recently, another kind of quantum fluid made of interacting photons in a nonlinear cavity has brought new perspectives to the study of superfluidity in driven-dissipative systems, with many fascinating developments [3] such as the observation of polariton BECs [4,5] and the demonstration of exciton-polariton superfluidity [6,7]. A different photon fluid configuration, initially proposed by Frisch *et al.* 20 years ago [8], but long ignored experimentally, relies on the propagation of a intense laser beam through some nonlinear medium. In this $2D+1$ geometry (two transverse spatial dimensions and one propagation dimension analogous to an effective time), the negative third-order Kerr nonlinearity is interpreted as a photon-photon repulsive interaction. Few theoretical works addressing mostly hydrodynamic effects using this geometry have been recently proposed [9,10] and investigated in photorefractive crystals [11], thermo-optic media [12,13], and hot atomic vapors [14].

The theoretical framework used to describe quantum fluids of light relies on the analogy with weakly interacting Bose gases and was originally derived by Bogoliubov [15,16]. A fundamental property of the Bogoliubov dispersion relation is the linear dependence in the excitation wave vector at long wavelengths (soundlike) and the quadratic dependence at short wavelengths (free particle-like). Although this dispersion has been well characterized in atomic BEC experiments [17–20], a direct measurement of this dispersion in a fluid of light remains elusive [12,21]. In this Letter, we propose a general method to experimentally access the dispersion of elementary density excitations of a photon fluid. We show that the dynamics of these excitations is governed by a Bogoliubov-like dispersion and that our experimental platform, based on light propagation in hot atomic vapor, is promising to study hydrodynamics effects emerging in fluid of light systems. Our experiment settles the question originally asked by Chiao two decades ago [22]: can one observe soundlike excitations and superfluidity of light?

Even if photons in free space are essentially noninteracting particles, engineering an effective photon-photon interaction is possible by exploiting an optical nonlinear process. In our experiment, the third-order Kerr nonlinearity is induced by the propagation of a near-resonant laser field inside a hot Rubidium atomic vapor. The sign and the strength of the interactions can be finely tuned by adjusting the laser detuning with respect to the atomic resonance. The vapor temperature, controlling the atomic density, provides an additional control over the strength of the interactions. This system has been extensively studied in the context of quantum and nonlinear optics [23], but the quantum fluid of light framework gives a better and more complete understanding about the physical phenomena discussed in this Letter. This framework is derived from the nonlinear Schrödinger equation (NLSE), describing the propagation along the z direction of a monochromatic linearly polarized laser field $E(\mathbf{r}_\perp, z)$ in a nonlinear medium, under the paraxial approximation

$$i\frac{\partial E}{\partial z} = -\frac{1}{2k_0}\nabla_\perp^2 E - \left(k_0 n_2 |E|^2 + i\frac{\alpha}{2}\right)E, \qquad (1)$$

 © 2018 American Physical Society

where $k_0 = 2\pi/\lambda_0$ is the laser wave vector (λ_0 stands for the laser wavelength in vacuum), and $\nabla_\perp$ is the gradient with respect to the transverse spatial coordinate $\mathbf{r}_\perp = (x, y)$. When the linear absorption coefficient α is negligible and the nonlinear refractive index $\Delta n = n_2|E|^2 = \frac{2}{\epsilon_0 c} n_2 I = \tilde{n}_2 I$ (I represents the laser field intensity) is negative, the NLSE is mathematically analogous to the Gross-Pitaevski equation, describing the dynamics with respect to an effective time $t = z n_0/c$ (c stands for the speed of light in vacuum) of a 2D fluid with repulsive interactions. Using the Madelung transformation $E(\mathbf{r}_\perp, z) = \sqrt{\rho(r_\perp, z)}\exp[i\Phi(r_\perp, z)]$, one obtains a coupled system of hydrodynamic equations for the electric field density ρ and phase Φ,

$$\frac{\partial \rho}{\partial t} + \boldsymbol{\nabla}_\perp \cdot (\rho \mathbf{v}) = 0, \tag{2}$$

$$\frac{c}{k_0}\frac{\partial \Phi}{\partial t} + \frac{1}{2}v^2 + c^2\left(n_2\rho - \frac{1}{2k_0^2}\frac{\nabla_\perp^2\sqrt{\rho}}{\sqrt{\rho}}\right) = 0, \tag{3}$$

where $\mathbf{v} = (c/k_0)\boldsymbol{\nabla}_\perp\Phi$. In this formulation, the laser beam is described as a fluid of density ρ flowing with velocity $\mathbf{v}$ in the transverse plane. The dynamics of the density fluctuations on top of the photon fluid is governed by the Bogoliubov dispersion relation. For small amplitude modulations moving on a uniform background fluid at rest, the set of hydrodynamic equations can be linearized assuming $\rho = \rho_0(z) + \delta\rho(\mathbf{r}_\perp, z)$ and $\mathbf{v} = \delta\mathbf{v}(\mathbf{r}_\perp, z)$. For a plane wave density fluctuation mode $\delta\rho$ of wave vector $\mathbf{k}_\perp$, the associated response frequency Ω_B will follow the dispersion relation below,

$$\Omega_B(\mathbf{k}_\perp) = c\sqrt{|\Delta n|\mathbf{k}_\perp^2 + \left(\frac{\mathbf{k}_\perp^2}{2k_0}\right)^2}. \tag{4}$$

When the wavelength $\Lambda = 2\pi/|\mathbf{k}_\perp|$ of the modulation is longer than the *healing length* $\xi = (\lambda/2)\sqrt{[1/(|\Delta n|)]}$, the dispersion relation becomes linear and the modulations propagate as sound waves. This regime is characterized by the sound velocity $c_s = c\sqrt{|\Delta n|}$, which only depends on the nonlinear index of refraction Δn. Conversely, when $\Lambda \gg \xi$, the dispersion relation becomes quadratic, which is similar to the free propagating particle one.

Observing the soundlike regime of the Bogoliubov dispersion relation has been proposed in [9] and was first attempted in [12] for propagating geometries. The approach used in [12] relies on the measurement of the phase velocity difference between plane wave density modulations propagating at a given transverse wave vector $k_\perp = 2\pi/\Lambda$ on top of a high and a low density photon fluid. The photon fluid is obtained by sending a wide laser beam through a self-defocusing nonlinear medium; the fluid density is then given by the light intensity. The plane wave density modulation is produced by interfering this first beam with a wide and weak probe field, propagating with a small angle with respect to the optical axis. In this configuration, however, a *conjugate* wave propagating in the opposite transverse direction ($-\mathbf{k}_\perp$) is spontaneously generated at the linear-nonlinear interface [24]. Probe and conjugate interfere, which strongly alters the phase shift measurement used to determine the dispersion relation. Moreover, the large nonlinearity needed to observe the sonic dispersion makes extracting the dispersion relation from this measurement rely on a complex numerical inversion [25]. On the contrary, we present a direct and intuitive method to extract the dispersion relation for arbitrary modulation wavelengths. Our approach is based on the measurement of the group velocity of a small amplitude Gaussian wave packet traveling on top of the photon fluid with the transverse wave vector $k_\perp$. This wave packet is designed by interfering a wide and intense beam forming the fluid (at $\mathbf{k}_\perp = \mathbf{0}$) with a Gaussian probe at $\mathbf{k}_\perp = k_0 \sin\theta \mathbf{e}_x$, as depicted in Fig. 1. At the entrance of the nonlinear medium, the effective photon-photon interaction constant undergoes a sudden jump along the optical axis. Two counterpropagating wave packets are spontaneously created from the initial perturbation and evolve over the effective time t through the nonlinear medium, with a transverse group velocity $\pm v_g$. The separation between these two modulations at a given propagation distance z (i.e., at given time t),

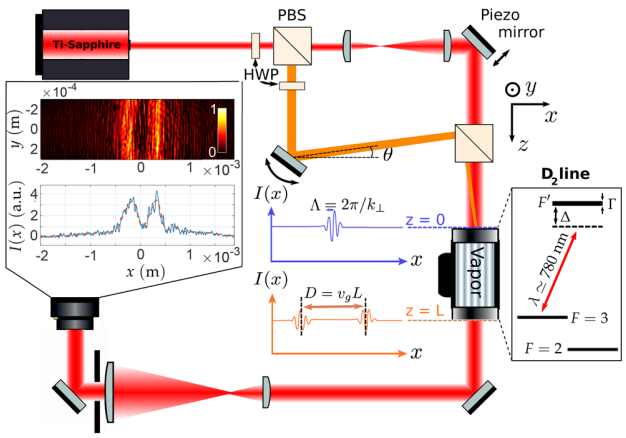

FIG. 1. Experimental setup: polarized beam splitter (PBS) and half wave plate (HWP). θ is the angle between the probe (orange beam) and the optical axis defined by the pump (red beam). The probe interferes with the pump and slightly modulates its intensity. (Blue inset) Integrated intensity profile at the input of the medium ($z = 0$). The wavelength Λ of the density modulation is given by $2\pi/k_\perp$, where $k_\perp = k_0 \sin\theta$. (Orange inset) Integrated intensity profile at the output of the medium ($z = L$). The distance D between the two wave packets gives access to the group velocity of the elementary excitations in the transverse plane. The output plane is imaged on a CMOS camera. (Inset, top left) Background-subtracted image obtained for $\theta \approx 0$ rad and associated integrated envelope profile (blue: original; red dotted: high frequency filtered).

is a direct measurement of the group velocity. In the output plane ($z = L$), this distance is given by $D(k_\perp) = 2Lv_g(k_\perp)$. The dispersion relation $\Omega_B(k_\perp)$ is reconstructed by scanning the modulation wave vector (tuning the angle θ between pump and probe) and integrating the group velocity v_g: $\Omega_B(k_\perp) = \int_0^{k_\perp} v_g(q)dq$.

In order to illustrate our method, we solve numerically the NLSE [Eq. (1)] to get the evolution of the transverse electric field (pump + probe). We use the second-order split step Fourier method, for one transverse spatial dimension (1D + 1 geometry) to take advantage of symmetries in the flat fluid density situation (infinitely wide background beam). The probe waist is located in the entrance plane at $z = 0$; its width ω_x^p is the same as the one used in the experiment. For all the density plots in Fig. 2, the uniform background intensity has been subtracted. The evolution of the two counterpropagative modulations generated at the entrance of the nonlinear medium is shown in Fig. 2(a) for zero initial transverse speed and presents a soundlike behavior (no spreading of the wave packet). Figure 2(b) is obtained for high transverse initial speed modulation, which behaves like a free particle. Notice that, for small incident angle, corresponding to zero initial transverse speed, both modulations acquire a nonzero opposite transverse speed. This nonlinear refraction law, counterintuitive from the refraction perspective, comes from the linear nature of the dispersion for $k_\perp \ll 2\pi/\xi$ [24]. The envelope of the intensity profile in the output plane is presented as a function of the probe wave vector in Fig. 2(c), on top of the experimental results in Fig. 2(d). The black dotted line represents the theoretical group velocity v_g, obtained by taking the derivative of Eq. (4). The distance between the two wave packets is constant for $k_\perp \lesssim 2\pi/\xi$ (linear dispersion; constant v_g) and linearly increase for larger $k_\perp$ (quadratic dispersion; $v_g \propto k_\perp$). The spreading of the wave packet due to the quadratic dispersion for $k_\perp \gtrsim 2\pi/\xi$ can also be clearly observed in Fig. 2(c). Conversely, all k space components that lie on the linear part of the dispersion relation propagate at the same transverse speed and the wave packets do not spread for $k_\perp < 2\pi/\xi$.

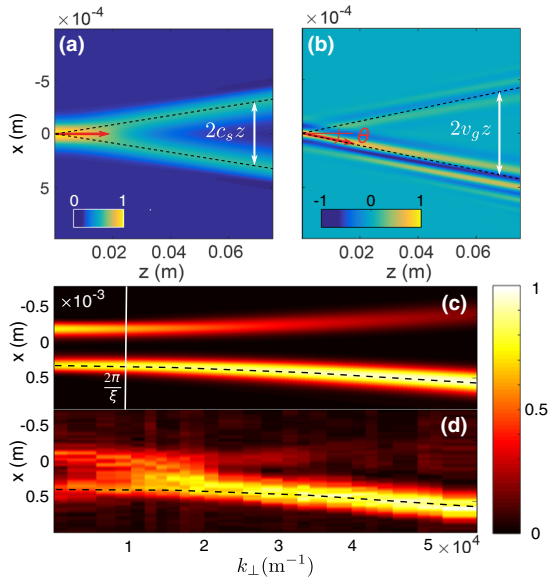

FIG. 2. (a) Simulation of the propagation of a weak intensity modulation through a nonlinear medium, with zero transverse speed ($\theta = 0$ rad). The modulation generates two counterpropagating Bogoliubov modes at the medium interface that get amplified until they separate from each other. The wave packet is not spreading along propagation due to the nondispersive regime (soundlike behavior). (b) Same as (a), for an incident probe at $\theta = 5 \times 10^{-3}$ rad (high transverse speed). Interference fringes appear and the wave packet spreads. (c) Simulation of the intensity profile envelope in the output plane for different probe wave vector. (Dashed black lines) Group velocity given by Eq. (4). (d) Experimental data. The upper wave packet amplitude decreases with $k_\perp$, as the efficiency of the degenerate four-wave mixing processes depends on the phase matching conditions, which is optimal for $k_\perp = 0$. The parameters in (a)–(c) are those used experimentally for (d): $\lambda_0 = 780$ nm, $\Delta n = 1.3 \times 10^{-5}$, and $\omega_x^p = 180$ μm ($\alpha = 0$ in numerical simulations).

The experimental setup is shown in Fig. 1. A continuous-wave Ti:Sapphire laser beam is split into a low power probe and a high power pump. The pump is focused in the center of the nonlinear medium with two cylindrical lenses to create an elliptical beam with a width along x of $\omega_x^0 \approx 3.2$ mm and a width along y of $\omega_y^0 \approx 300$ μm. The pump intensity in the central region can thus be considered as spatially uniform along x. The Rayleigh length $z_{R,y}^0$ associated with ω_y^0 is 37 cm, which is about 5 times the length of the nonlinear medium. We can therefore consider the pump beam as being collimated. The probe is directly focused with a cylindrical lens on the entrance of the nonlinear medium in order to get a flat initial phase profile. This beam is elliptically elongated along the y direction. We set the major axis width ω_y^p to 1700 μm and ω_x^p to 180 ± 10 μm in order to properly separate the Gaussian wave packets in the output plane and conserve the probe collimation along its propagation in the nonlinear medium ($z_{R,x}^p \approx 13$ cm). We fix the probe intensity at its waist to 1% of the pump intensity. This pump-probe cross configuration enables us to both get closer to the 1D case and to increase the integration range along y. The angle θ between pump and probe in the (xz) plane can be finely tuned with a piezoactuated mirror mount.

Both beams propagate through a $L = 7.5$ cm long cell, filled with an isotopically pure ^{85}Rb vapor. The cell is heated up to 150 °C. Adjusting the temperature allows us to control the atomic density and therefore the strength of the optical nonlinearity. In our case, this optical nonlinearity is obtained by tuning the laser frequency close to the ^{85}Rb D_2 resonance line, composed of two hyperfine ground states ($F = 2$, 3) and four hyperfine excited states ($F' = 1$–4).

Since the laser is highly red detuned from the $F = 3 \rightarrow F'$ transitions ($\Delta = -6$ GHz), the Doppler broadening can be neglected and the negative nonlinear susceptibility is one of a two-level system with an excited state of decay rate $\Gamma = 6.06$ MHz. At this temperature and detuning, the transmission coefficient of the laser beams through the cell is above 70%, which allows one to neglect multiple scattering of light. In comparison to [12], we can consider that the nonlinear interactions are local, as long as the length scale of the ballistic transport of excited atoms stays much shorter than the healing length, which is the case at that temperature.

The output plane of the cell is imaged on a camera. A microscope objective can be flipped on the beam path to image the far field (i.e., k space) and measure the probe transverse wave vector $k_\perp = k_0 \sin\theta$. The relative phase between pump and probe is scanned over 2π. Forty background-subtracted images are taken during the phase scan, integrated over 100 pixels around (Ox) and averaged in absolute values. Averaged images before integration are shown in the inset of Fig. 1(b). The distance D between the counterpropagating wave packets is estimated by performing a two-Gaussian fit for small $k_\perp$, i.e., when the conjugate beam is visible. For large $k_\perp$, the conjugate is not sufficiently amplified and D is measured from the distance between the input and output positions of the probe beam. In order to fully characterize our system, the third-order Kerr susceptibility n_2 is calibrated independently by measuring the self-phase accumulated by a Gaussian beam propagating through the cell [26,27]. With the detuning and temperature reported earlier, we found $\tilde{n}_2 = 3.1 \pm 0.2 \times 10^{-11}$ m^2/W.

The experimental group velocity and dispersion relation as a function of the probe transverse wave vector are shown in Fig. 3. The pump power was set to 175 mW, leading to a nonlinear refractive index Δn of 3.9×10^{-6}. Two different regimes can be identified in Fig. 3(a). The group velocity clearly goes toward a nonzero value when $k_\perp \rightarrow 0$, breaking the linear trend characteristic of the standard free-particle dispersion. The theoretical model plotted in Fig. 3 is obtained with no free fitting parameters. The offset at large $k_\perp$ between the model and the experimental data results from constructive interferences between the two nonfully separated wave packets, as can be seen by the experimental data of Fig. 2(d) around $k_\perp \sim 1.5 \times 10^4$ m^{-1} (the envelope intensity significantly increases in between them, leading to a systematic underestimation of the distance D by the two-Gaussian fit). After propagation in the cell, the counterpropagating wave packets have respectively accumulated the phase $\pm\Omega_B(k_\perp)L$. Constructive interferences occur when $\Omega_B(k_\perp)L = n\pi$ (n is a positive integer), i.e., for $k_\perp \sim 1.8 \times 10^4$ m^{-1} when $n = 1$. This value gives the position of the end of the plateaulike regime at low $k_\perp$. Another constructive interference should occur for $k_\perp = 0$ (when $n = 0$), but as both envelopes have the same amplitude in that case, the two peaks are still disentangled (see inset of Fig. 1).

More importantly, the dispersion relation of Fig. 3(b) guarantees that, in our experiment, a fluid of light can fulfill

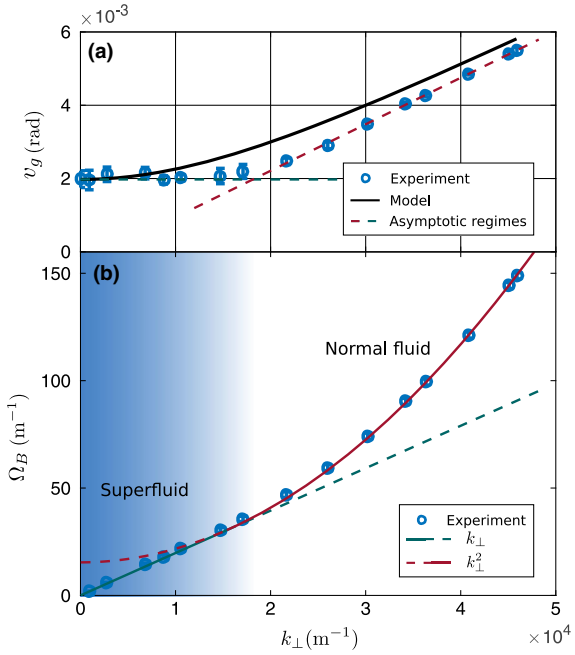

FIG. 3. (a) Group velocity as a function of $k_\perp$. The circles represent the experimental data obtained for $P = 175$ mW. The theoretical model is plotted in black (no free parameter—see text for details). The dashed lines figure the asymptotic behaviors: constant group velocity at small $k_\perp$ and linear increase at large $k_\perp$. (b) Dispersion relation obtained after integration of the group velocity. Linear (blue) and parabolic (red) dispersion curves are plotted as a reference.

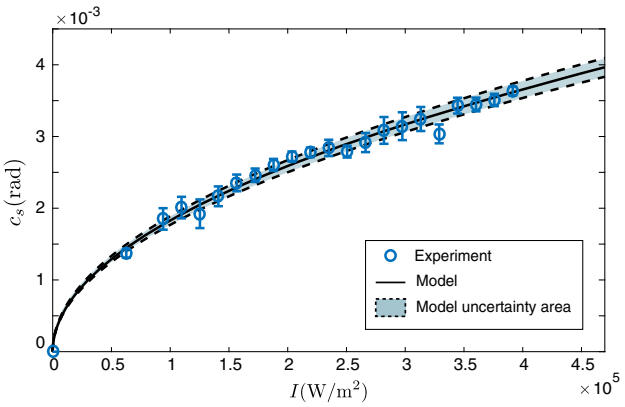

FIG. 4. Speed of sound c_s as a function of the pump intensity. Because of the 2D + 1 geometry, the speed of sound has the dimension of an angle. Data are plotted in blue dots. The light intensity corresponds to the fluid density; therefore, a scaling as a square root is expected as plotted in black solid. No free parameters are needed, as the nonlinearity has been measured independently. Uncertainty area in light blue is extracted from this independent measurement.

the Landau criterion for superfluidity. Indeed, this criteria defines a critical transverse speed $v_c = \min_{k_\perp}[\Omega_B/k_\perp]$ for the photon fluid, below which the emission of soundlike excitations is not possible anymore. In our case, $v_c = c_s > 0$ and one could observe frictionless flow of light around a defect if its transverse velocity v (measured in the defect frame) was lower than c_s. Nevertheless, our system does not undergo a phase transition with the sudden appearance of a long-range order, as it is initially provided by the laser spatial coherence. To investigate the sonic regime, we set the probe wave vector to zero and record the sound velocity as function of the background fluid density (the pump intensity I). The experimental data are shown in Fig. 4 (blue circles). We observe that the speed of sound scales with the square root of the fluid density (black solid) as expected. It is worth mentioning that, once again, the Kerr susceptibility measured independently sets the only parameter of the theoretical model.

In conclusion, we have reported two important experimental results: First, we measured the dispersion relation for small amplitude density fluctuations, which shows a linear trend at low wave vector, characteristic of a superfluid. We have then assessed the associated sound velocity for different fluid of light densities and obtained a scaling law analogous to the hydrodynamic prediction. This settles the question initially raised by Chiao about the possibility to observe a superfluid dispersion in a photon fluid. These results open a wide range of possible experiments in hydrodynamics with light using a novel versatile platform based on hot atomic vapors.

The authors want to thank Daniele Faccio for stimulating discussions at the early stage of the project, Iacopo Carusotto, Pierre-Elie Larré, and Giovanni Lerario for important remarks on the physics of Bose gases and superfluidity. This work has been supported by the CFlight ANR.

*Corresponding author.
quentin.glorieux@sorbonne-universite.fr

[1] P. Kapitza, Nature (London) **141**, 74 (1938).
[2] J. F. Allen and A. D. Misener, Nature (London) **141**, 75 (1938).
[3] T. Byrnes, N. Y. Kim, and Y. Yamamoto, Nat. Phys. **10**, 803 (2014).
[4] R. Balili, V. Hartwell, D. Snoke, L. Pfeiffer, and K. West, Science **316**, 1007 (2007).
[5] J. Kasprzak, M. Richard, S. Kundermann, A. Baas, P. Jeambrun, J. M. J. Keeling, F. M. Marchetti, M. H. Szymańska, R. André, J. L. Staehli, V. Savona, P. B. Littlewood, B. Deveaud, and L. S. Dang, Nature (London) **443**, 409 (2006).
[6] A. Amo, J. Lefrère, S. Pigeon, C. Adrados, C. Ciuti, I. Carusotto, R. Houdré, E. Giacobino, and A. Bramati, Nat. Phys. **5**, 805 (2009).
[7] G. Lerario, A. Fieramosca, F. Barachati, D. Ballarini, K. S. Daskalakis, L. Dominici, M. De Giorgi, S. A. Maier, G. Gigli, S. Kéna-Cohen *et al.*, Nat. Phys. **13**, 837 (2017).
[8] T. Frisch, Y. Pomeau, and S. Rica, Phys. Rev. Lett. **69**, 1644 (1992).
[9] I. Carusotto, Proc. R. Soc. A, DOI: 10.1098/rspa.2014.0320 (2014).
[10] P.-E. Larré and I. Carusotto, Phys. Rev. A **91**, 053809 (2015).
[11] C. Michel, O. Boughdad, M. Albert, P.-É. Larré, and M. Bellec, Nat. Commun. **9**, 2108 (2018).
[12] D. Vocke, T. Roger, F. Marino, E. M. Wright, I. Carusotto, M. Clerici, and D. Faccio, Optica **2**, 484 (2015).
[13] D. Vocke, K. Wilson, F. Marino, I. Carusotto, E. M. Wright, T. Roger, B. P. Anderson, P. Öhberg, and D. Faccio, Phys. Rev. A **94**, 013849 (2016).
[14] N. Šantić, A. Fusaro, S. Salem, J. Garnier, A. Picozzi, and R. Kaiser, Phys. Rev. Lett. **120**, 055301 (2018).
[15] N. N. Bogoliubov, Izv. Akad. Nauk SSSR, Ser. Fiz. **11**, 77 (1947) [Bull. Acad. Sci. USSR, Phys. Ser. **11**, 23 (1947)].
[16] V. Kohnle, Y. Léger, M. Wouters, M. Richard, M. T. Portella-Oberli, and B. Deveaud-Plédran, Phys. Rev. Lett. **106**, 255302 (2011).
[17] D. S. Jin, J. R. Ensher, M. R. Matthews, C. E. Wieman, and E. A. Cornell, Phys. Rev. Lett. **77**, 420 (1996).
[18] M.-O. Mewes, M. R. Andrews, N. J. van Druten, D. M. Kurn, D. S. Durfee, C. G. Townsend, and W. Ketterle, Phys. Rev. Lett. **77**, 988 (1996).
[19] R. Onofrio, C. Raman, J. M. Vogels, J. R. Abo-Shaeer, A. P. Chikkatur, and W. Ketterle, Phys. Rev. Lett. **85**, 2228 (2000).
[20] J. Steinhauer, R. Ozeri, N. Katz, and N. Davidson, Phys. Rev. Lett. **88**, 120407 (2002).
[21] S. Utsunomiya, L. Tian, G. Roumpos, C. Lai, N. Kumada, T. Fujisawa, M. Kuwata-Gonokami, A. Löffler, S. Höfling, A. Forchel *et al.*, Nat. Phys. **4**, 700 (2008).
[22] R. Y. Chiao, Opt. Commun. **179**, 157 (2000).
[23] Q. Glorieux, R. Dubessy, S. Guibal, L. Guidoni, J.-P. Likforman, T. Coudreau, and E. Arimondo, Phys. Rev. A **82**, 033819 (2010).
[24] P.-E. Larré and I. Carusotto, Phys. Rev. A **92**, 043802 (2015).
[25] P.-É. Larré, S. Biasi, F. Ramiro-Manzano, L. Pavesi, and I. Carusotto, Eur. Phys. J. D **71**, 146 (2017).
[26] C. M. Nascimento, M. A. R. C. Alencar, S. Chávez-Cerda, M. G. A. da Silva, M. R. Meneghetti, and J. M. Hickmann, J. Opt. A **8**, 947 (2006).
[27] Y. Zhang, X. Cheng, X. Yin, J. Bai, P. Zhao, and Z. Ren, Opt. Express **23**, 5468 (2015).

Chapter 5

Outlooks and future projects

In this work we have travelled through several implementations of light-matter interaction experiments from the generation of squeezed light in four-wave-mixing to the storage of light in an atomic vapor. The future projects I want to develop are along the line of combining quantum optics and quantum memory with the concept of fluids of light. Indeed,the experimental realizations of fluid of light presented in this manuscript are based on the Bogoliubov mean-field theory. An important leap forward in this field will consist in bridging the gap with quantum optics type measurements such as intensity noise, homodyne detection or entanglement. In this chapter I give a (partial) overview of the essential ideas we will explore in the coming years.

5.1 Fluid of light in the propagating geometry

5.1.1 Shockwaves dynamics in 1D and 2D Collaboration with N. Pavloff and A. Kamchatnov

Before exploring the quantum world with fluids of light, some highly interesting experiments are still to be conducted in the classical regime. One of them is focused on the generation of shockwaves in a fluid of light. Shockwaves appear when the Bogoliubov approximation of a small perturbation propagating in a fluid breaks down. Pioneering work about shockwaves in optics has been done by the Fleischer's group in photo-refractive crystal. Recently, we have started a collaboration with the group of Nicolas Pavloff in LPTMS to explore this field in detail and to understand the role of the geometry (1D and 2D) in shockwaves propagation.
The setup is identical to the setup used for Bogoliubov dispersion in chapter 4, however in this case, the magnitude of the perturbation is as large as the mean density. We have studied the dynamic of the shock propagation for 3 characteristic points of the shockwave (see Fig. 5.1):

- Point 1: the beginning of the linear slope
- Point 2: the maximum
- Point 3: the first minimum of the shockwave oscillations

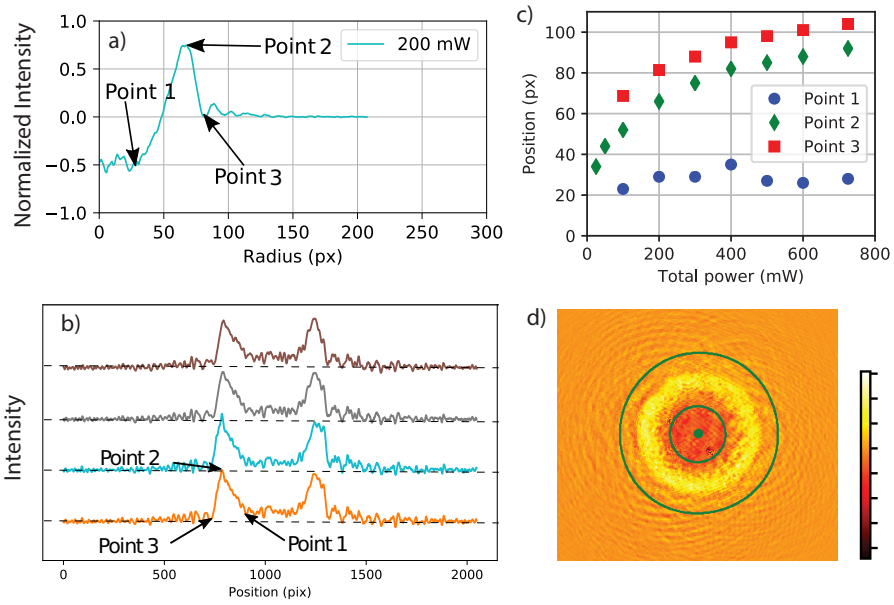

Figure 5.1: Preliminary results on shockwaves. a) 2D shock profile. Intensity is normalized to 0 far away from the shock. The negative value in the center is characteristic of 2D shockwaves. b) 1D configuration for various intensity. c) Scaling of points 1,2 and 3 as function of power. d) Typical intensity image.

The work in progress we are conducting with Nicolas Pavloff is to find theoretically a universal exponent for the propagation velocity of each of these three points and to verify it experimentally. It is understood that these exponents should vary strongly depending on the dimensionality of the system. Our implementation is intrinsically 2D (in the transverse plane) however, we can also explore 1D physics by making the system much longer in one direction (virtually infinite) and therefore invariant along this dimension.

A major difference between 1D and 2D for shockwaves consists in the prediction of the density in the center after the shock front has passed. In 1D the density of the fluid (here the intensity of light) should go back to average fluid density immediately after the shock front has passed, while for 2D (and 3D) the density should remain lower than the average density. This effect is well known in fluid dynamics and has an immediate consequence when for example an explosion occurs inside a building. Indeed, when shockwaves due to the explosion reach a window, glass breaks and falls inside the building and not outside, a consequence of the lower density inside following the shock front. We have reproduced this effect with light and observed a reduction of the density after the shock in 2D and no reduction in 1D as seen in figure 5.1a.

5.1.2 Superfluid flow around a defect Collaboration with C. Michel and M. Bellec

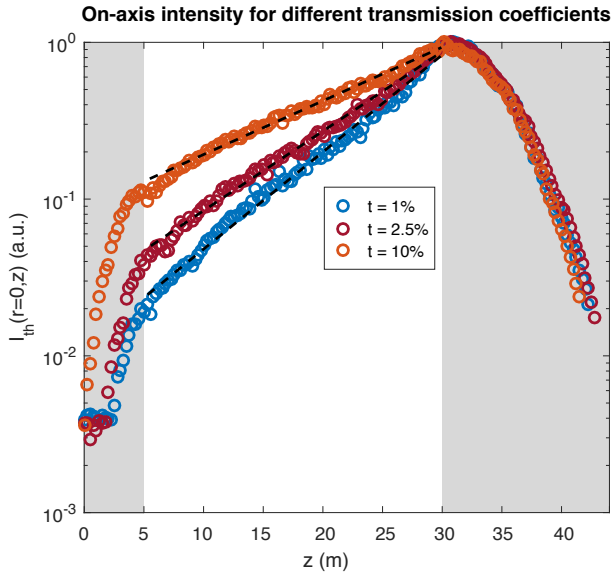

Figure 5.2: On axis intensity of a Bessel beam shaped to have an exponential increase along the propagation. Various attenuation coefficients are used. The dashed lines are the fits with linear slopes in log-scale. The region where the intensity is designed to follow an exponential increase is shown in white.

We have recently observed the Bogoliubov dispersion for light propagating into an atomic medium. The linear part of this dispersion is, following Landau criteria, an indication of possible superfluid flow. The smoking gun of superfluidity is the observation of Rayleigh scattering cancellation when the fluid hits a defect as seen in figure 4.2 for a polariton fluid. To settle our platform, based on light propagating through atomic vapor, as a realistic alternative to the study of superfluidity, we need to perform a similar experiment [103].

The defect here should be a refractive index change around the mean value as described in Eq. 4.41. As we want the defect to be constant in (effective) time, one needs to make it constant in the (real) space along the propagation direction. Local modifications of the refractive index can be created optically by designing spatially dependant optical pumping. Experimentally, this requires an external defect beam, tuned near resonance, which propagates with constant shape and amplitude through the atomic medium. This seems a difficult task, but works in progress in my group have shown this to be achievable. Two steps have to be considered.

The first step is the design of a non-diffracting beam. Bessel beams can be created using an optical axicon or with more control using a spatial light modulator. A distance of 10 cm for a beam size of 50 μm is achievable at 800 nm, to be compared to a Rayleigh length of 9 mm for a Gaussian beam of the same size.

The second stage is the control of the amplitude along the propagation direction to compensate the absorption by the atomic medium, which will be large as the defect beam is set near resonance for maximal efficiency. The intensity of the beam follows a Beer law along the medium, so we must design a beam with an exponentially rising intensity inside the first maxima of the Bessel function. This is done using the SLM and an approach similar to [104]. I present in figure 5.2 the preliminary results of this technique.

In the near future, we will study the effect of scattering on this optically designed defect in an experiment similar to [103, 81]. A strong asset of our system is that the defect can be of any arbitrary shape, size and depth by simple optical control. This opens the way, for example, to the study of propagation in a disorder media in the presence of interactions, by sending a non-diffracting speckle pattern as defect.

5.1.3 Optomechanical signature of superfluidity Collaboration with P.E. Larré and I. Carusotto

Figure 5.3: Kayaking in a normal fluid. Kayaking in a superfluid would be a tricky task as the paddle will not help the boat to move as it will not feel any drag force.

An exciting prospect of the experiments described in the previous section is to replace the optically induced defect by a real object and observe the optomechanical signature of superfluidity. Let us start by the analogy with a matter fluid. Imagine a flexible tree branch touching a river as highlighted in green in figure 5.3. When flowing water hits the branch, it moves it in the flow direction by applying a drag force on it. But with a superfluid the drag force vanishes and the branch comes back to its initial position. We want to produce an analogous experiment with light.

A defect can be created by any dielectric object with a refractive index different from the medium. We propose to use a tapered optical nanofiber in glass as a defect. The setup consists in the introduction of a nanofiber inside a rubidium vapor cell, along the cell direction. Sending near resonant light in the cell with a small angle with respect to the nanofiber will slightly move it thanks

to the radiation pressure (or the drag force in the hydrodynamics language). By increasing the light intensity (while staying below superfluidity threshold) one can increase the radiation pressure and in consequence the displacement of the nanofiber should be larger. However, when the light becomes superfluid the drag force no longer exists and the nanofiber should come back to its initial position as in absence of light. This effect has been predicted in Ref. [105]. The interpretation in non-linear optics language is more convoluted as it means that radiation pressure is cancelled by non-linearities above a certain threshold. Once again the hydrodynamic language provides us with an intuitive interpretation of a novel phenomena that is virtually impossible to predict using non-linear optics intuition.

In the implementation I propose here, we have a crucial tool to achieve this challenging experiment: we know how to precisely monitor the displacement of a nanofiber with a resolution below 2 nm. To do so, we use the fact that a nanoparticle deposited on a nanofiber scatters light inside the guided mode of the fiber. By placing a nanofiber within a standing wave (in the transverse plane), and monitoring the intensity of the scattered light, we can monitor fiber displacement with a resolution of 2 nm, well below diffraction limit.

For us, the next experimental step is to combine the nanofiber and the non-linear medium into one experiment and probe the optomechanical signature of superfluidity.

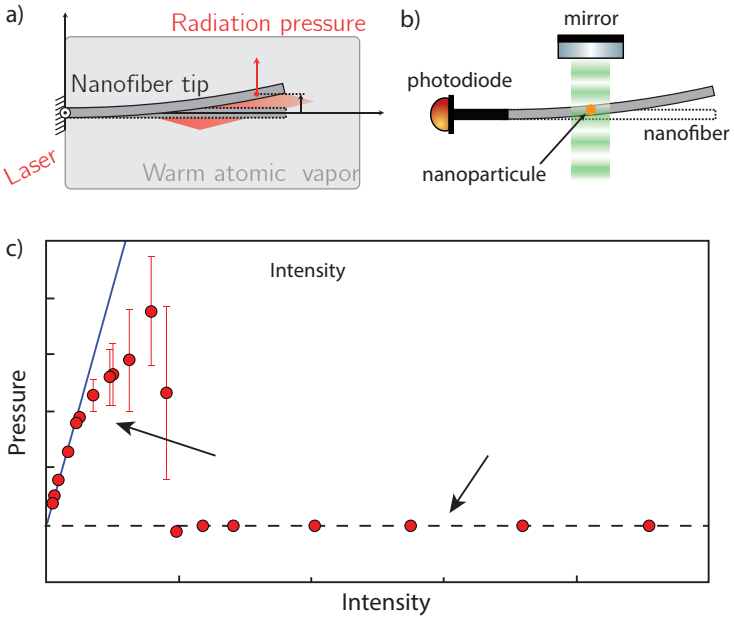

Figure 5.4: Optomechanical signature of superfluidity. a) Proposed implementation. b) Displacement measurement setup. The standing wave (green laser) is scattered inside the guided mode of the fiber by a nanoparticle. c) Pressure force as function of intensity. At the threshold of superfluidity the pressure force becomes zero and the frag force vanishes. Insets are numerical simulations of normal fluid and superfluids regimes. Adapted from [105]

5.1.4 Analogue gravity Collaboration with D. Faccio

A vast topic that fluids of light can help to investigate is analogue gravity, i.e. how to mimic gravitational effects in a non-linear optics experiment. The underlying idea behind hydrodynamical model for gravity has been introduced by Unruh. In 1981, he showed that sound waves in an accelerated flowing medium mimic the space-time geometry of a black hole [106]. As a consequence it is possible to look at quantum effects in the vicinity of the horizon and for example study the analogue of Hawking radiation, in a non-linear quantum system.

We can get an intuition about this effect using once again the analogy with water. Let us imagine a river flowing towards a few meters waterfall with a faster and faster flow speed. A fish swimming in the river (with a maximum velocity) will be irrevocably sent through the waterfall if he crosses the point where water flow speed becomes larger than its maximum velocity. This point is analogous to a black hole horizon (for fish). It is also true for (density) waves propagating on the river at the speed of sound. The black hole becomes a dumb hole (for sound waves instead of light).

Another familiar implementation is the hydraulic jump which appears in a sink. When water flows from the tap (at a given flow rate) and hits the bottom of the sink a circular region with laminar flow appears in the center and after an hydraulic jump one can observe turbulent flow. Because the flow rate is constant, water velocity is much faster in the center than at larger radius. In consequence, no waves can penetrate inside the central region because, there, the sound speed is slower than the water velocity. A region of space where no wave can enter is the time reversal opposite of a black hole also known as a white hole.

In optics, a similar idea can be implemented using the Madelung transformations. The density of the fluid is analogous to the intensity and therefore the speed of sound scales with the square root of the intensity. A sudden change in intensity in the transverse plane is then suitable to create the analogue of a black hole horizon [107]. Interesting theoretical proposals [108] investigate this configuration to observe the optical analogue of the Hawking radiation, and a potential implementation in our platform can be envisioned.

Another striking effect is known as the Zel'dovich effect i.e. the amplification of radiation scattering off rotating absorbing surfaces. The first demonstration of this effect dates back to 1971 when Zel'dovich showed that electromagnetic waves can be amplified when reflected on a rotating conducting object [109]. This effect has been extended to cosmology by Misner who showed, in 1972, that this reflection can also occur near rotating Kerr black holes [110]. Observation of this type of super-radiance in hydrodynamics has also been possible and is known as *over-reflection effect* [111]. Surprisingly, no experiment in optics have studied this effect so far. Our platform can be suitable for the observation of this effect in the optical domain. Indeed, analogue of rotating black holes can be created by injecting a fluid with an orbital angular momentum using a Laguerre-Gauss beam. The general topic of analogue gravity (and even analogue physics) is a good match with our approach which aims to find novel effects in non-linear

and quantum optics through the perspective of other physical phenomena.

5.1.5 Disorder and interactions Collaboration with N. Cherroret

Quantum fluids of light are characterized by long-range coherence. This not only favors superfluid behaviors but also localization phenomena in disordered potentials. In our platform, we can shape the spatial distribution $n_1(x, y, z)$ of the linear refractive index (i.e. the external potential) by applying a control field with the intensity profile modeled with a spatial light modulator. In particular, a disorder potential can be generated by illuminating the atomic medium with a random speckle intensity pattern. We plan to investigate the interplay between localization features, which correspond to freezing the motion in the disordered landscape, and perfect transmission, corresponding to a super-flow regime. In particular, the competition between localization and superfluid transport is envisaged as a novel route for guiding light in a disordered non-linear environment.

At zero temperature, a 1D phase diagram can be calculated in the presence of interactions as shown schematically in Figure 5.5. While the non–interacting regime can exhibit an Anderson localization, slightly repulsive interactions between the photons tend, on the contrary, to suppress this effect. A transition in favor of superfluidity should then occur, although the critical threshold for light superfluidity is expected to be substantially affected by the disorder. I propose to study the phase transitions marked with black arrows in Figure 5.5, at the quantum level in 1D and 2D. This comes along the lines of the complex but very exciting problem of many-body localization (MBL) which extends the concept of localization beyond the mean field approximation. Our system benefits of crucial assets to study this effect: a full quantum description is available [112], temperature, kinetic energy and interactions are tunable, disorder can be increased adiabatically and the dynamics of thermalization can be studied at various times and various spatial scales.

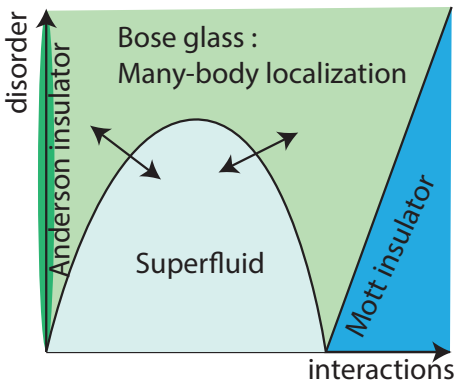

Figure 5.5: Phase diagram of a 1D system at T=0 in presence of disorder and interactions. We propose to study the phase transitions marked with the black arrows.

5.2 Quantum simulation with photons

I have tried in this manuscript to describe the tools which make the connection between quantum optics and quantum simulation with light. Before concluding, I want to explain how quantum memories or four-wave-mixing configurations can be used in the context of quantum simulation. Ultra-cold atoms in optical lattices are the current gold-standard to simulate Hamiltonian (conservative) dynamics. Let me briefly discuss why photonics quantum simulators are an exciting direction to explore !

5.2.1 From ultracold atoms to quantum fluids of light

The design of an analog quantum simulator relies on three steps [113]. First, we should prepare an input state relevant for the physical problem of interest (either a well defined quantum state or an equilibrium state at non-zero temperature). Next, we need to realize the proper mapping of the Hamiltonian to be simulated, including both the single-particle physics (external potential, effective mass) and the interaction between the constituents. Finally, measurements are performed on the output state to extract information on the simulated dynamics with the highest-possible precision. The cold-atoms community has achieved tremendous progresses in the recent years on these three tasks. We will briefly review how they are implemented on ultra-cold atoms and optical platforms.

Initial state preparation Preparing a state for quantum simulation implies to control the density distribution in the position or the momentum space, the energy or the temperature. Because ultracold atoms are prepared in a trap, it is somehow complicated to control precisely the local density for example. For light-based platforms, state preparation is more straightforward as it relies on optics. Cavity-setups are effective 2D systems in the transverse direction, and therefore, the density distribution in the position space is set by imaging a given intensity pattern onto a defined plane of the system (typically the cavity plane). Momentum distribution relies on the angular distribution of the photons and can then be tuned in the Fourier plane. Shifting away from zero, the mean of this momentum distribution injects a kinetic energy in the system and induces an effective flow in the transverse plane. On the other hand, the momentum distribution variance (the spread in momentum) defines an effective temperature of the photon fluid. For a variance of $1/l_\perp^2$, we can write the gaussian distribution of momentum $\exp[-k^2 l_\perp^2]$ and compare it to the thermodynamics expression $\exp[-\frac{\hbar^2 k^2}{2m}/\frac{k_B T}{4\pi}]$ to identify $T \propto 1/l_\perp^2$. For quantum fluids of light, thermalization occurs through the non-linear interaction mediated by the coupling with matter. An interesting feature of these setups is the possibility to isolate a subregion of the entire fluid by imaging it and therefore study the thermalization locally which is impossible with cold atoms.

Engineering the simulated Hamiltonians. An example of the Hamiltonian design with ultracold atoms is the simulation of condensed-matter systems of electrons moving on an array of atom cores. This configuration can be mapped to interacting ultra-cold atoms in an optical lattice. The interactions between atoms are tuned with the use of Feshbach resonances and the energy landscape at the single-particle level is controlled with an optical lattice,

created using the interference pattern of far-detuned overlapping laser beams, thanks to the dipole force. This precise control allows to simulate a quantum phase transition from a superfluid to a Mott insulator when the on-site interaction energy becomes much larger than the hoping energy due to tunneling between neighboring sites. For quantum fluids of light, the same level of control can be reached. The effective photon-photon interaction is mediated by the non-linearity $\chi^{(3)}$ of the medium and the potential landscape is created by auxiliary laser beams. Another example in the control of the Hamiltonian for an atomic quantum fluid is the development of artificial gauge fields, opening the way to the simulation of synthetic magnetic fields for neutral atoms, quantum Hall effect and topological phases. Similarly, fluids of light can also implement artificial gauge fields and synthetic magnetism [114, 115] by using for example photon orbital angular momentum [116].

Detection of the final state On the detection side, quantum optics techniques offer genuine advantages when working with a photonics platform compared to quantum simulations with ultra-cold gases. Typical ultra-cold atoms experiments use time-of-flight images after releasing the atoms from the trapping potential to provide insight into the momentum distribution and coherence properties [113]. Only recently, the trapped density distribution of a quantum gas has become available to experimentalists, at the cost of a complex in situ imaging setup called a quantum gas microscope [117]. With quantum fluids of light, detection turns out to be a much easier task, consisting in measuring the light exiting the system. Similar to state preparation, we can access the momentum distribution by imaging the Fourier plane and the density distribution by imaging the real plane. Moreover, coherence properties are available through interferometric techniques ($g^{(1)}$ and $g^{(2)}$ measurements) which are parts of the standard quantum optics toolbox. This ease of preparation and detection is actually one of the main benefits of quantum fluids of light and one attractive aspect of photonic quantum simulation in respect to quantum simulation with ultra-cold atoms.

5.2.2 Double-Λ configuration

The goal is to refine the EIT configuration to allow for more complex equations to be simulated. By adding a forth level and a second coupling beam it is possible to do so. I will not go into the details of the derivation, the interested reader can use [118], but I will just mention the main result that we are planning to implement in our setup.

With two coupling beams (the EIT beam is noted Ω_c and the second coupling beam Ω_s) the evolution equation for the probe Rabi frequency Ω_p is:

$$-i\frac{\partial}{\partial z}\Omega_p = \left[\frac{1}{2}\nabla_\perp^2 + V(r) - G(r)|\Omega_p|^2\right]\Omega_p, \tag{5.1}$$

with the potentiel given by

$$V(r) = -\frac{\kappa|\Omega_s|^2}{2\Delta(|\Omega_c|^2 + |\Omega_s|^2)}, \tag{5.2}$$

and the non-linear coupling term:

$$G(r) = -\frac{\kappa|\Omega_s|^2}{2\Delta(|\Omega_c|^2 + |\Omega_s|^2)^2}. \tag{5.3}$$

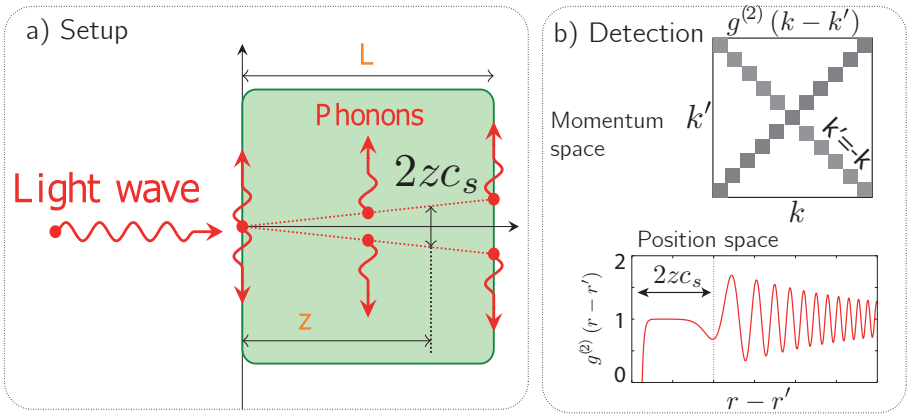

Figure 5.6: a) Schematic representation of the dynamical Casimir effect in a non-linear medium. Pairs of quantum correlated phonons (or intensity modulation) are generated at the input of the cell by the non-linearity quench. They propagate in the transverse direction at c_s the speed of sound and can be detected by homodyne detection at the output plane. b) Expected correlations in the momentum space and position space. Adapted from [112]

κ is a constant given by $\kappa = N\mu^2/(\varepsilon_0\hbar\Gamma)$. Obviously this two coefficients are coupled, but this opens the way to control of potential and non-linearity with much more degrees of liberty that what we currently achieve with two-level atoms.

5.2.3 Quantum optics

Going *quantum* is certainly a fundamental landmark in the field of photonics quantum simulators. Because light in warm atomic vapor is a well controlled system which has already proved to be an excellent source of quantum correlated beams (see chapter 3 for example) I anticipate that it could be the first system to lay the groundwork for achieving valuable results .

One step in this direction could be done by investigating the dynamical Casimir effect [112]. In the same experimental configuration as in section 4.5, but without the probe beam to seed an excited Bogoliubov mode, we have an interesting test-bed for quantum simulation. Indeed, because of the quench of the interaction at the entrance of the medium, quantum correlated pairs of Bogoliubov modes are generated even in the absence of the probe beam analogous to the dynamical Casimir effect. This is the same difference as between bright squeezing and squeeze vacuum as discussed in chapter 3. The main challenge is now to find a technique to measure the correlations presented in figure 5.6.

This experiment is basically a four-wave-mixing setup with a detection scheme in the plane of the cell output and not in the far field. Homodyne detection seems to be the suitable tool, however this means going to non-zero frequency to be realistic. The step that remains to be done is therefore to include frequency dependance inside the evolution equation and see how the analogy with the non-linear Schrödinger equation holds.

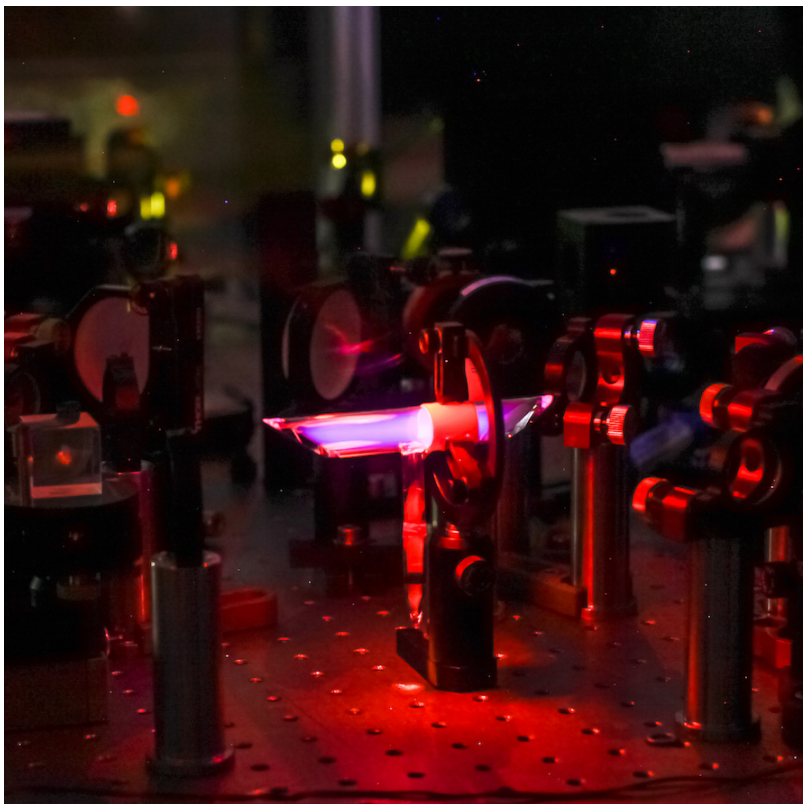

Figure 5.7: A nice picture of a rubidium cell to conclude...

5.3 Nano-optics

An important part of my work since I joined the LKB in 2013 has been dedicated to the development of a novel experimental apparatus for nano-optics. In writing this manuscript, I want to show the possible links that still remain to be tied between quantum optics and quantum memory on one hand and fluids of light and quantum simulation with light in the other. Therefore nanooptics experiments did not fit well in this effort. However, the interested reader can learn more about these works in the following references [119, 120, 121, 122, 123]:

- Polarization Control of Linear Dipole Radiation Using an Optical Nanofiber.
  M. Joos, C. Ding, V. Loo, G. Blanquer, E. Giacobino, A. Bramati, V. Krachmalnicoff, **Q Glorieux**.
  Phys. Rev. Applied, **9**, 064035 (2018).

- CdSe/CdS dot–in–rods nanocrystals fast blinking dynamics.
  M. Manceau, S. Vezzoli, **Q Glorieux**, E. Giacobino L. Carbone, M. De Vittorio J-P. Hermier, A. Bramati.
  ChemPhysChem, Accepted. (2018).

- Localised excitation of a single photon source by a nanowaveguide.
  W. Geng, M. Manceau, N, Rahbany, V. Sallet, M. De Vittorio, L. Carbone, **Q. Glorieux**, A. Bramati, C. Couteau.
  Scientific Reports **6**, 19721 (2016).

- Exciton Fine Structure of CdSe/CdS Nanocrystals Determined by Polarization Microscopy at Room Temperature.
  S. Vezzoli, M. Manceau, G. Leménager, **Q. Glorieux**, E. Giacobino, L. Carbone, M. De Vittorio, A. Bramati.
  ACS Nano **9**, 7992 (2015).

- Effect of charging on CdSe/CdS dot-in-rods single-photon emission.
  M. Manceau, S. Vezzoli, **Q. Glorieux**, F. Pisanello, E. Giacobino, L. Carbone, M. De Vittorio, A. Bramati.
  Phys. Rev. B **90**, 035311 (2014).

Bibliography

[1] Q. Fontaine, T. Bienaimé, S. Pigeon, E. Giacobino, A. Bramati, and Q. Glorieux, "Observation of the bogoliubov dispersion in a fluid of light," *Phys. Rev. Lett.*, vol. 121, p. 183604, Oct 2018. [Online]. Available: https://link.aps.org/doi/10.1103/PhysRevLett.121.183604

[2] R. H. Dicke, "Coherence in spontaneous radiation processes," *Physical Review*, vol. 93, no. 1, p. 99, 1954.

[3] D. A. Steck, "Rubidium 85 d line data," 2001. [Online]. Available: https://steck.us/alkalidata/rubidium85numbers.pdf

[4] M. Gross and S. Haroche, "Superradiance: An essay on the theory of collective spontaneous emission," *Physics reports*, vol. 93, no. 5, pp. 301–396, 1982.

[5] M. O. Scully and A. A. Svidzinsky, "The super of superradiance," *Science*, vol. 325, no. 5947, pp. 1510–1511, 2009.

[6] M. Fleischhauer and M. D. Lukin, "Quantum memory for photons: Dark-state polaritons," *Physical Review A*, vol. 65, no. 2, p. 022314, 2002.

[7] C. Alcock, V. Itkin, and M. Horrigan, "Vapour pressure equations for the metallic elements: 298–2500k," *Canadian Metallurgical Quarterly*, vol. 23, no. 3, pp. 309–313, 1984.

[8] P. Van der Straten and H. Metcalf, *Atoms and molecules interacting with light: Atomic physics for the laser era*. Cambridge University Press, 2016.

[9] Q. Glorieux, "Etude theorique et experimentale des correlations quantiques obtenues par melange a quatre ondes dans une vapeur atomique," Ph.D. dissertation, Université Paris-Diderot-Paris VII, 2010.

[10] O. Mishina, M. Scherman, P. Lombardi, J. Ortalo, D. Felinto, A. Sheremet, A. Bramati, D. Kupriyanov, J. Laurat, and E. Giacobino, "Electromagnetically induced transparency in an inhomogeneously broadened λ transition with multiple excited levels," *Physical Review A*, vol. 83, no. 5, p. 053809, 2011.

[11] A. S. Sheremet, L. V. Gerasimov, I. M. Sokolov, D. V. Kupriyanov, O. S. Mishina, E. Giacobino, and J. Laurat, "Quantum memory for light via a stimulated off-resonant raman process: Beyond the three-level λ-scheme approximation," *Physical Review A*, vol. 82, no. 3, p. 033838, 2010.

[12] R. W. Boyd, *Nonlinear optics*. Elsevier, 2003.

[13] W. Zhao and P. Palffy-Muhoray, "Z-scan technique using top-hat beams," *Applied physics letters*, vol. 63, no. 12, pp. 1613–1615, 1993.

[14] C. M. Nascimento, M. A. R. C. Alencar, S. Chavez-Cerda, M. G. A. da Silva, M. R. Meneghetti, and J. M. Hickmann, "Experimental demonstration of novel effects on the far-field diffraction patterns of a gaussian beam in a kerr medium," *Journal of Optics A: Pure and Applied Optics*, vol. 8, no. 11, p. 947, 2006. [Online]. Available: http://stacks.iop.org/1464-4258/8/i=11/a=003

[15] Y. Zhang, X. Cheng, X. Yin, J. Bai, P. Zhao, and Z. Ren, "Research of far-field diffraction intensity pattern in hot atomic rb sample," *Opt. Express*, vol. 23, no. 5, pp. 5468–5476, Mar 2015. [Online]. Available: http://www.opticsexpress.org/abstract.cfm?URI=oe-23-5-5468

[16] K.-J. Boller, A. Imamoğlu, and S. E. Harris, "Observation of electromagnetically induced transparency," *Physical Review Letters*, vol. 66, no. 20, p. 2593, 1991.

[17] M. Fleischhauer and M. Lukin, "Dark-state polaritons in electromagnetically induced transparency," *Physical Review Letters*, vol. 84, no. 22, p. 5094, 2000.

[18] Q. Glorieux, R. Dubessy, S. Guibal, L. Guidoni, J.-P. Likforman, T. Coudreau, and E. Arimondo, "Double-λ microscopic model for entangled light generation by four-wave mixing," *Physical Review A*, vol. 82, no. 3, p. 033819, 2010.

[19] Q. Glorieux, L. Guidoni, S. Guibal, J.-P. Likforman, and T. Coudreau, "Quantum correlations by four-wave mixing in an atomic vapor in a nonamplifying regime: Quantum beam splitter for photons," *Physical Review A*, vol. 84, no. 5, p. 053826, 2011.

[20] I. H. Agha, C. Giarmatzi, Q. Glorieux, T. Coudreau, P. Grangier, and G. Messin, "Time-resolved detection of relative-intensity squeezed nanosecond pulses in an 87rb vapor," *New Journal of Physics*, vol. 13, no. 4, p. 043030, 2011.

[21] Q. Glorieux, J. B. Clark, N. V. Corzo, and P. D. Lett, "Generation of pulsed bipartite entanglement using four-wave mixing," *New Journal of Physics*, vol. 14, no. 12, p. 123024, 2012.

[22] N. V. Corzo, Q. Glorieux, A. M. Marino, J. B. Clark, R. T. Glasser, and P. D. Lett, "Rotation of the noise ellipse for squeezed vacuum light generated via four-wave mixing," *Physical Review A*, vol. 88, no. 4, p. 043836, 2013.

[23] U. Vogl, R. T. Glasser, Q. Glorieux, J. B. Clark, N. V. Corzo, and P. D. Lett, "Experimental characterization of gaussian quantum discord generated by four-wave mixing," *Phys. Rev. A*, vol. 87, p. 010101, Jan 2013. [Online]. Available: https://link.aps.org/doi/10.1103/PhysRevA.87.010101

[24] U. Vogl, R. T. Glasser, J. B. Clark, Q. Glorieux, T. Li, N. V. Corzo, and P. D. Lett, "Advanced quantum noise correlations," *New Journal of Physics*, vol. 16, no. 1, p. 013011, 2014. [Online]. Available: http://stacks.iop.org/1367-2630/16/i=1/a=013011

[25] L.-M. Duan, M. Lukin, J. I. Cirac, and P. Zoller, "Long-distance quantum communication with atomic ensembles and linear optics," *Nature*, vol. 414, no. 6862, p. 413, 2001.

[26] J. B. Clark, R. T. Glasser, Q. Glorieux, U. Vogl, T. Li, K. M. Jones, and P. D. Lett, "Quantum mutual information of an entangled state propagating through a fast-light medium," *Nature Photonics*, vol. 8, no. 7, p. 515, 2014.

[27] M. S. Bigelow, N. N. Lepeshkin, and R. W. Boyd, "Superluminal and slow light propagation in a room-temperature solid," *Science*, vol. 301, no. 5630, pp. 200–202, 2003.

[28] P. W. Milonni, *Fast light, slow light and left-handed light*. CRC Press, 2004.

[29] R. W. Boyd and D. J. Gauthier, "Slow and fast light," ROCHESTER UNIV NY INST OF OPTICS, Tech. Rep., 2001.

[30] L. V. Hau, S. E. Harris, Z. Dutton, and C. H. Behroozi, "Light speed reduction to 17 metres per second in an ultracold atomic gas," *Nature*, vol. 397, no. 6720, p. 594, 1999.

[31] A. Kozhekin, K. Mølmer, and E. Polzik, "Quantum memory for light," *Physical Review A*, vol. 62, no. 3, p. 033809, 2000.

[32] R. W. Boyd and D. J. Gauthier, "Controlling the velocity of light pulses," *Science*, vol. 326, no. 5956, pp. 1074–1077, 2009.

[33] J. B. Khurgin and R. S. Tucker, *Slow light: Science and applications*. CRC press, 2008.

[34] H. J. Kimble, "The quantum internet," *Nature*, vol. 453, no. 7198, p. 1023, 2008.

[35] A. I. Lvovsky, B. C. Sanders, and W. Tittel, "Optical quantum memory," *Nature photonics*, vol. 3, no. 12, p. 706, 2009.

[36] Q. Glorieux, J. B. Clark, A. M. Marino, Z. Zhou, and P. D. Lett, "Temporally multiplexed storage of images in a gradient echo memory," *Optics express*, vol. 20, no. 11, pp. 12 350–12 358, 2012.

[37] B. Sparkes, J. Bernu, M. Hosseini, J. Geng, Q. Glorieux, P. A. Altin, P. K. Lam, N. Robins, and B. Buchler, "Gradient echo memory in an ultra-high optical depth cold atomic ensemble," *New Journal of Physics*, vol. 15, no. 8, p. 085027, 2013.

[38] G. Hetet, J. Longdell, A. Alexander, P. K. Lam, and M. Sellars, "Electro-optic quantum memory for light using two-level atoms," *Physical review letters*, vol. 100, no. 2, p. 023601, 2008.

[39] G. Hétet, M. Hosseini, B. M. Sparkes, D. Oblak, P. K. Lam, and B. C. Buchler, "Photon echoes generated by reversing magnetic field gradients in a rubidium vapor," *Optics letters*, vol. 33, no. 20, pp. 2323–2325, 2008.

[40] M. Hosseini, B. M. Sparkes, G. Campbell, P. K. Lam, and B. C. Buchler, "High efficiency coherent optical memory with warm rubidium vapour," *Nature communications*, vol. 2, p. 174, 2011.

[41] J. B. Clark, "Timing the state of light with anomalous dispersion and a gradient echo memory," Ph.D. dissertation, University of Maryland, College Park, 2014.

[42] M. Steger, K. Saeedi, M. Thewalt, J. Morton, H. Riemann, N. Abrosimov, P. Becker, and H.-J. Pohl, "Quantum information storage for over 180 s using donor spins in a 28si semiconductor vacuum," *Science*, vol. 336, no. 6086, pp. 1280–1283, 2012.

[43] M. Hosseini, "Quantum optical storage and processing using raman gradient echo memory," Ph.D. dissertation, Australian National University, 2012.

[44] G. Hétet, J. Longdell, M. Sellars, P. K. Lam, and B. Buchler, "Multimodal properties and dynamics of gradient echo quantum memory," *Physical review letters*, vol. 101, no. 20, p. 203601, 2008.

[45] J. B. Clark, Q. Glorieux, and P. D. Lett, "Spatially addressable readout and erasure of an image in a gradient echo memory," *New Journal of Physics*, vol. 15, no. 3, p. 035005, 2013.

[46] W. Ketterle, K. B. Davis, M. A. Joffe, A. Martin, and D. E. Pritchard, "High densities of cold atoms in a dark spontaneous-force optical trap," *Physical review letters*, vol. 70, no. 15, p. 2253, 1993.

[47] M. T. DePue, S. L. Winoto, D. Han, and D. S. Weiss, "Transient compression of a mot and high intensity fluorescent imaging of optically thick clouds of atoms," *Optics communications*, vol. 180, no. 1-3, pp. 73–79, 2000.

[48] A. M. Marino, J. B. Clark, Q. Glorieux, and P. D. Lett, "Extracting spatial information from noise measurements of multi-spatial-mode quantum states," *The European Physical Journal D*, vol. 66, no. 11, p. 288, Nov 2012. [Online]. Available: https://doi.org/10.1140/epjd/e2012-30037-1

[49] B. Schutz, *A first course in general relativity*. Cambridge university press, 2009.

[50] A. Peres and D. R. Terno, "Quantum information and relativity theory," *Reviews of Modern Physics*, vol. 76, no. 1, p. 93, 2004.

[51] S. L. Braunstein and P. Van Loock, "Quantum information with continuous variables," *Reviews of Modern Physics*, vol. 77, no. 2, p. 513, 2005.

[52] C. Weedbrook, S. Pirandola, R. García-Patrón, N. J. Cerf, T. C. Ralph, J. H. Shapiro, and S. Lloyd, "Gaussian quantum information," *Reviews of Modern Physics*, vol. 84, no. 2, p. 621, 2012.

[53] R. W. Boyd, "Slow and fast light: fundamentals and applications," *Journal of Modern Optics*, vol. 56, no. 18-19, pp. 1908–1915, 2009.

[54] L. Brillouin, "Über die fortpflanzung des lichtes in dispergierenden medien," *Annalen der Physik*, vol. 349, no. 10, pp. 203–240, 1914.

[55] M. D. Stenner, D. J. Gauthier, and M. A. Neifeld, "The speed of information in a fast-light optical medium," *Nature*, vol. 425, no. 6959, p. 695, 2003.

[56] A. Kuzmich, A. Dogariu, L. Wang, P. Milonni, and R. Chiao, "Signal velocity, causality, and quantum noise in superluminal light pulse propagation," *Physical review letters*, vol. 86, no. 18, p. 3925, 2001.

[57] M. D. Stenner, D. J. Gauthier, and M. A. Neifeld, "Fast causal information transmission in a medium with a slow group velocity," *Physical review letters*, vol. 94, no. 5, p. 053902, 2005.

[58] H. Wilhelm, "Hydrodynamic model of quantum mechanics," *Physical Review D*, vol. 1, no. 8, p. 2278, 1970.

[59] C. Sulem and P.-L. Sulem, *The nonlinear Schrödinger equation: self-focusing and wave collapse*. Springer Publishing, 2007, vol. 139.

[60] C. Coste, "Nonlinear schrödinger equation and superfluid hydrodynamics," *The European Physical Journal B-Condensed Matter and Complex Systems*, vol. 1, no. 2, pp. 245–253, 1998.

[61] F. Dalfovo, S. Giorgini, L. P. Pitaevskii, and S. Stringari, "Theory of bose-einstein condensation in trapped gases," *Reviews of Modern Physics*, vol. 71, no. 3, p. 463, 1999.

[62] R. Fedele and H. Schamel, "Solitary waves in the madelung's fluid: Connection between the nonlinear schrödinger equation and the korteweg-de vries equation," *The European Physical Journal B-Condensed Matter and Complex Systems*, vol. 27, no. 3, pp. 313–320, 2002.

[63] E. Madelung, "Quantentheorie in hydrodynamischer form," *Zeitschrift für Physik A Hadrons and Nuclei*, vol. 40, no. 3, pp. 322–326, 1927.

[64] L. Lugiato, "Transverse nonlinear optics: Introduction and review," *Chaos, Solitons & Fractals*, vol. 4, no. 8-9, pp. 1251–1258, 1994.

[65] L. Lugiato, M. Brambilla, and A. Gatti, "Optical pattern formation," in *Advances in Atomic, Molecular, and Optical Physics*. Elsevier, 1999, vol. 40, pp. 229–306.

[66] M. Brambilla, F. Battipede, L. Lugiato, V. Penna, F. Prati, C. Tamm, and C. Weiss, "Transverse laser patterns. i. phase singularity crystals," *Physical Review A*, vol. 43, no. 9, p. 5090, 1991.

[67] K. Staliunas, "Laser ginzburg-landau equation and laser hydrodynamics," *Physical Review A*, vol. 48, no. 2, p. 1573, 1993.

[68] Y. Pomeau and S. Rica, "Nonlinear diffraction," *Comptes rendus de l'Académie des Sciences. Série II*, vol. 317, no. 10, pp. 1287–1292, 1993.

[69] P. Coullet, L. Gil, and F. Rocca, "Optical vortices," *Optics Communications*, vol. 73, no. 5, pp. 403–408, 1989.

[70] M. Vaupel, K. Staliunas, and C. Weiss, "Hydrodynamic phenomena in laser physics: Modes with flow and vortices behind an obstacle in an optical channel," *Physical Review A*, vol. 54, no. 1, p. 880, 1996.

[71] R. Y. Chiao and J. Boyce, "Bogoliubov dispersion relation and the possibility of superfluidity for weakly interacting photons in a two-dimensional photon fluid," *Physical Review A*, vol. 60, no. 5, p. 4114, 1999.

[72] J. Klaers, J. Schmitt, F. Vewinger, and M. Weitz, "Bose–einstein condensation of photons in an optical microcavity," *Nature*, vol. 468, pp. 545 EP –, 11 2010. [Online]. Available: https://doi.org/10.1038/nature09567

[73] C. Ciuti, V. Savona, C. Piermarocchi, A. Quattropani, and P. Schwendimann, "Role of the exchange of carriers in elastic exciton-exciton scattering in quantum wells," *Physical Review B*, vol. 58, no. 12, p. 7926, 1998.

[74] Y. Yamamoto, F. Tassone, and H. Cao, *Semiconductor cavity quantum electrodynamics*. Springer, 2003, vol. 169.

[75] J. Hopfield, "Theory of the contribution of excitons to the complex dielectric constant of crystals," *Physical Review*, vol. 112, no. 5, p. 1555, 1958.

[76] T. Boulier, E. Cancellieri, N. D. Sangouard, Q. Glorieux, A. Kavokin, D. M. Whittaker, E. Giacobino, and A. Bramati, "Injection of orbital angular momentum and storage of quantized vortices in polariton superfluids," *Physical review letters*, vol. 116, no. 11, p. 116402, 2016.

[77] S. Pigeon, "Fluides quantiques et dispositifs à polaritons," Ph.D. dissertation, Université Paris-Diderot-Paris VII, 2011.

[78] H. Deng, G. Weihs, C. Santori, J. Bloch, and Y. Yamamoto, "Condensation of semiconductor microcavity exciton polaritons," *Science*, vol. 298, no. 5591, pp. 199–202, 2002.

[79] J. Kasprzak, M. Richard, S. Kundermann, A. Baas, P. Jeambrun, J. Keeling, F. Marchetti, M. Szymańska, R. Andre, J. Staehli *et al.*, "Bose–einstein condensation of exciton polaritons," *Nature*, vol. 443, no. 7110, p. 409, 2006.

[80] I. Carusotto and C. Ciuti, "Probing microcavity polariton superfluidity through resonant rayleigh scattering," *Physical review letters*, vol. 93, no. 16, p. 166401, 2004.

[81] A. Amo, J. Lefrère, S. Pigeon, C. Adrados, C. Ciuti, I. Carusotto, R. Houdré, E. Giacobino, and A. Bramati, "Superfluidity of polaritons in semiconductor microcavities," *Nature Physics*, vol. 5, no. 11, p. 805, 2009.

[82] P. Kapitza, "Viscosity of liquid helium below the λ-point," *Nature*, vol. 141, no. 3558, p. 74, 1938.

[83] J. F. Allen and A. Misener, "Flow of liquid helium ii," *Nature*, vol. 141, no. 3558, p. 75, 1938.

[84] K. B. Davis, M.-O. Mewes, M. R. Andrews, N. Van Druten, D. Durfee, D. Kurn, and W. Ketterle, "Bose-einstein condensation in a gas of sodium atoms," *Physical review letters*, vol. 75, no. 22, p. 3969, 1995.

[85] P. Nozieres, *Theory of quantum liquids: Superfluid bose liquids*. CRC Press, 2018.

[86] R. P. Feynman, "Atomic theory of the two-fluid model of liquid helium," *Physical Review*, vol. 94, no. 2, p. 262, 1954.

[87] L. Landau, "Theory of the superfluidity of helium ii," *Physical Review*, vol. 60, no. 4, p. 356, 1941.

[88] G. B. Hess and W. Fairbank, "Measurements of angular momentum in superfluid helium," *Physical Review Letters*, vol. 19, no. 5, p. 216, 1967.

[89] J. D. Reppy and D. Depatie, "Persistent currents in superfluid helium," *Physical Review Letters*, vol. 12, no. 8, p. 187, 1964.

[90] C. Ryu, M. Andersen, P. Clade, V. Natarajan, K. Helmerson, and W. D. Phillips, "Observation of persistent flow of a bose-einstein condensate in a toroidal trap," *Physical Review Letters*, vol. 99, no. 26, p. 260401, 2007.

[91] N. A. Silva, J. Mendonça, and A. Guerreiro, "Persistent currents of superfluidic light in a four-level coherent atomic medium," *JOSA B*, vol. 34, no. 10, pp. 2220–2226, 2017.

[92] A. Amo, S. Pigeon, D. Sanvitto, V. Sala, R. Hivet, I. Carusotto, F. Pisanello, G. Leménager, R. Houdré, E. Giacobino *et al.*, "Polariton superfluids reveal quantum hydrodynamic solitons," *Science*, vol. 332, no. 6034, pp. 1167–1170, 2011.

[93] T. Boulier, H. Terças, D. Solnyshkov, Q. Glorieux, E. Giacobino, G. Malpuech, and A. Bramati, "Vortex chain in a resonantly pumped polariton superfluid," *Scientific reports*, vol. 5, p. 9230, 2015.

[94] P. Larré and I. Carusotto, "Propagation of a quantum fluid of light in a cavityless nonlinear optical medium: General theory and response to quantum quenches," *Physical Review A*, vol. 92, no. 4, p. 043802, 2015.

[95] W. Wan, S. Jia, and J. W. Fleischer, "Dispersive superfluid-like shock waves in nonlinear optics," *Nature Physics*, vol. 3, no. 1, pp. 46–51, 2007.

[96] W. Wan, D. V. Dylov, C. Barsi, and J. W. Fleischer, "Diffraction from an edge in a self-focusing medium," *Optics letters*, vol. 35, no. 16, pp. 2819–2821, 2010.

[97] E. Khamis, A. Gammal, G. El, Y. G. Gladush, and A. Kamchatnov, "Nonlinear diffraction of light beams propagating in photorefractive media with embedded reflecting wire," *Physical Review A*, vol. 78, no. 1, p. 013829, 2008.

[98] D. Vocke, T. Roger, F. Marino, E. M. Wright, I. Carusotto, M. Clerici, and D. Faccio, "Experimental characterization of nonlocal photon fluids," *Optica*, vol. 2, no. 5, pp. 484–490, 2015.

[99] D. Vocke, K. Wilson, F. Marino, I. Carusotto, E. M. Wright, T. Roger, B. P. Anderson, P. Öhberg, and D. Faccio, "Role of geometry in the superfluid flow of nonlocal photon fluids," *Physical Review A*, vol. 94, no. 1, p. 013849, 2016.

[100] M. Elazar, V. Fleurov, and S. Bar-Ad, "All-optical event horizon in an optical analog of a laval nozzle," *Physical Review A*, vol. 86, no. 6, p. 063821, 2012.

[101] O. Firstenberg, P. London, M. Shuker, A. Ron, and N. Davidson, "Elimination, reversal and directional bias of optical diffraction," *Nature Physics*, vol. 5, no. 9, pp. 665–668, 2009.

[102] O. Firstenberg, M. Shuker, N. Davidson, and A. Ron, "Elimination of the diffraction of arbitrary images imprinted on slow light," *Physical review letters*, vol. 102, no. 4, p. 043601, 2009.

[103] C. Michel, O. Boughdad, M. Albert, P.-É. Larré, and M. Bellec, "Superfluid motion and drag-force cancellation in a fluid of light," *Nature Communications*, vol. 9, no. 1, p. 2108, 2018. [Online]. Available: https://doi.org/10.1038/s41467-018-04534-9

[104] T. Čižmár, V. Kollárová, X. Tsampoula, F. Gunn-Moore, W. Sibbett, Z. Bouchal, and K. Dholakia, "Generation of multiple bessel beams for a biophotonics workstation," *Optics Express*, vol. 16, no. 18, pp. 14 024–14 035, 2008.

[105] P. Larré and I. Carusotto, "Optomechanical signature of a frictionless flow of superfluid light," *Physical Review A*, vol. 91, no. 5, p. 053809, 2015.

[106] W. G. Unruh, "Experimental black-hole evaporation?" *Physical Review Letters*, vol. 46, no. 21, p. 1351, 1981.

[107] H. S. Nguyen, D. Gerace, I. Carusotto, D. Sanvitto, E. Galopin, A. Lemaître, I. Sagnes, J. Bloch, and A. Amo, "Acoustic black hole in a stationary hydrodynamic flow of microcavity polaritons," *Physical review letters*, vol. 114, no. 3, p. 036402, 2015.

[108] P.-É. Larré, A. Recati, I. Carusotto, and N. Pavloff, "Quantum fluctuations around black hole horizons in bose-einstein condensates," *Physical Review A*, vol. 85, no. 1, p. 013621, 2012.

[109] Y. B. Zel'Dovich, "Generation of waves by a rotating body," *ZhETF Pisma Redaktsiiu*, vol. 14, p. 270, 1971.

[110] E. D. Fackerell and J. R. Ipser, "Weak electromagnetic fields around a rotating black hole," *Physical Review D*, vol. 5, no. 10, p. 2455, 1972.

[111] M. Richartz, A. Prain, S. Liberati, and S. Weinfurtner, "Rotating black holes in a draining bathtub: superradiant scattering of gravity waves," *Physical Review D*, vol. 91, no. 12, p. 124018, 2015.

[112] P.-E. Larré and I. Carusotto, "Propagation of a quantum fluid of light in a cavityless nonlinear optical medium: General theory and response to quantum quenches," *Phys. Rev. A*, vol. 92, p. 043802, Oct 2015. [Online]. Available: https://link.aps.org/doi/10.1103/PhysRevA.92.043802

[113] I. Bloch, J. Dalibard, and S. Nascimbene, "Quantum simulations with ultracold quantum gases," *Nature Physics*, vol. 8, no. 4, pp. 267–276, 2012.

[114] J. Otterbach, J. Ruseckas, R. Unanyan, G. Juzeliūnas, and M. Fleischhauer, "Effective magnetic fields for stationary light," *Physical review letters*, vol. 104, no. 3, p. 033903, 2010.

[115] N. Schine, A. Ryou, A. Gromov, A. Sommer, and J. Simon, "Synthetic landau levels for photons," *Nature*, 2016.

[116] N. Westerberg, C. Maitland, D. Faccio, K. Wilson, P. Öhberg, and E. M. Wright, "Synthetic magnetism for photon fluids," *Phys. Rev. A*, vol. 94, p. 023805, Aug 2016. [Online]. Available: http://link.aps.org/doi/10.1103/PhysRevA.94.023805

[117] W. S. Bakr, J. I. Gillen, A. Peng, S. Fölling, and M. Greiner, "A quantum gas microscope for detecting single atoms in a hubbard-regime optical lattice," *Nature*, vol. 462, p. 74, 2009.

[118] D. G. Angelakis, M. Huo, and L. C. Kwek, "Luttinger liquid of photons and spin-charge separation in hollow-core fibers," *Physical review letters*, vol. 106, no. 15, p. 153601, 2011.

[119] M. Joos, C. Ding, V. Loo, G. Blanquer, E. Giacobino, A. Bramati, V. Krachmalnicoff, and Q. Glorieux, "Polarization control of linear dipole radiation using an optical nanofiber," *Phys. Rev. Applied*, vol. 9, p. 064035, Jun 2018. [Online]. Available: https://link.aps.org/doi/10.1103/PhysRevApplied.9.064035

[120] M. Manceau, S. Vezzoli, Q. Glorieux, E. Giacobino, L. Carbone, M. De Vittorio, J.-P. Hermier, and A. Bramati, "Cdse/cds dot-in-rods nanocrystals fast blinking dynamics." *ChemPhysChem*, vol. 19, no. 23, pp. 3288–3295. [Online]. Available: https://onlinelibrary.wiley.com/doi/abs/10.1002/cphc.201800694

[121] W. Geng, M. Manceau, N. Rahbany, V. Sallet, M. De Vittorio, L. Carbone, Q. Glorieux, A. Bramati, and C. Couteau, "Localised excitation of a single photon source by a nanowaveguide," *Scientific Reports*, vol. 6, pp. 19 721 EP –, 01 2016.

[122] S. Vezzoli, M. Manceau, G. Lemenager, Q. Glorieux, E. Giacobino, L. Carbone, M. De Vittorio, and A. Bramati, "Exciton fine structure of cdse/cds nanocrystals determined by polarization microscopy at room temperature," *ACS Nano*, vol. 9, no. 8, pp. 7992–8003, 2015, pMID: 26212764. [Online]. Available: https://doi.org/10.1021/acsnano.5b01354

[123] M. Manceau, S. Vezzoli, Q. Glorieux, F. Pisanello, E. Giacobino, L. Carbone, M. De Vittorio, and A. Bramati, "Effect of charging on cdse/cds dot-in-rods single-photon emission," *Phys. Rev. B*, vol. 90, p. 035311, Jul 2014. [Online]. Available: https://link.aps.org/doi/10.1103/PhysRevB.90.035311